

Surface analytical studies of interfaces in organic semiconductor devices

Yongli Gao *

Department of Physics and Astronomy, University of Rochester, Rochester, NY 14627, United States

ARTICLE INFO

Article history:

Available online 19 March 2010

Keywords:

Organic semiconductor interfaces
Organic–metal interface
Organic–organic interface
Organic–inorganic interface
Doping in organics
Organic light emitting diodes
Organic photovoltaic devices
Organic thin film transistors
Surface analytical studies

ABSTRACT

Surface and interface analytical studies have generated critical insight of the fundamental processes at interfaces involving organic semiconductors. I will review surface analytical studies of interface formation of organic semiconductors with different materials. Metal/organic interface is a focus of both device engineering and basic science, since it is a key factor in nearly all important aspects of device performances, including operation voltages, degradation, and efficiency. I will discuss metal–organic interface dipole formation, charge transfer, chemical reaction, energy level alignment, in-diffusion, quenching of luminescence and possible recovery of it. The effect of the insertion of ultra-thin interlayers such as LiF and doping by alkali metals will also be discussed. In organic/organic interface, the energy offset between the two dissimilar organic materials is vitally important to efficient device operation of organic light emitting diodes (OLED), as well as charge separation at donor–acceptor interface in organic photovoltaic devices (OPV). I will discuss the interface energy level alignment, band bending, Debye screening, and charge separation dynamics as observed in surface analytical studies, and the implications to OLED and OPV. The interfaces of OSCs with other inorganic materials are also important. For organic thin film transistors (OTFT), the electronic properties of the interface formed between the organic and the dielectric strongly influences the current–voltage characteristics, as the electronic activity has been shown to occur primarily at the interface between the dielectric and the organic materials. I will review the interface formation of OSCs with dielectric materials and with indium-tin-oxide (ITO), a material whose transparency and conductivity make it indispensable for a number of opto-electronic applications and whose electronic properties and energy level alignment with organics have proven dramatically altered by surface treatments.

© 2010 Elsevier B.V. All rights reserved.

Contents

1. Introduction	40
1.1. Electronic structure of organic semiconductors	40
1.2. Characteristics of interfaces in organic semiconductors	41
1.3. Interface growth mode and modeling	43
2. Experimental techniques	43
2.1. Conditions for surface analysis	44
2.2. Photoemission spectroscopy	44
2.3. Inverse photoemission spectroscopy	46
2.4. Scanning probe microscopy	47
2.5. NEXAFS, PYS, IPE, and SIMS	48
3. Metal/organic interface	48
3.1. Metal/organic interface dipole	49
3.2. Charge transfer and chemical reaction	52
3.3. Diffusion and cluster formation	54
3.4. Band bending in metal/organic semiconductor interface	56
3.5. Quenching of excitons	56
3.6. Contaminated surface	57

* Tel.: +1 585 2758574; fax: +1 585 2758527.

E-mail address: ygao@pas.rochester.edu.

4.	Organic/organic interface	58
4.1.	Organic/organic interface energy level alignment	58
4.2.	Band bending and carrier accumulation at organic/organic interface	60
4.3.	Interface charge separation and transfer	63
5.	Organic/inorganic interface	65
5.1.	Organic/insulator interface	65
5.2.	ITO surface treatment and its interface with organics	68
6.	Interface engineering	69
6.1.	Doping	70
6.2.	Reversal of doping induced energy level shift	73
6.3.	Insertion of ultra-thin interlayers	74
7.	Structural, electronic, and electrical studies on ordered systems	76
8.	Possible damage by surface analytical probes	80
9.	Final remarks	81
	Acknowledgements	81
	References	81

1. Introduction

Organic semiconductor materials have demonstrated their potential as a new class of electronic materials for applications including, but not limited to, organic light emitting diodes (OLED) [1], organic thin film transistors (OTFT) [2], and organic photovoltaic devices (OPV) [3]. In all organic semiconductor devices, the charge transport process across interfaces of dissimilar materials is important for optimum device operation. As proven in over five decades of research, the understanding of interfaces of inorganic semiconductors (ISC) with metals, semiconductors, and insulators, has had a tremendous impact on semiconductor device technology. Similar situation is found also in organic semiconductor (OSC) devices. Furthermore, the thickness of the active organic layer is typically only a few hundred angstroms in OSC devices, which further blurs the distinction between bulk and interface.

Understanding the interface processes in organic devices is critical for their further advance in performance. Surface and interface analytical studies have generated critical insight of the fundamental processes at interfaces involving organic semiconductors, as summarized in books and review articles [4–10]. For example, it is established now from surface analytical studies that the interface energy level alignment is not from a common vacuum level as previously believed. Instead, it depends on the detailed interface interactions including wavefunction hybridization, charge transfer, chemical reaction, and intermixing, etc. Understanding issues regarding metal/organic interfaces, such as the formation of the interface dipole, the injection barrier, the diffusiveness of the interface and origin of ionized species, is beginning to take shape.

In this review, I intend to introduce the readers to the field of organic semiconductor interface formation by summarizing information on the interfaces obtained by using popular interface analytical techniques. In writing this article, I have naturally chosen to draw on my expertise of investigating interface electronic structures with photoemission spectroscopy, such as ultraviolet photoemission spectroscopy and related techniques. This is by no means implying that these tools are the only ones used, or are better than others in the study of organic semiconductor devices. The hope is that some insights for the fundamental aspects of metal/organic, organic/organic, and organic/inorganic interface formation can be appreciated by learning examples and studies through surface/interface analysis. In the reminder of this section, I will introduce the background knowledge of the electronic structure, molecular properties, and interface characteristics. In Section 2, surface and interface analytical techniques popularly applied to OSC studies will be described. Metal/organic, organic/organic, and organic/inorganic interfaces will be discussed in Sections 3–5, respectively. Investigations on interface engineering and doping are presented

in Section 6. Studies of ordered systems are described in Section 7. In Section 8, possible damages of OSC by surface analytical tools are discussed. A brief summary and future prospects are provided in Section 9.

1.1. Electronic structure of organic semiconductors

Physical models of solids are built upon the realization that the interactions between neighboring atoms or molecules in a lattice give rise to allowed energy levels that electrons occupy. The variation in the orientation and distance between neighboring atoms or molecules in solid creates a rich band structure, which in turn determines the properties of the material. Shown in Fig. 1.1 are the schematics of the energy levels of hydrogen molecule and the energy band formation of a 1D crystal. As two hydrogen atoms form a hydrogen molecule, the electron wavefunctions of the 1s orbital of the two atoms overlap, resulting in molecular bonding (σ) and antibonding (σ^*) bonds with corresponding energy levels split from that of the initial H 1s orbital. When a large number of N H atoms form a 1D crystal, the overlap of the wavefunctions leads to the formation of N energy levels closely packed that can usually be considered as a continuum of an energy band. The width of the energy band depends on the degree of the wavefunction overlap, or the spacing between the atoms, as shown beautifully by Shockley in 1939 [11]. In a lattice with a periodic potential, the electronic wavefunction is described by Bloch's theorem, which states that $\psi_k(\mathbf{r})$, the solutions of the Schrodinger equation must be of the form [12]

$$\psi_k(\vec{r}) = u_k(\vec{r}) \exp(i\vec{k} \cdot \vec{r}) \quad (1.1)$$

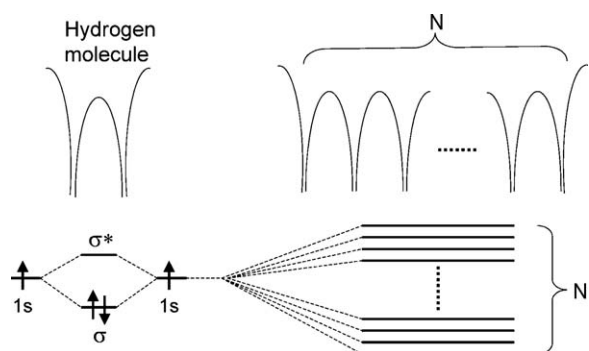


Fig. 1.1. Schematics of the energy levels of hydrogen molecule and the energy band formation of a 1-D crystal. The electron wavefunctions of the 1s orbital of the two H atoms overlap, resulting in molecular bonding (σ) and antibonding (σ^*) bonds with energy levels split. When a large number of N H atoms form a 1-D crystal, the overlap of the wavefunctions leads to the formation of N energy levels closely packed that can usually be considered as a continuum of an energy band.

where \mathbf{r} is the position vector, \mathbf{k} the crystal momentum vector, and $u_k(\mathbf{r})$ a function of the same periodicity of the lattice.

At this point, an important distinction must be made between inorganic semiconductors and organic semiconductors. Inorganic semiconductors have occupied and unoccupied energy levels, valence and conduction bands, respectively, that can extend over many unit cells. The semiconductor can be appropriately doped n-type or p-type. The interaction between charge carriers and the lattice is generally weak, and the transport of the charge carriers can be adequately described as delocalized Bloch waves in the bands. In organic semiconductors, the occupied and unoccupied energy levels for organic semiconductors are formed from planar structures of sp^2 bonds as well as π -bonds, and the π -bonds between carbon atoms in organic molecules usually form the highest occupied molecular orbital (HOMO) and lowest unoccupied molecule orbital (LUMO) in most OSCs. The interactions between the molecules are Van der Waals in nature and the electron wave function overlap between the molecules is small. The charge carriers are localized and surrounded by significant nuclear relaxation, and are better described together with the surrounding nuclear deformation as polarons instead of electrons or holes. As a result, the transport from one molecule to another is typically described by hopping of polarons [13]. Shown in Fig. 1.2 is a series of ultraviolet photoemission spectroscopy (UPS) spectra by Salaneck et al. on poly(2,5,2',5'-tetra-hexyloxy-8,7'dicyano-di-*p*-phenylenevinylene) (CN-PPV) doped with Na [14]. In the spectra, two new peaks, B and C, appear in the original band gap upon doping. In addition, the spectra indicate that the HOMO peak, marked A, remains at its position. No density of states (DOS) at the

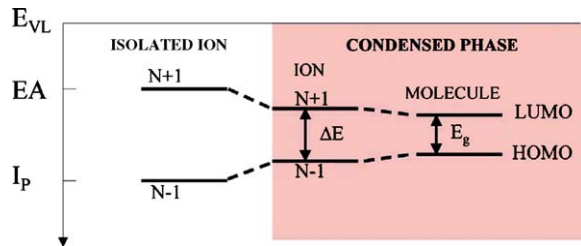


Fig. 1.3. Energy levels of an isolated molecular ion in vacuum and in a condensed phase. Removal of an electron into vacuum produces a cationic state of $N - 1$ electrons yielding the ionization potential I_p , and adding an electron to a neutral molecule produces an anionic state of $N + 1$ electrons giving the electron affinity level E_A .

Fermi level E_F is visible, suggesting the formation of a bipolaron lattice.

The polarization of the medium caused by the excess charge in OSC will affect both the energetics and the nature of the excited states in the OSC [13]. The simplified diagram in Fig. 1.3 shows a comparison between the energy levels of an isolated molecular ion and the levels of an ion in a condensed phase with the energy measured from the vacuum level. Removal of an electron into vacuum produces a cationic state of $N - 1$ electrons yielding the ionization potential I_p , and adding an electron to a neutral molecule produces an anionic state of $N + 1$ electrons giving the electron affinity level E_A . The polarization effects in the condensed phase cause the $I_p - E_A$ separation to decrease [13].

One of the most relevant parameters of a metal for organic device applications is the work function Φ . The work function can be defined as the difference in energy between an electron at rest in the vacuum outside a metal and an electron at the Fermi level (i.e. chemical potential of electrons inside the solid). The distance between the electron and the surface should be sufficiently large such that the (Coulombic) force due to the electron's interaction with its image in the solid is not felt. For metals, the work function depends both on the depth of the potential well by the ionic cores and the overspill of the conduction electron. Both quantities depend on the surface atomic geometry, and there is a strong variation in the work function for different surfaces of the same material, for example Cu(1 1 1), $\Phi = 4.94$ eV; Cu(1 1 0), $\Phi = 4.48$ eV [15]. For semiconductors and insulators, work function is not as important since the Fermi level depends sensitively on the charge doping of material. For these surfaces, more sensible parameters to use are the ionization potential and electron affinity.

1.2. Characteristics of interfaces in organic semiconductors

It is generally recognized that interfaces play important roles in organic semiconductor devices. Taking metal/organic interfaces as an example, the contact between a metal electrode and a single, a small group, or a thin film of molecules can play a critical, if not dominant, role in the performance of molecule-based electronics. The central issue is: how does an electron cross a metal–molecule interface? From a theoretical perspective, a quantitative answer to this question consists of three components: energetic alignment, electronic coupling, and dynamic localization due to polarization in nuclear coordinates. These three concepts are not unique to molecular electronics but have long been at the center of chemisorption studies [16].

The schematics of an ideal Schottky barrier formed between a metal and a semiconductor is shown in Fig. 1.4(a). The vacuum level at the metal/semiconductor interface is aligned, and as the thermal equilibrium is reached, the Fermi level of the bulk of the semiconductor is aligned with that of the metal. A charged region in the semiconductor forms with a voltage drop of eV_B equal to the contact potential difference between the metal and the bulk of the

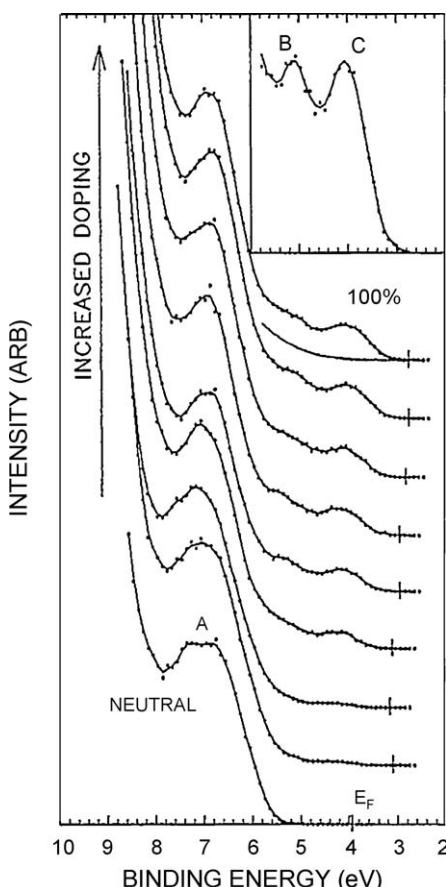


Fig. 1.2. UPS spectra of CN-PPV doped with Na. Two new peaks, B and C, appear in the original band gap upon doping, suggesting the formation of a bipolaron lattice (from Ref. [14]).

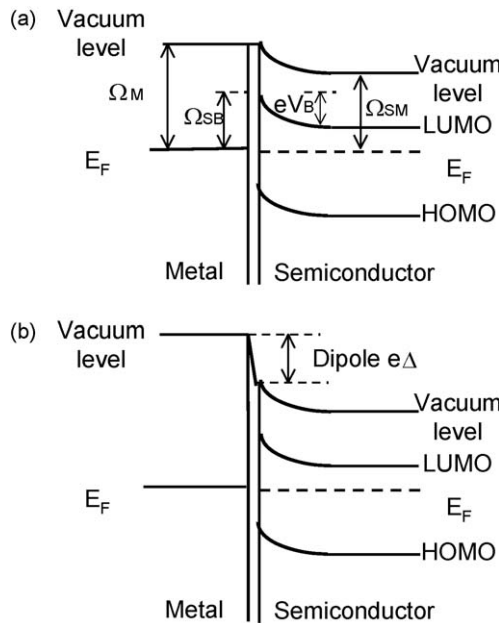


Fig. 1.4. The schematics of (a) an ideal and (b) a realistic Schottky barrier formed between a metal and a semiconductor. The ideal Schottky barrier height Φ_{SB} is simply the work function difference between the metal and the semiconductor, Φ_M and Φ_{SM} , respectively [17].

semiconductor. Here e is the absolute electron charge. The ideal Schottky barrier height Φ_{SB} is simply the work function difference between the metal and the semiconductor, Φ_M and Φ_{SM} , respectively [17].

$$\Phi_{SB} = \Phi_M - \Phi_{SM} \quad (1.2)$$

The schematics shown in Fig. 1.4(a) is for an n-type semiconductor with $\Phi_{SM} < \Phi_M$, and the depletion region width w is determined by the doping density N_D of the semiconductor from solving the Poisson equation [18]

$$w = \sqrt{\frac{2\epsilon_{SM}k_B T}{eN_D} \left(V_B - \frac{k_B T}{e} \right)}, \quad (1.3)$$

where ϵ_{SM} is the dielectric constant of the semiconductor, k_B the Boltzmann constant, and T the temperature. For undoped semiconductors, w approaches infinity, and therefore cannot be measured with surface analytical tools. On the other hand, if the semiconductor is doped, either intentionally or unintentionally by impurities in the semiconductor or by diffusion across the contact, band bending will occur and be measurable.

In general, the conventional picture of ideal Schottky barrier formation described by Eq. (1.2) and illustrated in Fig. 1.4(a) does not describe the behavior of a real metal-semiconductor interface. The realistic picture of the interface formation is given in Fig. 1.4(b), where an interface dipole Δ exists between the metal and semiconductor. The Schottky barrier height is therefore modified [18]

$$\Phi_{SB} = \Phi_M - \Phi_{SM} - e\Delta. \quad (1.4)$$

The interface dipole is established in part to satisfy the thermal equilibrium condition between the two materials. It can be facilitated by the surface states of the semiconductor, either intrinsic or induced by the metal contact. For organic semiconductors, the van der Waals nature of the interactions between the molecules results in low energetic expenses in severing the bonds at the surface, and as a result the existence of extensive intrinsic surface states is unlikely.

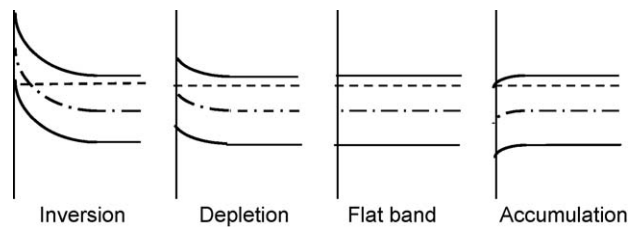


Fig. 1.5. Possible band conditions at the metal-semiconductor interface. The dash line is the Fermi level E_F in the bulk of the semiconductor. The dash-dot line represents E_i , the Fermi level of an intrinsic semiconductor that is approximately at the middle of the band gap.

There can be conditions in the interface region other than depletion as presented in Fig. 1.4. Shown in Fig. 1.5 is a summary of the possible conditions in a semiconductor. The dash line is the Fermi level E_F in the bulk of the semiconductor. The dash-dot line in the figure represents E_i , the Fermi level of the intrinsic semiconductor that is approximately at the middle of the band gap. All except the flat band condition have net charge in the semiconductor that brings it back to the bulk equilibrium from the interface. In the depletion condition, the net charge is from the ionized donors that are immobilized by the lattice. The width of the depletion region is given in Eq. (1.3). The semiconductor can also be characterized by the intrinsic Debye length [18],

$$L_D = \sqrt{\frac{\epsilon_{SM}k_B T}{e^2 N_D}}, \quad (1.5)$$

that is the length scale to screen off a potential of the order of $k_B T/e$. In the inversion condition, the intrinsic Fermi level E_i is above E_F at the interface, where the semiconductor is inverted from n-type to p-type. In this case, both the ionized donors and the holes contribute to the screening of the interface potential, and the width of the screening region is less than that in the depletion condition. For the accumulation condition, the majority charge carriers, in the case the electrons, are accumulated at the interface and screen the interface potential. The characteristic extrinsic Debye length for the accumulation condition is similar to that in Eq. (1.5), with N_D replaced by N_C , the effective density of states in the conduction band of the given material [19].

The energy level dependence on the doping density is fundamental for understanding the interaction between the dopant and the host system. The electron concentration is given by [19]

$$n = \int d\varepsilon D(\varepsilon) f_{FD}(\varepsilon), \quad (1.6)$$

where $D(\varepsilon)$ is the electron density of states and $f_{FD}(\varepsilon)$ the Fermi-Dirac distribution. For most crystalline inorganic semiconductors, $D(\varepsilon)$ is broad and smooth in comparison with $k_B T$, and in the non-degenerate limit Eq. (1.6) leads to

$$n = N_C \exp\left[\frac{-(E_C - E_F)}{k_B T}\right], \quad (1.7)$$

where E_C the conduction band minimum. If the doping density N_D is much larger than the intrinsic carrier concentration and full ionization can be assumed, the Fermi level position can be deduced as,

$$E_F = E_C - k_B T \ln\left(\frac{N_C}{N_D}\right). \quad (1.8)$$

Therefore, a linear dependence with slope of about $k_B T$ is generally expected for non-degenerate inorganic semiconductors.

Organic heterojunctions are critical for the application of OSC devices. The high efficiency of heterojunction OLED can be

attributed to the accumulation of electrons and holes at the heterojunction interface that facilitates efficient exciton formation and light emission [1]. The interest in charge separation (CS) and transfer (CT) across organic heterojunctions is prompted by its many uses in photoreceptor and imaging applications, and more recently, in organic photovoltaic devices. There is a fundamental difference between OPV and inorganic photovoltaic device (IPV) in the charge separation process. In IPV cells, electron–hole pairs are generated immediately upon light absorption under normal conditions throughout the bulk according to the exponential decrease of the incident light intensity. The exciton binding energy is in the range of meV in inorganic semiconductors, comparable to the thermal energy at room temperature, and the electron hole pairs can be easily separated by a build-in potential either through p-n junction or asymmetric cathode and anode [20]. In contrast, light absorption in organic materials almost always results in the production of a mobile excited state rather than a free electron-hole pair. Because the non-covalent electronic interactions between organic molecules, a tightly bound electron hole pair (Frenkel exciton or mobile excited state) is the usual product of light absorption in organic semiconductors. Furthermore, the dielectric constant of an organic material is usually low compared to inorganic semiconductors, and the attractive Coulomb potential is less screened than in inorganic semiconductors. The exciton binding energy, or the correlation energy between the localized electrons and holes, is substantially larger than the thermal energy at room temperature, and can be as high as 1.6 eV, resulting virtually no probability of thermal separation of the carriers [13]. The CS process, or interfacial dissociation of excitons only occurs at donor–acceptor (DA) interface, and the charge transport is driven by diffusion instead of build-in potential [20].

1.3. Interface growth mode and modeling

Organic molecules, when deposited onto an inorganic substrate, can result in three different growth modes (see Fig. 1.6) depending on the relative strengths of the adsorbate–adsorbate, and adsorbate–substrate interactions [21]. First, if the substrate is chemically inert, the adsorbate–substrate interaction will be very small having almost no influence on the growth of the organic film. This will enable the organic molecules to move freely on the surface and form large, separated islands of crystals after adsorption. This type of growth is known as Volmer–Weber or 3D-island growth (Fig. 1.6(a)). Second, if the substrate has highly reactive bonds, the adsorbate–substrate interaction will be very large, and as soon as the organic molecules hit the surface they will be bound strongly to the substrate. This will prevent self-ordering mechanism of the organic molecules, which is of crucial importance for ordered growth, hence result in disorder. This mode of growth is known as Frank–van der Merwe or layer-by-layer growth (Fig. 1.6(b)). Third type of growth is a moderate combination of the first two scenarios. That is, the adsorbate–substrate interaction is neither too strong, nor too weak. It is such that the substrate has strong enough influence on the deposited particles to impose its crystallinity to the grown organic film, and

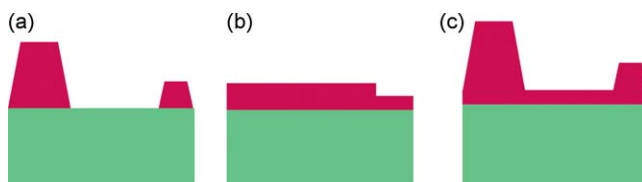


Fig. 1.6. Growth scenarios when organic molecules are deposited: (a) Volmer–Weber or 3D-island growth; (b) Frank–van der Merwe or layer-by-layer growth; (c) Stranski–Krastanov mode or layer+island growth.

the deposited particles have enough mobility to self-order themselves. This type of growth goes by the name of Stranski–Krastanov mode or layer + island growth (Fig. 1.6(c)).

In order to study the growth kinetics of a surface one can use the q th-order height–height correlation function, which can be defined as [21]

$$C_q(r, t) = \left(\left(\frac{1}{N} \sum_{i=1}^N |h(r_i, t) - h(r_i + r, t)|^q \right)^{1/q} \right), \quad (1.9)$$

where N is the number of sites with single valued heights $h(r_i, t)$. By definition, the $q = 2$ case refers to the height–height correlation function which is the rms fluctuation in the height difference between two surface points separated by a lateral distance r . It scales as follows according to the scaling hypothesis

$$C_2(r, t) \sim t^\beta g\left(\frac{r}{\xi(t)}\right), \quad (1.10)$$

where r is the lateral separation, t is time, β is a scaling exponent, and g is a scaling function which depends on r and ξ , where ξ is the correlation length. The correlation length is the critical distance over which two heights are correlated. $C_2(r, t)$ takes the following asymptotic behavior

$$C_2(r, t) \sim t^\beta. \quad (1.11)$$

Namely, for distances much larger than the correlation length, $C_2(r, t)$ increases as a power of time. β in the above equation is called the growth exponent. It characterizes the time-dependent dynamics of the growth. For distances much less than the correlation length ξ , $C_2(r, t)$ is independent of time for surfaces that obey the normal scaling law. It reads as

$$C_2(r, t) \sim \rho r^H, \quad (1.12)$$

where ρ is the local slope of the interface, and H is a second scaling exponent called the Hurst exponent. The Hurst exponent H characterizes the roughness of the saturated interface. As for the local slope ρ , it is literally the approximate average slope of the local structure. Its value is related to the intersection of $C_2(r, t)$ with the vertical axis. For normal scaling, it does not depend on time. If ρ does depend on time, the scaling becomes anomalous. As one can see, to be able to characterize a growing interface, one needs the height–height correlation function $C_2(r, t)$, and more specifically, the critical exponents H and β .

2. Experimental techniques

The electronic structure at interfaces with semiconductors is generally described by charting the energy levels such as the vacuum level, valence band, and conduction band as a function of distance from the interface. There are indirect electrical measurements capable of determining this profile but they generally rely on a theoretical model of the system to determine the general features of the interface with the electrical measurements merely determining the bounds of the energy and spatial values of the profile of the system. The technological success of devices whose performance is dictated by the interface characteristics has driven the development of increasingly sophisticated instrumentation designed to better probe the surface properties. Currently, there exist a large number of surface and interface analytical tools capable of providing complementary information [22–26]. The usefulness of these analytic instruments has been proven by their successful application in the study of inorganic semiconductor devices where the interfaces were found to dictate the performance of the device. Many have been successfully applied to study organic/metal interfaces, including photoemission spectroscopy (PES), inverse photoemission spectroscopy (IPES), scanning probe

microscopy (SPM) and spectroscopy, near edge X-ray absorption fine structure (NEXAFS), Kelvin probe (KP), photoelectron yield spectroscopy (PYS), internal photoemission (IPE), metastable atom electron spectroscopy (MAES), secondary ion mass spectroscopy (SIMS), reflection infrared spectroscopy (RIRS), high resolution electron energy loss spectroscopy (HREELS), low energy electron microscopy (LEEM), low energy electron diffraction (LEED), temperature programmed desorption (TPD), etc. In the following sub-sections, I will briefly discuss some of those more frequently used tools for the study of organic semiconductors.

2.1. Conditions for surface analysis

In any systematic surface study of materials, it is essential to recognize basic requirements dictated by the relatively low number of atoms of interest. For a given number of atoms N_A , the number of surface atoms scales as $N_A^{2/3}$. As such, a solid contains $\sim 10^{23}$ atoms/cm³, the surface has $\sim 10^{15}$ atoms/cm². The relative ratio of surface to bulk atoms presents a handicap when the probing depth exceeds several atomic layers, since the signal due to bulk atoms can quickly overwhelm that originating from the surface. A technique useful for surface analysis must therefore be sensitive to the electronic or structural properties of the relative small number of surface atoms. In addition, sample cleanliness is exceedingly important, because the interaction between the surface and contaminants will interfere with a clear characterization of surface properties.

A simple model of the interaction between the surface of a sample and the surrounding air molecules highlights the importance of a clean environment. Kinetic theory states that the rate k_p for the impact of atoms on a surface is given by [27]:

$$k_p = \frac{P}{\sqrt{2\pi m k_B T}}, \quad (2.1)$$

where P is the ambient pressure and m is the mass of the atoms. For nitrogen, if $T = 300$ K and $P = 10^{-6}$ Torr, then $\rho = 5 \times 10^{14}$ cm⁻² s⁻¹. If every atom that strikes the surface sticks, then a monolayer of nitrogen will grow in 2 s. Since surface contamination may result in interactions between the adsorbate and the substrate, it is necessary to minimize exposure of the sample to contaminants. Consequently, detailed surface studies require a highly controlled environment with a pressure on the order of 10^{-10} Torr. This range of pressure is usually referred to as ultra-high vacuum (UHV).

2.2. Photoemission spectroscopy

Photoelectron spectroscopy is based on the photoelectric effect explained by Einstein in 1905 [28], which relies on the creation of photoelectrons via interaction between the irradiating photons and the sample. Since the total energy must be conserved in this process, the kinetic energy, E_k , imparted to an electron satisfies [22]

$$E_k = h\nu - E_B - \Phi, \quad (2.2)$$

where Φ is the work function of the sample, $h\nu$ the photon energy, and E_B the binding energy of the initial state of the electron with respect to the Fermi level. Fig. 2.1 schematically summarizes this phenomenon. As indicated in Fig. 2.1, photoelectrons originate from energy levels occupied by electrons, including the valence band in inorganic semiconductors or HOMO energy levels for organic semiconductors as well as from core-level states, which correspond to closed atomic shells. The surface sensitivity of photoemission spectroscopy comes from the strong interaction of the photoexcited electron with the rest of the solid, resulting in a relatively short distance, or mean free path (MFP) λ , that it can travel before suffering an inelastic scattering. λ depends strongly

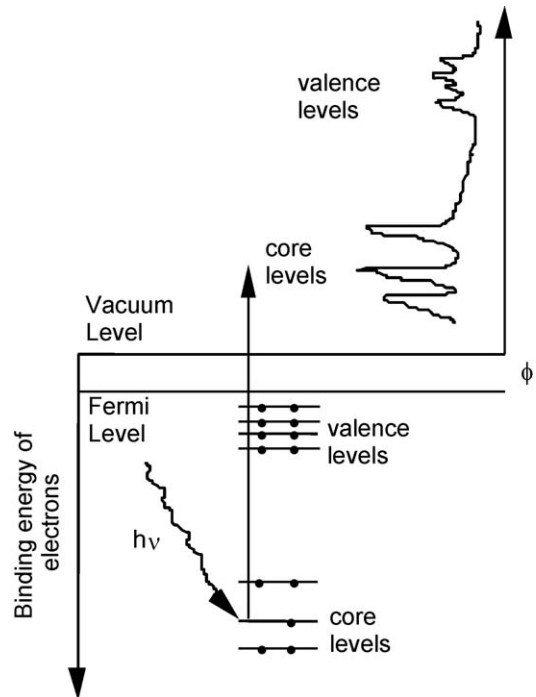


Fig. 2.1. A schematic representation of photoemission spectroscopy. Photoelectrons originate from energy levels occupied by electrons, including the valence as well as the core-level states.

on the kinetic energy of the photoelectron. The dependence on different materials is relatively minor. The MFP dependence on the kinetic energy has been summarized as the universal curve as shown in Fig. 2.2 [29]. The intensity attenuation of photoelectrons after passing through an overlayer of thickness d is given by

$$I = I_0 \exp\left(\frac{-d}{\lambda}\right), \quad (2.3)$$

where I_0 and I are the original and attenuated photoelectron intensity, respectively.

Photoemission spectroscopy has been extensively applied in the investigations of organic semiconductors as reviewed previously [4–8,30,31]. The techniques are customarily named accord-

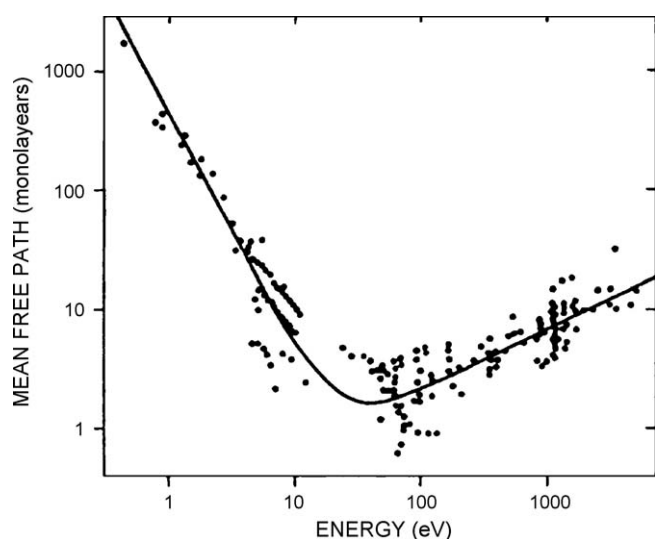


Fig. 2.2. Universal curve of electron mean free path in solids. The dots are measurement results of different materials (from Ref. [29]).

ing to the type of photon source used. Most commonly in-house ones are X-ray photoelectron spectroscopy (XPS) and UPS. In addition to XPS and UPS, synchrotron radiation, which requires expensive central synchrotron facilities, covers photon energies from infrared up to hard X-ray. Ultraviolet photoemission spectroscopy has been extensively used for studying organic semiconductor surface and interfaces. These photons are generated by a He gas discharge lamp, with an energy of 21.2 eV (He I) or 40.8 eV (He II). These low energy photons are restricted to probing the valence structure of samples. The line width of the UV lamp is small, only about 20 meV, which allows higher resolution spectra to be measured for the valence levels. Another benefit is that the interactions between these photons and the valence electrons have a higher cross section than with X-rays, allowing improved statistics for these measurements and thereby faster measurements. Finally, UPS is typically less damaging to the sample than XPS, a feature especially valuable to organic semiconductors that are usually vulnerable to photo induced damages and chemistry. The probing depth of UPS is typically $3\lambda = 15 \text{ \AA}$.

The UPS spectrum of a clean Au surface is shown in Fig. 2.3(a). The UPS spectrum clearly shows the Fermi level of the Au surface, which is used as a reference point to ensure that the binding energy scale is accurate. Since the Fermi level should remain constant for the system in thermal equilibrium it is only necessary to directly measure the Fermi level of a metal surface occasionally in order to ensure calibration of the energy scale. The Au 5d band is clearly

visible at around 5 eV binding energy. At a binding energy of ~ 16 eV is the low energy cutoff. This feature is composed of the electrons with the highest binding energy that the 21.22 eV photons are able to eject from the surface. Therefore by simply adding 21.22 eV to the low energy cutoff binding energy the binding energy of the vacuum level of the system relative to the Fermi level can be calculated.

The method used to determine the positions of the UPS features is shown in Fig. 2.3(b). The low energy cutoff position is defined as the highest binding energy of the measured electrons. This point is determined by linear extrapolating the high binding energy portion of the spectrum and finding the intersect with the background signal. The determination of the Fermi level position differs slightly due to the nature of the Fermi level. The measured Fermi level of a metal is expected to obey Fermi statistics and therefore the Fermi level is defined as occurring at the point where the energy level is half occupied, i.e., the midpoint of the leading edge of the spectrum, as illustrated in Fig. 2.3(b). In some practices, the vacuum level is marked at the middle of the cutoff edge instead of the more typical way of linear extrapolating. This is based on the ideal case that the cutoff of a uniform surface is a step function convoluted by the finite resolution of the electron energy analyzer, and the mid-point of the cutoff edge corresponds to the position of the step, in a way similar to the metal Fermi edge. The difference between the mid-point and the linear extrapolating is half of the electron energy analyzer resolution, typically ~ 0.1 eV in UPS. However, if the surface is not uniform, i.e., with a range of workfunction values, the cutoff edge will be broadened, and the linear extrapolating will be a better way to get the lowest workfunction of the surface.

If the surface is composed of a semiconductor the general features of the UPS spectra will be the same except for the fact that the Fermi level will not be measurable due to the lack of density of states in the band gap. The position of the valence structure can be used, in conjunction with the vacuum level, to calculate the ionization potential of the surface. For organic semiconductors the valence feature that is used to calculate the ionization potential is the highest occupied molecular orbital. The HOMO feature position is generally referred to by its low binding energy onset. This HOMO onset is determined by performing a linear fit of the low binding energy edge of the spectrum, and determining where that fit intersects the background signal, as shown in Fig. 2.3(b). UPS allows direct measurement of several important material properties by allowing measurement of the valence levels. The relative positions of the Fermi level, the vacuum level, the HOMO can all be measured. This allows calculation of the work function and ionization potential of the surface.

The most commonly used photon sources for XPS are the unmonochromatized K_{α} radiation from magnesium or aluminum targets. There are also monochromatized X-ray sources better energy and spatial resolution. The Al K_{α} and the Mg K_{α} lines peak at 1486.6 eV and 1254.6 eV, respectively. XPS is also commonly known as electron spectroscopy for chemical analysis (ESCA). XPS is based on the principle that the binding energy of a given photoelectron is highly dependent on the element from which the electron originates. Further, any change in the chemical environment of the atom probed by XPS causes a small chemical shift in the binding energy of a core-level electron. The core-level peaks are easily identified from a handbook of photoemission spectroscopy, although their exact positions depend on the chemical environments of the atoms.

In principle, the underlying physical interactions responsible for changes in the binding energies of different chemical species can be expressed in a straightforward fashion. In a first order approximation, the energy of a core-level electron depends on the Coulomb attraction of the nuclei and the repulsion of all the other

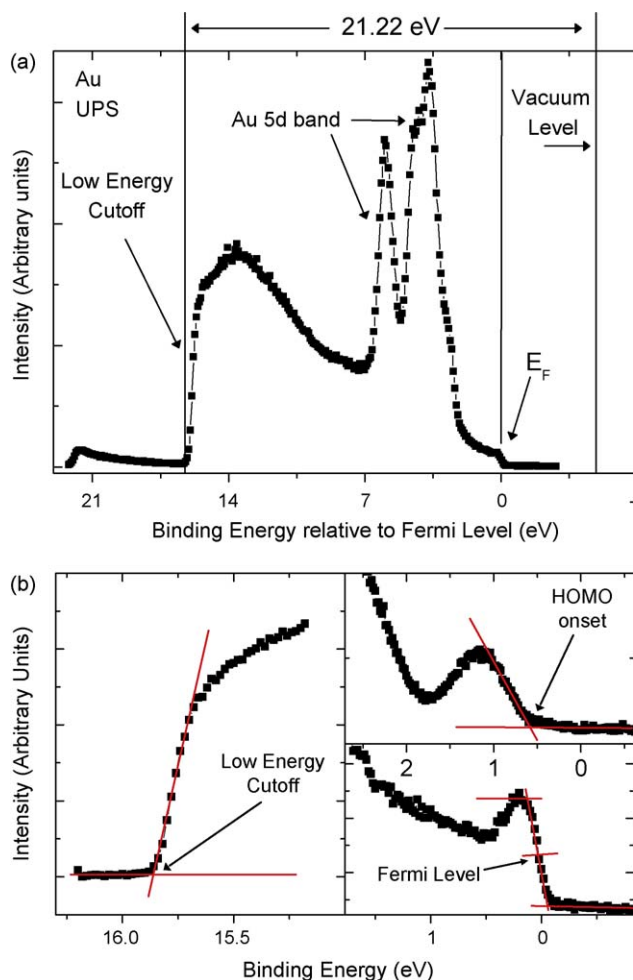


Fig. 2.3. (a) UPS spectra of a clean Au surface; (b) UPS feature position determination, including the low energy cutoff, the HOMO onset of a semiconductor, or the Fermi level of a metal.

electrons in the system, which neglects many-body effects. The change in the binding energy, ΔE , resulting from a change in the chemical environment will cause the HOMO energy level charges to redistribute. $\Delta E(A,B)$ of a particular core-level in two different compounds, A and B , was originally described by Gelius as follows [32]:

$$\Delta E(A,B) = K_c(q_A - q_B) + (V_A - V_B). \quad (2.4)$$

The first term, $K_c(q_A - q_B)$, describes the difference in the electron-electron interaction between core orbital, c , and the HOMO energy level charges, q_A and q_B , respectively. The coupling constant K_c is the two electron integral between core and HOMO energy level electrons. The second term in Eq. (2.4) has the character of a Madelung potential, which in the point charge approximation is defined as [12]

$$V_i = \sum_{i \neq j} \frac{q_j}{R_{ij}} \quad (2.5)$$

where the summation is over potentials arising from all the other ionic charges q_j centered at positions R_{ij} relative to the atom, i , in the material. Both terms in Eq. (2.4) are usually on the order of 10 eV. However, the summation of the two terms is on the order of a few eV or less since the ions attract the electron, while the HOMO energy level electrons repel the electron. As a result of this partial cancellation of the two terms, observed chemical shifts in solids are usually on the order of a few eV or less. Typical resolution for XPS is 1 eV, that can be improved to 0.5 eV by using a monochromatized X-ray source. The probing depth depends on the kinetic energy of the core level being probed and the material (see Fig. 2.2), and is usually taken as 50 Å. The elemental sensitivity and accuracy are about 1%.

If the momentum of the photoelectrons can also be measured in addition to the kinetic energy with an angle resolved electron energy analyzer, the electronic band dispersion $E(\mathbf{k})$ can be obtained if the sample is crystalline. The technique is termed angle resolved photoemission spectroscopy (ARPES) [33,34]. As the photoelectron goes across the crystal surface, its momentum parallel to the surface is conserved

$$\hbar k_{\parallel} = \sqrt{2mE_K} \sin\theta, \quad (2.6)$$

where m is the free electron mass and θ the exit angle of the photoelectron with respect to the surface normal. The perpendicular component of the momentum is not conserved, and it is related to that inside the crystal by

$$\hbar k_{\perp} = \sqrt{2m(E_K \cos^2\theta - V_0)} \quad (2.7)$$

where V_0 is the negative potential step inside the crystal.

As photoemission spectroscopy involves removing an electron from the molecule being probed, the measured photoelectron energy will depend on how well the hole left behind is screened by the environment, as it affects the Coulomb attraction of the hole and the departing photoelectron [8,16,35–52]. Shown in Fig. 2.4 are (a) six different environments for a single molecule, and (b) the resulting HOMO level shifts due to differences in polarization screening (from Ref. [39]). The gas phase (1) and isolated adsorbate (2) differ in ionization potential by ~0.4 eV, the gas phase (1) and the bulk film (5) differ by ~1.2 eV, and the gas phase (1) and the surface of the film (6) differ by ~1.0 eV. In Fig. 2.4(a), environment 5, three regions which surround a single molecule are labeled a, b, and c. From the above estimates, it can be concluded that the polarization due to regions a and c are ~0.2 eV each, and region b contributes ~0.8 eV. The minimum of I_p occurs at the completion of the first molecular layer (3), and the total polarization energy is 0.4 eV (metal surface) + 0.8 eV (region

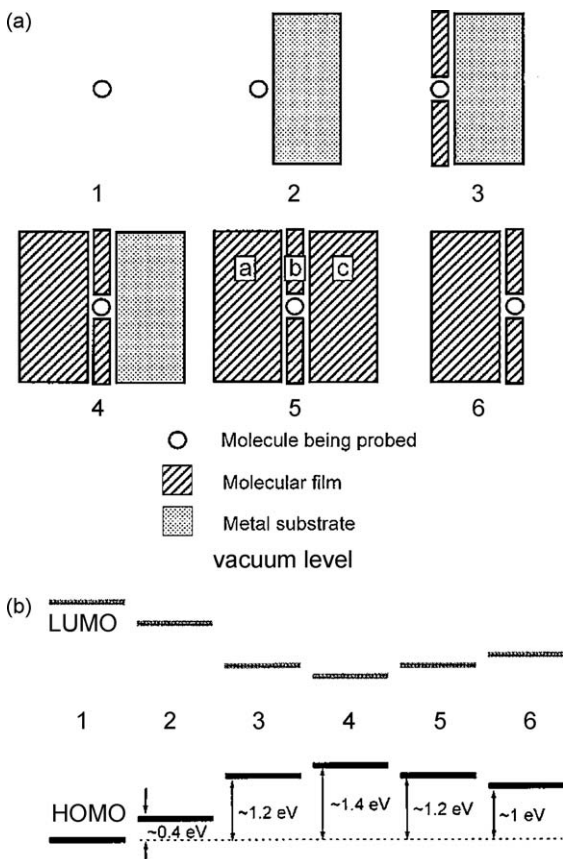


Fig. 2.4. (a) Six different environments for a single molecule, and (b) the resulting HOMO level shifts due to differences in polarization screening (from Ref. [39]).

b) ~1.2 eV. This implies that the I_p of the monolayer (3) should be ~0.2 eV smaller than that of the bulk surface (6), as verified by the experiment [39].

2.3. Inverse photoemission spectroscopy

Inverse photoemission spectroscopy is time reversed photoemission spectroscopy [53–57]. The surface under investigation is bombarded with electrons of a known kinetic energy, between 0 and 20 eV. These incident electrons radiatively decay into unoccupied energy levels. The ejected photons are then measured thus providing a direct measure of the unoccupied energy levels of the surface. There are two methods of performing this experiment. The first is to bombard the surface with electrons of a single kinetic energy and directly measure the spectrum of emitted photons using a spectrometer. The second approach is to vary the kinetic energy of the electrons and measure single photon energy. Given the energies of the incident electrons this technique has approximately the same surface sensitivity as UPS. Typical energy resolution ranges from 0.3 to 0.8 eV depending on the instrumentation [53–57].

The observed UPS spectrum is the representation of the filled states of a molecular cation resulting from the photoelectric process modified by the relaxation (polarization). The width of the peaks is presumably due to inhomogeneity of the film since the organic film is normally amorphous with random disorder. Therefore, the center of the HOMO peak corresponds to the HOMO energy of the most populous molecular cation, with the negative charge (photoelectron) at infinity (beyond vacuum level). Conceptually similar analysis applies to the IPES spectrum for the LUMO region. Induced by the injected electron, the relaxation (polariza-

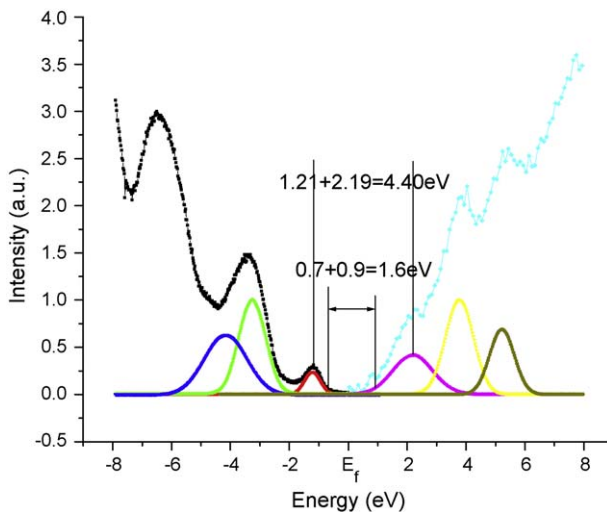


Fig. 2.5. UPS and IPES spectrum of CuPc. The energy gap can be deduced from the onset of the HOMO from UPS (left) and that of the LUMO from IPES (right).

tion) of the surrounding medium makes the IPES spectrum the representation of the relaxed anion instead of the neutral state of the molecule. Thus the energy separation of the HOMO–LUMO peaks obtained by UPS and IPES is the energy difference of relaxed positive and negative polarons separated at infinity, sometimes referred as energy gap (E_g) of the organic material. However, the charge injection into solid does not necessarily occur at the most populous or average species. Rather, when the injection is contact limited (usually the case in OLED devices), the charge injects to the molecules with the lowest energy difference to the Fermi level. The onset is defined as the extrapolation of the leading edge (closer to the Fermi level) in the spectrum. Similarly, the barrier for the electron injection will be from the Fermi level to the onset of LUMO. In most organic molecular devices the cathode and anode is separated far enough that the injection of hole and electron occurs at different molecules and beyond the size of the polarons. It is a general practice to define the onset of HOMO peak as the HOMO position of the copper phthalocyanine (CuPc) film, at -0.7 eV shown in Fig. 2.5. Similar term is used for LUMO position, at about 1.0 eV for the pristine CuPc film. The result is an injection energy gap (E_g) of about 1.6 eV, interestingly very close to the CuPc optical band gap E_{opt} (~ 1.7 eV).

2.4. Scanning probe microscopy

Scanning probe microscopy has transformed into an indispensable tool in the area of science and technology for the study of a whole range of materials properties in the nanoscale regime with very high spatial resolution [58,59]. SPM with its ever-expanding family enables us to characterize and correlate the materials properties such as topographical, mechanical, optical, electrical, thermal properties. The basic idea behind SPM techniques is straightforward. There is an interaction parameter, such as the tunneling current in scanning tunneling microscopy (STM), van der Waals, electrostatic, and capillary forces in atomic force microscopy (AFM), established between the microscope tip and the surface under investigation. The dependence of the interaction parameter on the distance between the probe and the sample is exploited in order to elicit information about the sample, and sometimes the tip. This is done by establishing a feedback mechanism based on the interaction parameter.

The ability of STM to achieve atomic resolution is owing to the fact that the tunneling current dependence on the height of the gap

(the distance between the tip and the sample) is exponential [58,59]

$$I_t = C \exp(-2\kappa d); \quad \kappa = (2m\Phi)^{1/2}, \quad (2.8)$$

where I_t is the tunneling current, κ is the wave function decay constant, d is the separation between the tip and the sample, and Φ is the work function of the metal substrate. Since STM relies on the tunneling current as its interaction mechanism, a sample must be conductive if it is to be operated on by STM. The above exponential dependence makes STM remarkably sensitive to the change in the separation between the STM tip and the sample. Shown in Fig. 2.6 is the STM picture of perylene-tetracarboxylic acid-dianhydride (PTCDA) deposited on highly oriented pyrolytic graphite (HOPG) taken in air [60]. It is remarkable that STM can obtain molecular resolution images if the organic overlayer is ordered. It also shows that the inertness of organic semiconductors allows molecular resolution with STM in air or water, while UHV is necessary for most metals and semiconductors because of the surface adsorption as described in Eq. (2.1) that usually induces chemical reactions.

Today's AFMs mostly use optical detection mechanism [58,59]. A laser beam is reflected off of the back of a cantilever, which has a very small protruding tip facing the surface whose radius of curvature is about 100 Å, that is attached to a piezoelectric ceramic scanner. As the cantilever is scanned over a surface, it is deflected up and down due to the local structure of the surface. This bending of the cantilever is detected through the movement of the laser that is reflected from the cantilever and hit the four-quadrant position sensitive photo-detector (PSPD). The level of the deflection is compared, by a computer, to a pre-determined set point value. Unlike STM, AFM can be used to measure the topography of insulators and semiconductors, as well as conducting materials. The most dominant force contributing to the deflection of the AFM cantilever is due to the interatomic van der Waals forces. The AFM can be operated in three different modes: contact mode, non-contact mode, and tapping mode (or intermittent contact), depending upon the distance between the tip and the sample during the scan, as shown on the plot. In the contact mode AFM (C-AFM), the tip is scanned over the surface in the repulsive force region while touching the surface "physically". In the non-contact mode AFM (NC-AFM), the tip is oscillated at a particular frequency

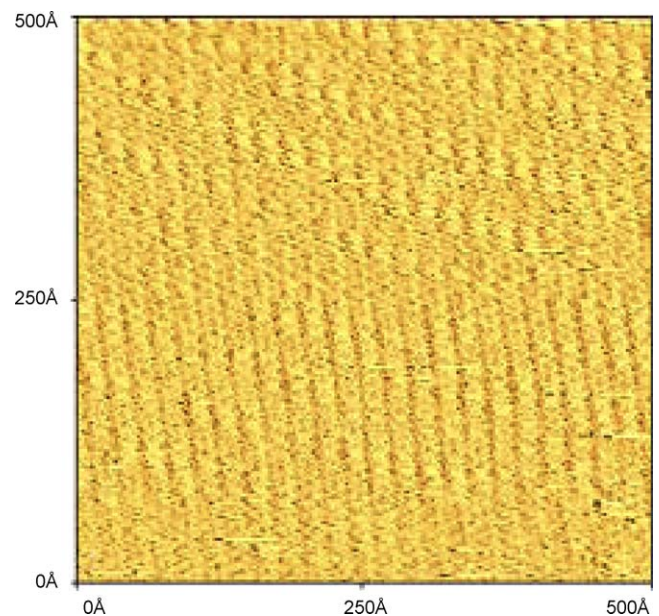


Fig. 2.6. Molecular resolution STM images of PTCDA deposited on HOPG taken in air (from Ref. [60]).

at relatively farther distances (in the order of 100 Å) from the surface during the scan and does not touch the surface. This regime is the attractive force regime of the van der Waals interaction. This is why NC-AFM enables imaging of soft samples without damaging the structure of the surface of the sample, where the surface can easily be damaged during a C-AFM scan. The third mode of AFM operation is the so-called tapping mode or intermittent-contact mode (IC-AFM). In this mode, the vibrating cantilever of the NC-AFM is brought closer to the sample (from attractive to repulsive regime) at the lower end of its travel to “tap” the surface. Since the friction between the tip and the sample is avoided in the tapping mode in contrast to C-AFM, and is more effective in its detection of the features of the surface than NC-AFM, it has become scanning mode of choice for a wide variety of samples.

2.5. NEXAFS, PYS, IPE, and SIMS

Near edge X-ray absorption fine structure is useful for investigating organic molecules on surfaces [61]. It can provide information about the bond angles, orientation, and unoccupied electronic structure of the adsorbed molecule. NEXAFS spectra are collected by exposing the sample to a monochromatic photon beam of varying energy, and monitoring transitions from a specific core-level to unoccupied states. These transitions, of course, obey the dipole selection rule. Following the excitation of the core-level electron, the core hole decays usually via an Auger process. Thus, the photon beam induces a current that changes as a function of excitation energy, allowing the determination of the electronic character of the unoccupied electronic states and inter-atomic bonding. The difference between NEXAFS and IPES in the measurement of the unoccupied electronic structure is that IPES corresponds to the $N + 1$ ionized state, while NEXAFS corresponds to the neutral state of the molecule. The polarization effects depicted in Fig. 1.3 must be included. Another distinction of NEXAFS is that it is sensitive to the element and dipole selection rules. NEXAFS requires the use of a synchrotron radiation source with photon energies high enough to excite core holes. The synchrotron radiation has a natural polarization that can be utilized to a great advantage in NEXAFS studies of the bonding and orientation of the molecule. The σ and π bonds of the molecule can have particular orientations on a surface. The angular dependence of the X-ray absorption can be used to track the orientation of resonant bonds according to the dipole selection rules [61].

Established by Lord Kelvin in 1898 [62], Kelvin probe is a surface analytical technique sensitive to the sample workfunction. The principle of KP is to find the bias dc voltage V_{b0} at which the ac current induced by the changing capacitance C is zero between the sample and an oscillating reference electrode positioned at a small distance from the sample,

$$i = \frac{dQ}{dt} = \frac{d(CU)}{dt} = U \frac{dC}{dt} = 0, \quad (2.9)$$

or, the vacuum level difference U across the capacitance equals zero,

$$U = \Phi_{\text{ref}} - \Phi - V_{b0} = 0, \quad (2.10)$$

where Φ_{ref} and Φ are the workfunction of the reference electrode and the sample, respectively. Because of the zero current condition, KP can give an accurate workfunction of the sample surface $\Phi = \Phi_{\text{ref}} - V_{b0}$ without the concerns of possible current induced artifact or ultrahigh vacuum conditions in PES. If it is measured in ambient or low vacuum environment, the measured workfunction may be dominated by the adsorbates as described in Section 2.1.

Photoelectron yield spectroscopy is another method to determine the work function Φ of a metal sample or, the ionization potential I_p if the sample is a semiconductor or an insulator. In PYS,

the total photoelectron yield Y is measured as a function of the incident photon energy $h\nu$. For metals, Y is proportional to the square of the excess of $h\nu$ over Φ [63],

$$Y = (h\nu - \Phi)^2. \quad (2.11)$$

For organic materials, Y is to the cubic of the excess over I_p [64],

$$Y = (h\nu - I_p)^3. \quad (2.12)$$

The advantages of PYS over PES in the workfunction measurement are similar to that of KP. It does require a tunable photon source with calibrated spectral intensity and energies exceeding the sample ionization threshold Φ or I_p , typically in the order of 5 eV. The Φ or I_p is determined by extrapolating the yield as a function of photon energy. The same principle is applied in internal photoemission, a process of charge carrier excited optically from one material (emitter) to another (acceptor) [65]. The process is similar to photoemission described in Eq. (2.2), except the photoelectrons (holes) are moving from the emitter into the acceptor instead of vacuum. In IPE measurements, photons are absorbed in a thin metal contact on organic, and the hot electrons (or holes) give rise to a photocurrent as they traverse the interface. The photocurrent yield is described by Eq. (2.11) with Φ replaced by the Schottky barrier height Φ_{SB} [66]. Given the typical value of Φ_{SB} of 1 eV, the tunable light source should work well in the infrared region.

In metastable atom electron spectroscopy, an excited metastable atom A^* is impinged onto the sample surface. The energy of the electron ejected from the sample S by the impact of A^* is measured, similar to that in PES. The process can be described as $S + A^* \rightarrow S^+ + A + e^-$ [67,68]. Typically He^* is used, and the electron energy and detection are very similar to those in UPS. The advantage of MAES over UPS is that it selectively detects the outermost surface layer, because the metastable atoms do not penetrate into the sample. The ultimate surface sensitivity extends to the outer most molecular orbitals, which interact more readily with the metastable atom. By comparison of MAES and UPS spectra, the orientation of the molecules in the top layer can be deduced.

Secondary ion mass spectroscopy is based on the observation by Thomson in 1910 that ion bombardment induces a release of positive ions and neutral atoms from a solid surface [69]. In SIMS, the composition of a sample surface is investigated by sputtering the surface with a focused primary ion beam and collecting and analyzing ejected secondary ions. These secondary ions are measured with a mass spectrometer to determine the elemental, isotopic, or molecular composition of the surface [70]. With elemental sensitivity in the range of parts per billion, SIMS is the most sensitive surface analysis technique for element composition. SIMS is often used for depth profiling when combined with a sputtering ion source, which can mill down the surface in a layer by layer fashion with vertical resolution ~100 Å (dynamic SIMS). A complication in quantitative SIMS analysis is the so-called “matrix effect” from the sensitivity of the ionization probability to the surface chemical composition. Another possible concern is “kick-in” of species by the primary or the milling ion beam [70].

3. Metal/organic interface

Metal/organic interface is a focus of both device engineering and basic science, since it is a key factor in nearly all important aspects of device performances, including operation voltages, degradation, and efficiency. The complexity of metal/organic interfaces is also intriguing in basic organic condensed matter physics. The energy level alignment and charge injection at the interface are among the most concerned fundamental issues. This is the area significant efforts in research are made and impressive improvement obtained [4–6,10,30,31,71]. Among the important

information obtained from photoemission studies, is the molecular energy level alignment at the interface of multilayer films.

3.1. Metal/organic interface dipole

The energy level alignment at the interface involves a number of physical and chemistry processes. In these processes, the most important ones related to the device performances include possible chemical reaction, interface dipole, diffusion, charge transfer and possible band bending. The vacuum level alignment (VLA) model is the earliest proposed model [4]. In this model, the vacuum level of metal cathode and ITO anode is simply aligned with that of the organic layer. As a result, the LUMO and HOMO shift inside the organic layer accordingly. Although used widely in the early days of metal/organic studies with various successes, this simple model have been disapproved by many studies, most persuasively by UPS studies [6]. The most important difference to VLA model is that the interface dipole model assumes that a dipole layer exists at the metal/organic and ITO/organic interfaces, as first suggested by Seki and his coworkers [72–79]. The interface dipole causes an abrupt shift of potentials across the dipole layer. The interface dipole layers at cathode and anode modify the LUMO and HOMO shifts inside organic layer. This model has gain its support mainly by various UPS and Kelvin probe works from the change of work function or vacuum level across the interface [6,37–41,50,72–214].

Several possible mechanisms may contribute to the interface dipole. In their review article [6], Ishii et al. listed six possible causes, as shown in Fig. 3.1, including (a) charge transfer across the interface, (b) image potential induced polarization of the organic material, (c) pushing back of the electron cloud tail out of the metal surface by the organic material, (d) chemical reactions, (e) formation of interface state, and (f) alignment of the permanent dipole of the organic material. Among these factors, (a)–(c) are more general in metal-organic interfaces, while (d)–(f) are specific to the individual metal-organic pair. These factors provide a plausible foundation to explain qualitatively the interface dipole formation. XPS analysis of the core level evolution indicates that (b) is unlikely to be a major factor contributing to the interface dipole formation. Should the polarization inside the organic molecule be significant, one would expect that core level peaks, especially that of the most common carbon atoms, would be broadened due to the intramolecular polarization. This is not generally observed for organic/metal interfaces. In fact, the lack of peak width change indicates that the dipole is predominantly confined to the interface between the metal surface and organic molecules.

As an example of organic/metal interface, the cutoff evolution of the UPS spectra of CuPc on Au by Yan et al. [172] is shown in Fig. 3.2. It is clear that most changes occur at the very first layer of CuPc. Smaller changes continue when more CuPc is deposited. Most of the additional shift may be attributed to the polarization effect or

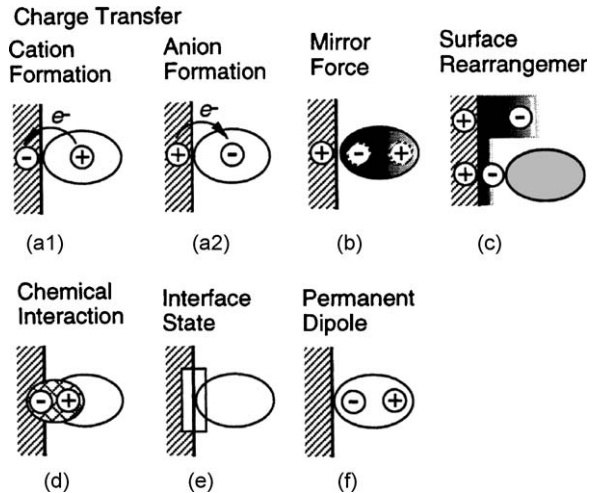


Fig. 3.1. Models for metal-organic interface dipole layer formation (from Ref. [6]).

extended charge diffusion, and is unlikely to be a result of the interface dipole. From Fig. 3.2 we can therefore estimate that the interface dipole is about 0.8 eV at CuPc/Au. Shown in Fig. 3.3 is the interface dipole at metal and tris(8-hydroxyquinoline) aluminum (Alq) interfaces as a function of the metal work function [172]. The positive dipole is defined as pointing away from the metal surface. The data show approximately linear behavior, be it metal deposited on organic (Na/Alq, Ca/Alq, Al/Alq) or organic deposited on metal (Alq/Ca, Alq/Mg, Alq/Au). The slope of the straight line is -0.8. Similar linear dependence on metal work function has also been observed for other organic materials by my group and by several other groups [6,97,172].

Extra care should be taken in calculating the dipole for the case of metal deposited on organic. For organic not undergoing destructive chemical reactions, all the energy levels of the organic should shift the same amount to the first order of approximation, corresponding to the change of the Fermi level in the organic. As a result, the interface dipole is not the vacuum level shift observed in UPS alone, but the difference between the vacuum level and the core level shift.

Further quantitative understanding of the interface dipole formation can be obtained by realizing that the metal and organic material must reach thermodynamic equilibrium when in contact. Tung devised a model of inorganic semiconductor/metal interface based on charge transfer and thermodynamic equilibrium between the metal and semiconductor [215]. According to his model, the interface dipole is given by

$$\Delta = \frac{-ed_{MS}N_B}{\varepsilon_{it}} \cdot \frac{\Phi_M - (I_p - E_g/2)}{E_g + \kappa}, \quad (3.1)$$

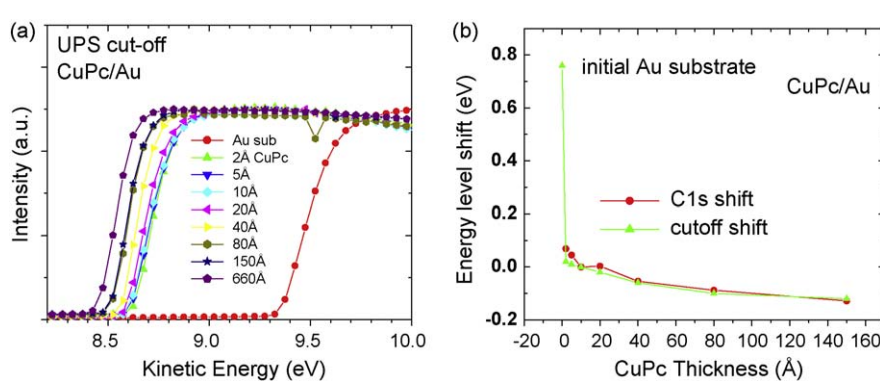


Fig. 3.2. Determination of interface dipole at CuPc/Au interface: (a) normalized cutoff of UPS spectra; (b) comparison of cutoff shift and the C 1s shift (from Ref. [172]).

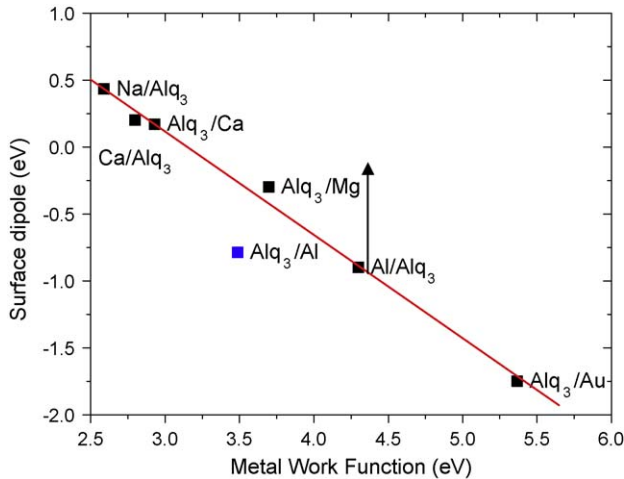


Fig. 3.3. Interface dipole at metal and Alq interfaces as a function of the metal work function. The arrow shows the dipole when the metal work function equals the midgap energy (from Ref. [172]).

where d_{MS} is the distance between metal and semiconductor atoms at the interface, N_B the density of bonds through which charge transfer takes place, ε_{it} the dielectric constant in the interface region, and κ the sum of all the Coulombic interactions for charges at different sites. The model suggests that charge transfer is a primary mechanism of Schottky barrier formation, and a good agreement with the experimental results is found for polycrystalline inorganic semiconductors [215]. It should be emphasized that the model is based on thermodynamic equilibrium, facilitated by the interface bonds, of electrons across the interface between the metal and semiconductor. It therefore does not depend on the details of the interface reactions, so long as the physical properties of the semiconductor, such as I_p and E_g , still remain intact at the interface. The model does not apply to interfaces where strong chemical reactions result in the domination of the interface by new reacted species.

The charge transfer is not the only factor in determining the interface dipole. A closer inspection of Eq. (3.1) reveals that the

thermodynamic equilibrium model implies that the Fermi level is shifted toward the mid-gap of the semiconductor by the interface dipole, and the interface dipole changes sign as the metal work function goes across the mid-gap energy. However, from the fitted data in Fig. 3.3, this sign change occurs at $\Phi_M = 3.2$ eV, 1.1 eV lower than the Alq mid-gap energy of 4.3 eV. In fact, an interface dipole of -0.9 eV is seen at the mid-gap energy indicated by the vertical arrow in Fig. 3.3. This apparent deviation from Eq. (3.1) is attributed to the combination of pushing back of the electron cloud by the organic material and the permanent dipole momentum of the organic [172]. On a metal surface, the electron cloud extends out of the surface defined by the positive ion cores of the metal. The relative displacement of the charge distribution produces a dipole layer pointing away from the surface, and a negative dipole potential, V_{tail} , seen by the electrons. Theoretical values of V_{tail} varies for different metals and facets but is usually about a few tenths of an eV, the same order of magnitude as observed [216]. When the electron cloud tail is pushed back by the organic material, its contribution to the metal work function is also eliminated. As a result, the sign change in the metal–organic interface dipole shifts from the organic mid-gap energy toward a lower energy.

The detailed interface dipole formation inevitably depends on the atomic/molecular orientation of the substrate and overlayer. One example is given by Ueno and his coworkers, who investigated the formation and molecular orientation of monolayers of OTi-phthalocyanine (OTiPc) and CuPc/OTiPc on cleaved highly oriented pyrolytic graphite with combined use of UPS and metastable atom electron spectroscopy, and observed the layer-by-layer dependence of the interface dipole that is strongly associated with the molecular orientation [131]. Fig. 3.4 shows a summary of the energy levels and E_F alignment for OTiPc (oriented monolayer)/HOPG, OTiPc(bilayer)/HOPG, CuPc/HOPG, and CuPc(monolayer)/OTiPc(oriented monolayer)/HOPG [131]. Measured vacuum level positions and interface dipoles are also shown. The difference induced by the interface dipole between the binding energy of the HOMO of the OTiPc(oriented monolayer)/HOPG and that of the OTiPc(bilayer)/HOPG, $\Delta E_{HOMO}(OTiPc)$, is 0.24 eV, while the difference, $\Delta E_{HOMO}(CuPc)$, between the HOMO of CuPc(monolayer)/HOPG and of the CuPc(monolayer)/OTiPc(oriented monolayer)/HOPG is

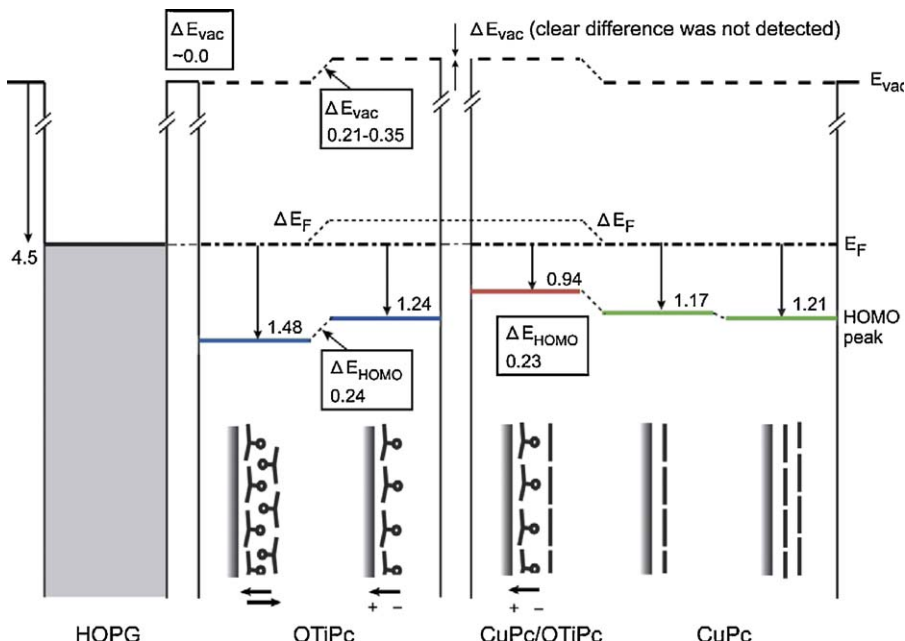


Fig. 3.4. Energy diagram for the HOMO levels and Fermi level for OTiPc/HOPG, CuPc/HOPG, and CuPc/OTiPc/HOPG systems. Layer-by-layer dependence of the interface dipole is observed that is strongly associated with the molecular orientation (from Ref. [131]).

0.23 eV. It is concluded that thermodynamic equilibrium is achieved for these molecular layer sandwich system, and that the interface dipole layer induces a change in binding energy of the valence states of the organic overlayer equal to the potential step introduced by the dipole layer in thermodynamic equilibrium [131].

The delicate orientational change of the molecules can show strong features in metastable atom electron spectroscopy [131]. Fig. 3.5 shows the upper valence band region measured with He I UPS and He^{*} MAES on: (1) OTiPc (~2–3 monolayer (ML)) as-grown on HOPG kept at room temperature (RT) (measured at RT), (2) OTiPc film (oriented monolayer) on HOPG obtained by annealing (1) at 573 K for 9 h (measured at RT), (3) annealed OTiPc film (oriented monolayer) after cooling (2) to 123 K (measured at 123 K), (4) CuPc ~ 1 ML deposited on the OTiPc monolayer kept at 123 K (CuPc/OTiPc/HOPG)(measured at 123 K), and (5) CuPc/OTiPc/HOPG heated up to 373 K (measured at 373 K) [131]. The HOPG substrate spectrum is also shown for comparison in the bottom of Fig. 3.5. The MAES spectra (2) and (3) clearly show that the oxygen nonbonding state, marked as peak C in Fig. 3.5, appears after annealing, indicating that the film consists of OTiPc molecules with upward orientation. When 1 ML CuPc layer is deposited on the oriented OTiPc monolayer kept at 123 K, peak C disappears, indicating that the outermost surface of the OTiPc film is covered by CuPc molecules. It is in sharp contrast to the corresponding UPS spectra that show little change. Peak C remains undetectable even at 373 K. Furthermore, no increase is observed in the intensity of the σ (C-H) bands that are effectively excited by He^{*} only when the molecular plane is tilted. These results indicate that (i) the outermost surface of the CuPc/OTiPc/HOPG consists of molecules oriented flat with respect to the substrate and (ii) there are few, if any, OTiPc molecules in the outermost surface layer. In UPS, the most characteristic change of the spectral feature is seen in the HOMO band A. The results also show the sensitivity of MAES to the outer most molecular layer [131].

Another aspect to explain the interface dipole formation and energy level alignment at metal/organic interface is proposed by

Kahn and his coworkers [140,142,184,185,217]. They propose that the metal/molecule interaction broaden the molecular levels, so that the initial delta-like distribution of the isolated molecule is transformed into a continuum density of states with, in particular, non-negligible density in the molecular energy gap. The position of the charge neutrality level (CNL) is such that the total integrated density of states up to the CNL accommodates the number of electrons in the isolated molecule. The charge transfer at the interface is controlled by the difference between the metal Fermi level and the organic CNL. The offset between the CNL of the organic molecule and the initial metal Fermi level, or work function Φ_M if its position is referred to the vacuum level, determines whether and in which direction charge is transferred between the metal and the organic molecule. The charge transfer induces an interface dipole, which tends to align the Fermi level, E_F , and the CNL. A measure of this drive to align the E_F and the CNL is given by S , which depends directly on the DOS around the CNL, and relates the initial and final energy difference by

$$E_F - E_{\text{CNL}} = S(\Phi_M - E_{\text{CNL}}). \quad (3.2)$$

The implication of Eq. (3.2) is that the energy-level alignment at metal/organic interfaces is characterized by S , the CNL, and the work function Φ_M of the metal. The CNL plays the role of an effective Fermi level for the organic material and S acts as a screening parameter, which determines how the initial energy difference $\Phi_M - E_{\text{CNL}}$ is to be screened. For CuPc/Au, it was obtained $S \sim 0.19$ and an interface dipole of $\Delta = 0.9$ eV, compared to the experimental value of $\Delta \sim 1.2$ eV. An important requirement is the weak sensitivity of the organic CNL to the metal/organic interaction, and it is crucial that the CNL be taken as an intrinsic property of the organic material, nearly independent of the metal on which it is deposited [140,142,184,185,217].

Lee et al. suggested that the interface dipole and charge-injection barrier at organic/metal interface should be better described as a linear function of the metal electronegativity [218]. This is because the metal workfunction Φ_M is considered to

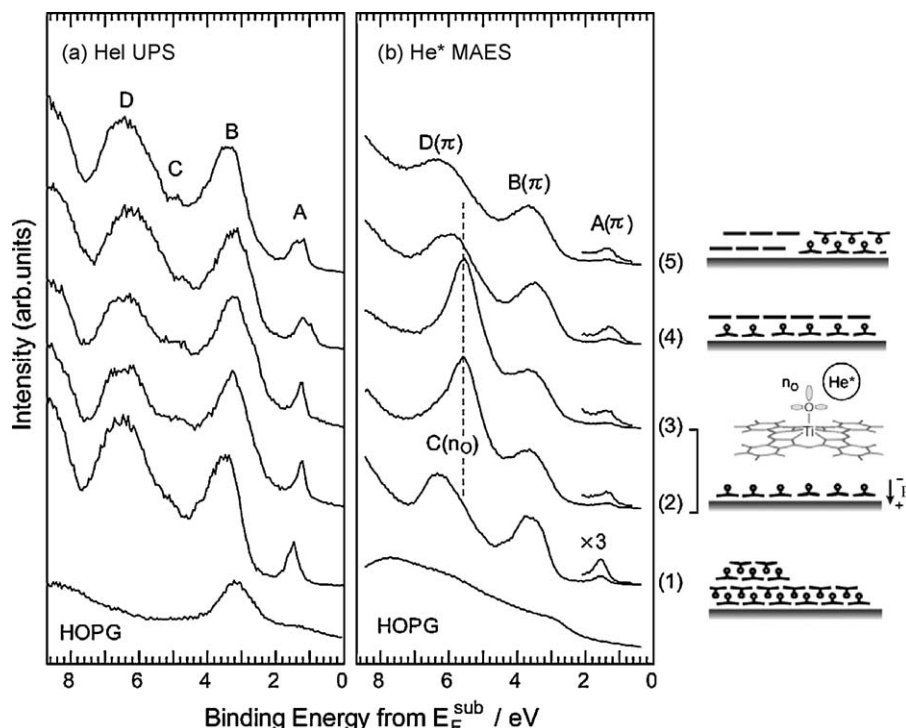


Fig. 3.5. UPS (a) and He^{*} MAES (b) spectra of the upper valence band region of 5 systems. The results show the sensitivity of MAES to the outer most molecular layer (from Ref. [131]).

be composed of two terms. One is related to the bulk contribution to the metal work function, denoted as Φ_{mb} the internal work function [219]. The other contribution to Φ_M is attributed to an additional surface dipole layer caused by the tailing of the electron cloud out of the metal surface. It can be described as the change of the electrostatic potential in the vacuum side. When the organic/metal interface forms, the electron cloud deforms and the second contribution changes. As a result, the quantity, Φ_M should be considered as pseudo-bulk rather than a bulk quantity and it may not be expected to account well for the interface dipole and charge-injection barrier at organic/metal interfaces. It is suggested that the metal electronegativity E_A rather than its work function Φ_M is a more appropriate quantity to characterize the metal/organic semiconductor interface, as earlier proposed for metal/inorganic semiconductor interfaces [220].

While photoemission spectroscopy has provided the most direct evidence on the interface dipole formation and energy level alignment, other analytical tools have also been used to measure these quantities such as internal photoemission [113,181,191, 221–223]. For example, Campbell and Smith measured IPE and photocurrent versus bias to determine metal/Alq Schottky energy barriers for a range of contact metals with work functions from 2.7 eV (Sm) to 5.6 eV (Pt) [221]. The electron Schottky barrier for low work-function metals (<about 3.6 eV) was pinned at about 0.6 eV. For metals with higher work functions (>about 3.6 eV) the ideal Schottky model was taken to be accurate. It remains to be resolved that how the results from IPE can be related to those from photoemission spectroscopy.

3.2. Charge transfer and chemical reaction

The descriptions of the metal/organic interface in Section 3.1 are idealized for abrupt interfaces and it may not apply for interfaces with heavy intermixing or strong chemical reactions. In these processes, the most important ones related to the device performances beside interface dipole include possible chemical reaction [40,41,82,98,112,129,159,162,168,202,224–255], diffusion [72,98, 170,223,231,243,249,256–276], charge transfer [7,14,31,37,51,

52,71,114,125,128,148,150,162,164,167–172,176,183,184,188,189, 193,197,200,206,207,210,228,230,235,238,239,241,268,277–322] and possible band bending [94,323,324].

Other effects, such as the ordering and facet of the materials and changes in the organic material by the charge transfer, chemical reactions, in-diffusion of the metal atoms, and metal cluster formation are not included. At most interfaces in organic semiconductor devices, more than one type of interactions can and do occur. Other major factors affecting metal/organic interface formation include the thermal energy of the material being evaporated, the topology of the substrate, the condensation energy on the surface, and the growth mode of the deposited film. For the process of organic deposited on metal (denoted as organic/metal), the diffusion/disruption between the two materials is low except the most reactive metals, since the thermal energy of the evaporated organic molecules is generally low due to the low evaporating temperature. The organic material normally arrives at the surface in the molecular form, and later condenses to form thin films. The condensation energy of the organic material on the surface is low due to the nature of van der Waals interaction that bonds the organic molecules. Comparing to organic/metal interfaces, there are significantly more diffusion and disruption at the metal/organic interfaces (deposit metal onto organic film), because the hot metal atoms have larger kinetic energies, which makes the penetration of metal atoms into the organic film fairly easy. Also, the metal arrives as isolated atoms or atom clusters that will give a high condensation energy, resulting in possible damage or reaction with the organic. The relative sizes of the organic molecule and metal atom are very different. The smaller metal atoms may easily fall into the “valleys” of the organic molecules. This fact requires one to exercise caution when interpreting the energy level changes at the initial metallization process.

An example of a metal/organic interface chemical reaction is Ca deposited onto Alq, where a staged interface formation is observed to initialize by charge transfer and then chemical reaction. In Fig. 3.6, the evolution of XPS C 1s, O 1s and N 1s core level electron density curves (EDCs) are plotted as a function of increasing Ca thickness Θ_{Ca} on Alq by Choong et al. [301]. At $\Theta_{Ca} = 0 \text{ \AA}$, these core

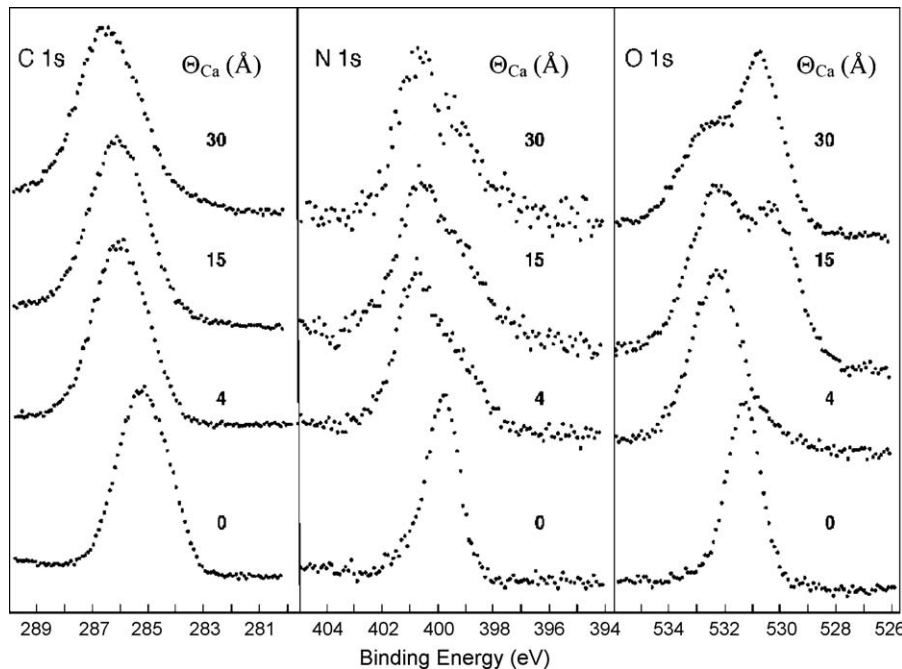


Fig. 3.6. Evolution of XPS C 1s, O 1s and N 1s core level electron density curves (EDCs) as a function of increasing Ca thickness Θ_{Ca} on Alq. The new components in N 1s and O 1s are signatures of interface charge transfer and chemical reaction (from Ref. [301]).

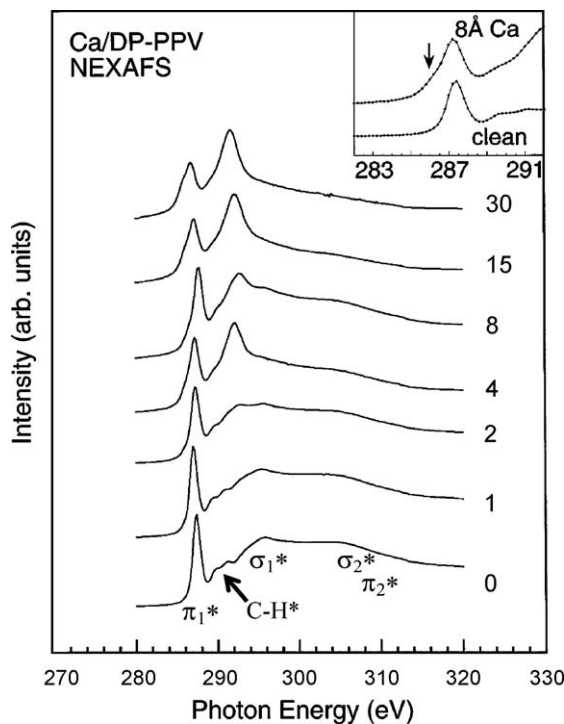


Fig. 3.7. Evolution of the NEXAFS spectrum during the deposition of Ca on DP-PPV. The changes after $>4 \text{ \AA}$ Ca reflect charge transfer across the metal/polymer interface (from Ref. [325]).

level EDCs are gaussian in shape and composed of only one component, which indicates a clean Alq film. As early as $\Theta_{\text{Ca}} = 1 \text{ \AA}$, a new component is observed in the N 1s EDCs. Conversely, the O 1s EDCs remain single component until $\Theta_{\text{Ca}} = 4 \text{ \AA}$, indicating that the phenoxide side of the ligand is relatively unaffected by the presence of Ca. As more Ca is deposited, the O 1s EDC splits and a new reacted component occurs at lower binding energy, which increases in intensity and shifts back to higher binding energy with increasing Ca coverage. The intensity and position of the reacted N 1s component remain almost constant with coverage above about 4 \AA . Clearly Ca first interacts with N atoms in the Alq molecule until the Ca-N interaction is saturated, followed by a Ca-O reaction. The interaction between Ca and N is a charge transfer process yielding a stable Alq radical anion and Ca^{2+} , resulting in one of the three quinolates of Alq accepts the electron donated by Ca before the structural deformation of the Alq allows the chemical reaction

between Ca and O. Metallic Ca forms after 15 \AA of Ca is deposited [301].

The charge transfer process in the early stage of metal/organic interface can also be investigated with near edge X-ray absorption fine structure measurements. Fig. 3.7 shows the evolution of the NEXAFS spectrum of poly(2,3-diphenylphenyl vinylene) (DP-PPV) during the course of Ca deposition by Ettedgui et al. [325]. The spectrum of clean DP-PPV reflects contributions primarily from the phenylene portion of the molecules, and the features near 287, ~ 290 , and $293\text{--}315 \text{ eV}$ are attributed to the π_1^* , π_2^* structures, and the σ_1^* and σ_2^* regions, respectively. Following the deposition of Ca, an increase within the leading edge of the π_1^* resonance is found in the photocurrent compared to that of the clean sample, indicating the formation of new intra-gap states. The changes in the unoccupied states of DP-PPV following the deposition of Ca may result from charge transfer across the Ca/DP-PPV interface. The creation of these additional unoccupied states at the Ca/DP-PPV interface may enhance charge injection by providing additional sites for electron transfer into the polymer near the Fermi level of the metal. A strong feature at photon energy of 291 eV is also induced by Ca deposition, which may be attributed to the deformation of the molecular geometry [4] or the formation of polarons and bipolarons [325].

Interface chemical reaction between metal and organic can be immediate upon deposition without an initial charge transfer stage. The evolution of the XPS O 1s, N 1s, Al 2p, and C 1s spectra at representative coverages (Θ_{Al}) of aluminum on Alq by Le et al. [239] is shown in Fig. 3.8. The XPS spectra were normalized to constant intensity for comparison purposes. The bottom curve in each set represents pristine Alq, and can be fit very well by a single component, Gaussian line shape. All core levels showed significant broadening and shifting to higher binding energy with increasing aluminum deposition. However, the more detailed behaviors are very element specific. The C 1s exhibits only the above mentioned broadening and shifting as does the Al 2p up to a coverage of $\Theta_{\text{Al}} = 4 \text{ \AA}$ where a low binding energy component begins to emerge. The O 1s develops a distinct asymmetry to the high binding energy side while in the N 1s spectrum, a broad feature appears to evolve on the low binding energy side of the principal peak. In contrast to Ca/Alq [301], where the nitrogen spectrum is singularly influenced by the metal interaction, it is the oxygen emission that is most significantly affected in the Al/Alq. Above $\Theta_{\text{Al}} = 4 \text{ \AA}$, the intensity of the reacted O 1s component remains essentially constant. The broadening of the Al and C spectra is simply due to the greater diversity in chemical states and environments of the atoms. While both the original Alq aluminum and the deposited aluminum are bonded to oxygen, both the

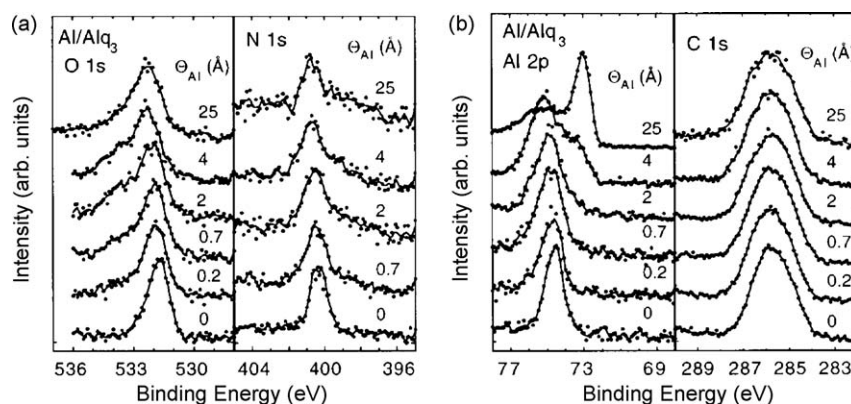


Fig. 3.8. Evolution of XPS O 1s, N 1s, Al 2p, and C 1s spectra as a function of aluminum coverage observed at the Al/Alq interface. All core levels showed significant broadening and shifting to higher binding energy with increasing aluminum deposition. (from Ref. [239]).

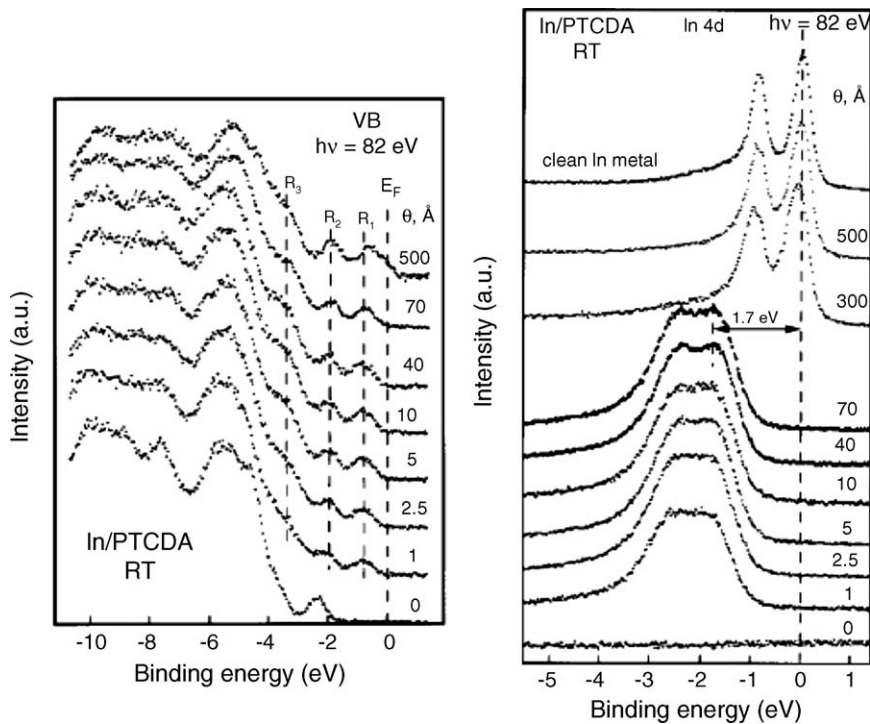


Fig. 3.9. Spectra of (a) the valence band and (b) In 4d core levels, obtained with UPS and XPS, respectively, at selected nominal In deposition thicknesses on PTCDA. The data indicate that In diffuses at a very high rate into PTCDA without any surface accumulation (from Ref. [231]).

coordination and charges are different and at least a modest increase in line width is to be expected. The low binding energy peak that first appears in the Al 2p spectra at $\Theta_{Al} = 4 \text{ \AA}$ is simply due to unreacted, metallic aluminum. The intensity of this peak increase with coverage while that of all the other elements decreases as a true metallic film is formed. A clear demarcation is seen in the core level spectra for coverages above and below $\Theta_{Al} = 4 \text{ \AA}$. For $\Theta_{Al} \geq 4 \text{ \AA}$, the binding energies and line widths are virtually independent of coverage and all of the added aluminum is found in the metallic state. This clearly indicates that the reaction is limited within the first 4 Å of deposited aluminum. While a 4 Å layer of aluminum would be extremely thin, the modified layer which would result from a reaction between the deposited aluminum and the Alq would be much thicker. Due to the extreme difference in molecular/atomic sizes, 0.2 Å of aluminum corresponds to approximately one metal atom for every surface Alq molecule. If each deposited aluminum atom reacts with one Alq molecule and can freely diffuse into and react with the bulk Alq, then an $\approx 4 \text{ \AA}$ deposition would produce a reacted layer of $> 150 \text{ \AA}$. This also explains why such dramatic spectral changes occur when only 0.2 Å of metal are deposited [239].

3.3. Diffusion and cluster formation

There can be substantial metal diffusion into organic materials [72,98,170,223,231,243,249,256–276]. Shown in Fig. 3.9 are the spectra of (a) the valence band and (b) In 4d core levels, obtained with UPS and XPS, respectively, at selected nominal In deposition thicknesses on 3, 4, 9, 10 perylenetetracarboxylic dianhydride (PTCDA) by Hirose et al. [231]. The intensities and line shapes of the VB and In 4d spectra remain unchanged beyond coverage of a few angstroms. Indium clustering is ruled out by the absence of metallic states at E_F (Fig. 3.9(a)) and in In 4d (Fig. 3.9(b)) at coverages as high as 70 Å. Several hundred angstroms of In are necessary to obtain evidence of metallicity. It is concluded that In diffuses at a very high rate into PTCDA without any surface

accumulation, so that surface metallization is obtained only after the saturation of the organic film with metal atoms. The interfacial region is very wide due to an anomalously fast diffusion of In into the organic layer. The absence of metal clustering, which permits diffusion, is believed to be due to the ionization of In and ion–ion repulsion in the PTCDA matrix [231].

Secondary ion mass spectroscopy is a very effective tool to probe diffusion. SIMS spectra of 1000 Å CuPc on 15 Å Li, deposited on a Au covered Si wafer by Yan et al. [305] are shown in Fig. 3.10. The x-axis is the sputtering time, which is roughly proportional to the probed depth from the sample surface for the homogenous layer. The left vertical line in Fig. 3.10 is the estimated position of the interface of the CuPc and Li, and the right line is that of Au/Si. The interfaces are reasonably sharp given the instrumental resolution $\sim 100 \text{ \AA}$. Inspecting the Li depth profile in the film, it is remarkable that Li has diffused up to the very top of the surface,

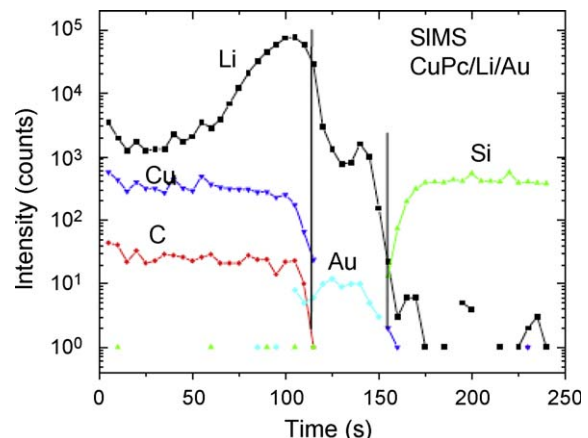


Fig. 3.10. SIMS spectra of a 1000 Å CuPc/15 Å Li/Au/Si wafer. It is remarkable that Li has diffused up to the very top of the surface (from Ref. [305]).

despite that it is laid down on the Au substrate before the CuPc so that there is no thermal kinetic energy related penetration that accompanies metal deposition on organics. The intensities of C and Cu signal are mostly constant throughout the top CuPc layer, as expected for a film with low concentration of impurity. The slightly increase at the very top surface ($t \sim 0$) for all elements is due to the surface effect in SIMS [70].

There was a puzzle in organic semiconductors devices that there could be asymmetry in $I-V$ characteristics for interfaces of the same metal and organic material, but formed differently by either metal deposition on organic or organic on metal. The order of the deposition is one of the most important, yet easily overlooked, aspects in the interface formation. The major factors include the thermal energy of the material being evaporated, the topology of the substrate, the condensation energy on the surface, and the growth mode of the deposited film. For the process of organic deposited on metal (denoted as organic/metal), the diffusion/disruption between the two materials is low except the most reactive metals, since the thermal energy of the evaporated organic molecules is generally low due to the low evaporating temperature. The organic material normally arrives at the surface in the molecular form, and later condenses to form thin films. The condensation energy of the organic material on the surface is low due to the nature of van der Waals interaction that bonds the organic molecules. Comparing to organic on metal interfaces, there are significantly more diffusion and disruption at the metal on organic interfaces (deposit metal onto organic film), because the hot metal atoms have larger kinetic energies, which makes the penetration of metal atoms into the organic film fairly easy. Also, the metal arrives as isolated atoms or atom clusters that will give a high condensation energy, resulting in possible damage or reaction with the organic. The relative sizes of the organic molecule and metal atom are very different. The smaller metal atoms may easily fall into the “valleys” of the organic molecules. This fact requires one to excise caution when interpreting the energy level changes at the initial metallization process. It is therefore imperative to investigate and understand the symmetry of interface formation in the cases of metal deposited onto organic and organic deposited onto metal.

The changes in the UPS spectra caused by deposition of pentacene onto Au by Watkins et al. [170] are shown in Fig. 3.11(a). There is an initial shift of the vacuum level 0.8 eV closer to the Fermi level after the deposition of 2 Å of pentacene, reflected in the UPS cutoff shift. The shift of the vacuum level increases to a total of 1 eV after the deposition of 18 Å of pentacene. While these changes are observed in the cutoff position, no apparent change in position of any other feature within the UPS spectra is observed. A further decrease in the Au UPS features and a gradual increase in the pentacene UPS spectral features are observed as pentacene is deposited on the surface. Fig. 3.11(b) shows the evolution of the UPS spectra as gold is deposited onto a pentacene substrate. Upon deposition of 1 Å of Au the vacuum level and pentacene HOMO shifts ~0.5 eV to higher binding energy. The same shift is also observed in the XPS C 1s core level [309]. The rigid shift of these features are likely due to doping of the pentacene by Au that results in a movement of the Fermi level closer to the LUMO of the pentacene. Charging of the pentacene film can be ruled out from the constant XPS Au 4f core level [309]. After 8 Å of gold deposition there is a detectable Fermi level and the pentacene's HOMO features have been largely suppressed, indicating the interaction of gold with the pentacene surface. Yet even after 48 Å of gold the HOMO features that are associated with a metallic gold layer are still not apparent. This is further evidence that the gold has not yet formed a continuous layer, possibly forming clusters on the surface of the pentacene as suggested by the XPS results. The final surface has a work function of 4.2 eV instead of the 5.4 eV that would be expected

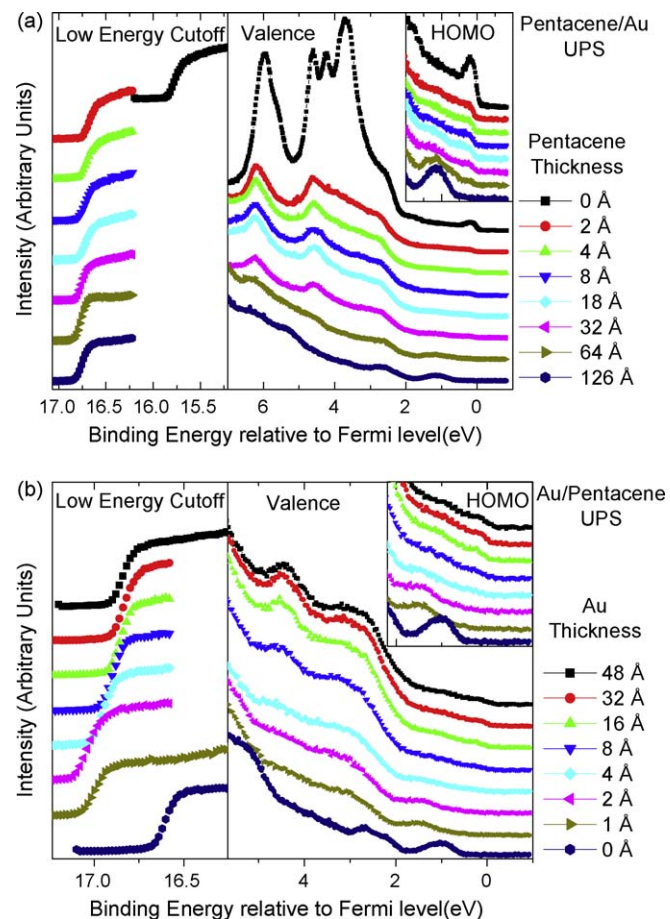


Fig. 3.11. (a) UPS spectrum evolution as a function of pentacene deposition thickness onto gold; (b) UPS spectrum evolution as a function of Au deposition thickness onto pentacene (from Ref. [170]).

for a continuous gold surface, suggesting that even though there is a metallic surface it is not a simple gold surface [170].

Fig. 3.12 presents a summary of the results for the interfaces between pentacene and metals Au, Ag, and Ca [170]. In the figure, the sequence of deposition is from the left to right. Both the Ag and the Au interface exhibit a measurable Fermi level after ~8 Å of metal deposition, indicating a metallic surface. Yet it can be clearly seen that neither metallic surface gives the work function of the pure metal, even after 30+ Å of metal deposition, nor the valence features of the clean metal surface. Au on pentacene results in a work function of 4.2 eV, about 1 eV lower than that of pure Au. Ag on pentacene gives a work function of 3.8 eV, 0.7 eV lower than that of pure Ag. It is interpreted as indication that as these metals are deposited onto the pentacene surface the metal either first penetrates the surface, thereby doping the upper layers of the pentacene, or diffuses into the pentacene. The attenuation of the C 1s XPS peak supports metal diffusion or clustering of Au and Ag. For the deposition rates used in these experiments, <0.1 Å per second, it is more likely that the metal has diffused into the pentacene. The subsequent doping region width, $w > 50$ Å, is estimated from XPS core level analysis. Au^* and Ag^* are used in Fig. 3.13 to represent the metallic mixtures at these interfaces. The difference between metal on organic and organic on metal results in asymmetric electronic properties, for example the hole injection barrier is 0.5 eV for pentacene on Au but 1 eV for Au on pentacene. Ca deposition on pentacene does not exhibit this behavior. With the deposition of 8 Å of Ca onto the pentacene the HOMO position relative to the Fermi level has shifted to where it was observed for the pentacene/Ca interface and the observed work function has

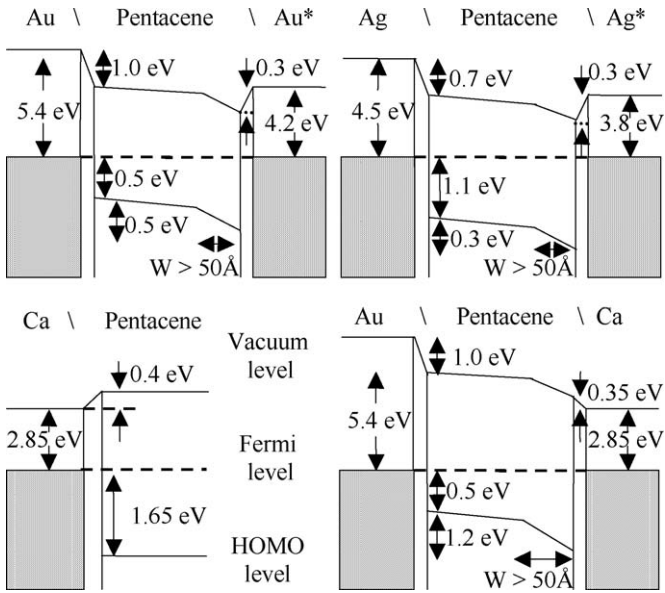


Fig. 3.12. Energy diagrams for the various interfaces between pentacene and different metals (Au, Ag, and Ca), with the sequence of deposition being from left to right (from Ref. [170]).

almost reached that of a clean Ca surface, which is achieved by 64 Å of Ca deposition. Unlike Au or Ag, Ca forms a pure metal film on the surface and exhibits symmetric behavior with regards to whether Ca is deposited onto pentacene or vice versa. This difference in behavior of Ca and noble metals is consistent with the observation that reactive metals penetrate much less than the noble ones when deposited on organic materials.

As noble metals are deposited to organic materials, the lack of chemical interaction of the metal atoms and the organic molecules can result in substantial clustering of the deposited metals [48,83,163,210,211,231,252,257,263,268,326–328]. Such effect is best studied with structure sensitive probes such as transmission electron microscopy (TEM), AFM, and X-ray diffraction (XRD). There can also be signatures of cluster formation in photoemission spectroscopy, most pronouncedly charging. Fig. 3.13 shows a cross-sectional TEM image by Durr et al. through the x-z plane of the Au/diindenoperylene (DIP)/Au heterostructure with 150 Å Au on 300 Å DIP with a lateral range of ~1 μm [263]. The image clearly shows the island-like morphology of the DIP film, with island heights of up to 1500 Å. The Au layer deposited on the DIP film covers the islands with a relatively sharp interface and consists of small coalesced clusters rather than of a smooth, closed film. In addition, interdiffusion of smaller Au clusters into the DIP islands is seen. However, the pronounced islanding morphology of DIP

makes it difficult to identify which Au clusters are embedded into individual DIP islands. Because of the relatively large probed sample thickness of ~100 nm along the y direction in Fig. 3.13, Au clusters simply covering the top of a small DIP island located in front of a taller DIP island may appear as clusters interdiffused into the taller DIP island. When examined with UPS, these Au clusters on top of the DIP film exhibit positive charging, since electron transfer from surrounding DIP to the clusters is difficult. The charging is observed to be neutralized by simultaneous light irradiation of the DIP sample [263].

3.4. Band bending in metal/organic semiconductor interface

In semiconductors, band bending is a fundamental issue that is important for electrical characteristics across the interface. The observation of band bending in a semiconductor depends on the depletion length, which can be very large if the semiconductor is not intentionally doped. Kelvin probe have been used to investigate the surface workfunction and band bending in organic semiconductors [86,88–91,94,192,210,329–342]. The energy of the vacuum level relative to the Fermi level of the substrate, ϵ_{vac}^F , of C₆₀ film on Au, Cu, Ag metals is shown in Fig. 3.14(a) as functions of the film thickness by Ishii et al. [94]. The data in small thickness region ($d \leq 10$ nm) is shown in the inset. An abrupt shift of the vacuum level was observed at $d \leq 1$ nm in Fig. 3.14(a). This is due to the formation of interfacial dipole layer. The value of ϵ_{vac}^F shows gradual downward shift, converging to 4.44 eV at $d = 500$ nm, reflecting band bending in C₆₀. Fig. 3.14(b) shows the change of ϵ_{vac}^F of N,N₀-bis(3-methylphenyl)-N,N₀-diphenyl-[1,10-biphenyl]-4,40-diamine (TPD)/metal (Au, Ag, Cu, Mg, Ca) as a function of the film thickness d . At $d < 1$ nm, an abrupt shift of ϵ_{vac}^F due to the formation of interfacial dipole layer is observed for all the substrates. After the completion of the shift, the plot becomes quite flat, indicating no thickness dependence, indicating flat band behavior. The observed flat band behavior is probably due to the high purity of the sample. Because of the very low concentration of the impurity, the space charge layer must be much wider, leading to the flat band behavior within 110 nm (see Eq. (1.3)). Another organic material with permanent dipole moment such as Alq, the surface workfunction behavior depends on whether the deposition is performed with light illumination. When illuminated, the thickness dependence of ϵ_{vac}^F is very similar to that of TPD, i.e., flat band with large d . When Alq film is deposited in dark condition, ϵ_{vac}^F of the film shows much different behavior from that under light irradiation. Fig. 3.14(c) plots ϵ_{vac}^F of Alq film deposited on Au and Al substrates in dark condition. In the initial stage of deposition up to $d = 1$ nm, ϵ_{vac}^F shows an abrupt downward shift due to the formation of interfacial dipole layer as in the case of “under light irradiation”. In the thicker region, ϵ_{vac}^F shows linear decrease over a wide range of thickness ($d = 5–550$ nm) with a mean slope of about ~0.05 V/nm. Even at $d < 500$ nm, no saturation of the change in ϵ_{vac}^F was observed. The underline mechanisms of such behavior are still being investigated [94].

3.5. Quenching of excitons

When an exciton is near a metal surface, the interaction with its image inside the metal causes energy transfer into the metal and quenching of the exciton. Chance et al. established a model where they described how molecular fluorescence was related to energy transfer rate [343]

$$k_{\text{ET}} = \beta d^{-3}, \quad (3.3)$$

where β is the energy transfer rate constant and d is the distance between the dipole emitter and the metal mirror. In addition to this established mechanism, my group observed that the quench-

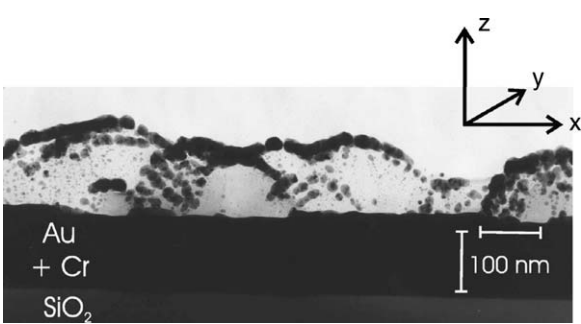


Fig. 3.13. Cross-sectional TEM image through the x-z plane of the Au/DIP/Au heterostructure. Interdiffusion of Au clusters into the DIP islands is seen (from Ref. [263]).

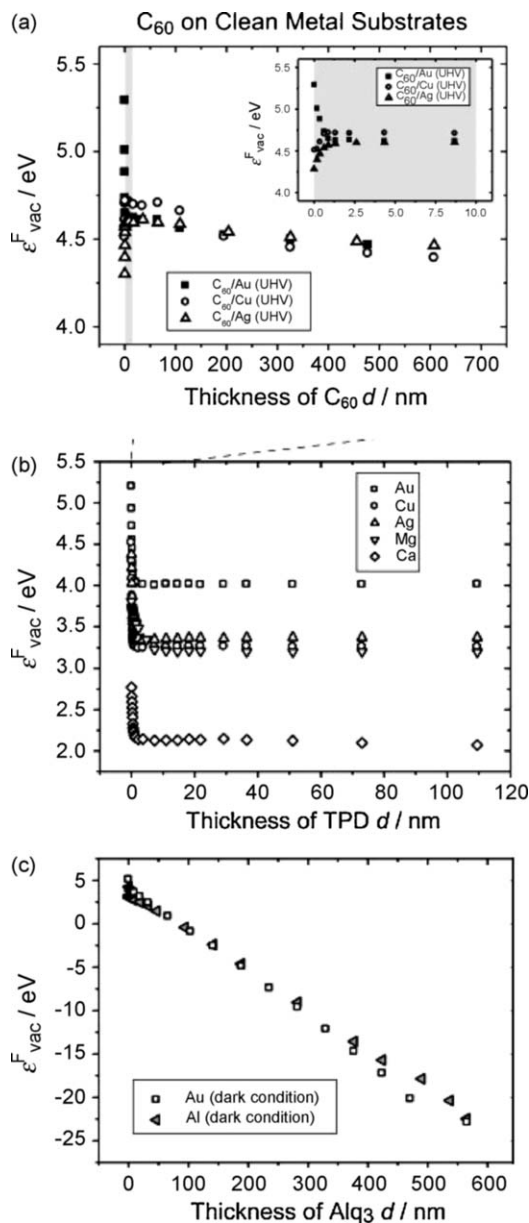


Fig. 3.14. Variation in vacuum level energy ϵ^F showing (a) band bending of C_{60} on Au, Cu, and Ag, (b) flat band of TPD on Au, Cu, Ag, Mg, and Ca, (c) linear decrease of Alq on Au and Al deposited in darkness (from Ref. [94]).

ing of excitons could occur way before a metal overlayer became metallic, as the metal atoms formed quenching centers to the luminescence of organic materials [303,344–351]. Shown in Fig. 3.15 is the photoluminescence (PL) intensity plotted as a function of Θ_{Ca} for a film of 300 Å 4PV, an oligomer of poly(phenylene vinylene) (PPV) [344]. The rate of intensity decrease can be divided into three stages. The first stage is between $\Theta_{\text{Ca}} = 0$ and 1 Å, the second between $\Theta_{\text{Ca}} = 1$ and 30 Å, and the third for $\Theta_{\text{Ca}} > 30$ Å. The first stage accounts for the reduction of the PL intensity by 65% and is due to the fact that the Ca atoms provide nonradiative decay channels. After the initial drop, the effect of PL quenching by Ca atoms is reduced, as indicated by a slower rate of PL quenching observed in the second stage, as the quenching region of additional Ca atoms overlap with existing ones. In the third stage, $\Theta_{\text{Ca}} > 30$ Å, the drop in PL intensity is solely to the attenuation of both excitation and emission photons due to the thickness of the Ca layer as it becomes metallic. The quenching phenomenon is quite common. It has the most sever adverse effect on single layer OLED

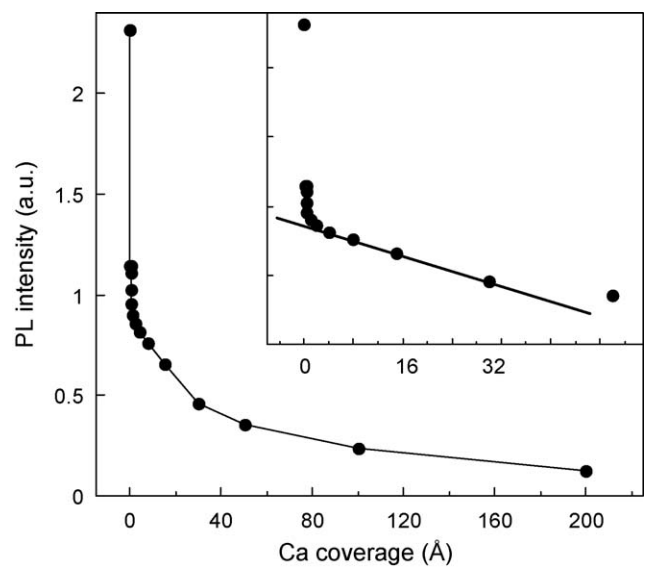


Fig. 3.15. PL intensity plotted as a function of Θ_{Ca} . The initial reduction is due to the fact that the Ca atoms provide nonradiative decay channels. (from Ref. [344]).

devices based on hole conducting materials, such as PPV and its derivatives, because of the radiative recombination zone in these devices is close to the metal cathode. For electron conducting materials, the problem will be much less significant since the recombination zone is close to the ITO anode, on which no quenching of PL is observed. It is also less important for multilayer devices with both electron conducting and hole conducting layers, since the emission zone will be localized at the organic/organic interface, provided that the electron conducting layer is substantially thicker than the combination of exciton diffusion length and cathode metal penetration depth [344].

Park et al. found that the PL quenching due to Ca deposition can be recovered after exposure to oxygen [303]. The crucial role of the oxidized Ca layer is clearer when the PL intensity evolution of Ca/4PV with and without the oxidation process are compared, as shown in Fig. 3.16. The bottom curve of Fig. 3.16(b) is the PL intensity as a function of Ca thickness without the oxidation process. Here a monotonic intensity decrease is evident. The middle curve is the PL intensity after each fresh deposition of Ca on previously oxidized Ca/4PV. For example, the data point at 8 Å is the PL intensity after 4 Å of fresh Ca was deposited on the 4 Å oxidized-Ca/4PV layer. The middle curve shows how effective a given Ca oxide layer is in protecting 4PV PL from fresh Ca. The top curve in Fig. 3.16(b) shows the PL intensity at the end of the oxidation process at a given Ca thickness. The PL intensity of oxidized Ca/4PV remains between 55 and 65% of that of pristine 4PV up to 50 Å of oxidized Ca layer. On the other hand, the PL from unoxidized Ca decreases down to around 15% after deposition of 50 Å Ca. These numbers suggest that a proper oxidation of Ca at the Ca/4PV interface could significantly improve the efficiency of a single layer EL device [303].

3.6. Contaminated surface

During device fabrication, it is possible that surface can be contaminated, and the interface structure may be different from that obtained with surface analytical tools under UHV conditions. It is especially true for polymer devices, where typical way of depositing thin films by spin cast usually expose the surface to ambient atmosphere. Some surface analytical work has been performed to investigate the effect of the surface contamination that often exists during device fabrication [87,134,141,223,248,

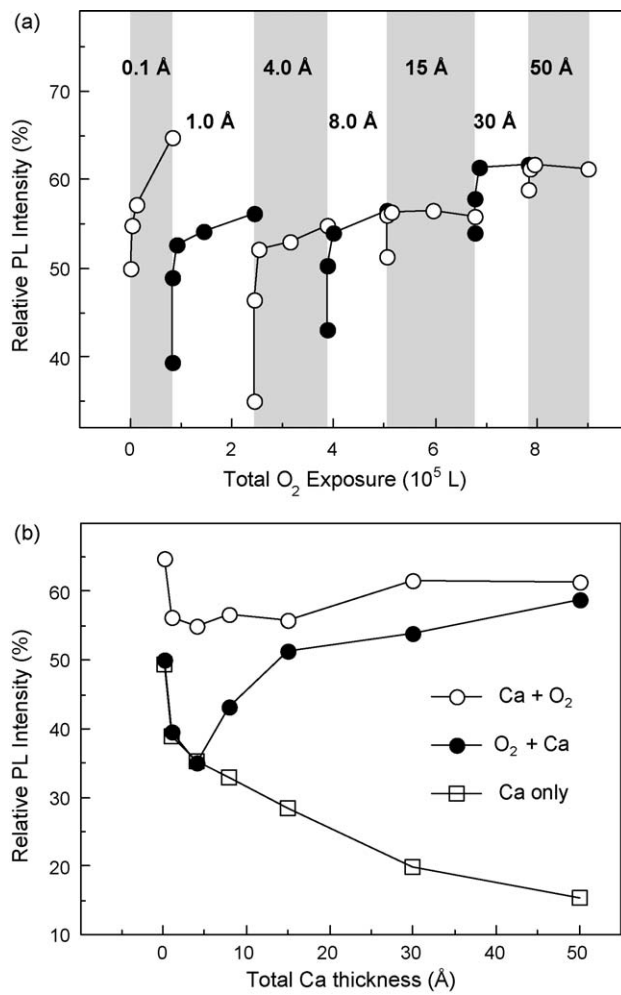


Fig. 3.16. PL intensity evolution of Ca/4PV with and without the oxidation process. PL quenching due to Ca deposition can be recovered after exposure to oxygen. (from Ref. [303]).

270,302,311,318,350,352–370]. For spin cast polymer films, my group and others observed that the surface contamination species such as oxygen and water can cause chemical reaction with the deposited metal atoms, forming oxide and postpone the interaction and formation of the interface between the metal and the organic material [298,303,311,313,314,317,318,325,359–364,366, 367,371,372]. An example is XPS study of the Ca/PPV interface, which shows the initial formation of Ca oxide and the lack of strong reaction between the Ca overlayer with the PPV substrate, indicating that the Schottky barrier formation in Ca/PPV was a slow process. The late barrier formation at the Ca/PPV interface can be attributed to the shielding by surface oxygen impurities, part of which underwent calcium oxide formation at the interface. Similar processes may also occur in small molecule devices if the surface is inadvertently or deliberately exposed to ambient. Wan et al. addressed the effects of ambient exposure of a polycrystalline Au electrode prior to making contact with α -N,N?-di-1-naphthyl-N,N?-diphenyl-1,1?-biphenyl-4,4?-diamine (α -NPD) [141]. UPS and current–voltage (I – V) measurements are used to investigate the resulting hole barrier and charge injection characteristics. UPS measurements show that the hole barrier with the contaminated low work function Au electrode is reduced by 0.4–0.6 eV with respect to the barrier with the clean high work function Au electrode. The corresponding interface dipoles are 0.3 eV for the former and 1.3 eV for the latter. I – V measurements confirm this unexpected change in barrier. These results illustrate the role of

the contamination layer in reducing the direct interaction between metal and molecules [141].

4. Organic/organic interface

The energy offset between two dissimilar organic films is vitally important to efficient OLED and OPV operation. The interfaces between organic molecules share some common features with the metal/organic interfaces, as well as having some of their own characteristics. The interface dipole in organic–organic interface is much less common as in metal–organic interface, given the fact that there are less itinerant charge carriers in the former than the latter and the contributions of charge transfer and electron cloud tail insignificant. The main contributions to the interface dipole are most likely from the alignment of the permanent dipole of the organic molecule or band bending in the accumulation region. Furthermore, to date researchers have not observed in organic–organic interfaces significant chemical interactions or strong interdiffusion. This can be attributed to the fact that the wave functions for the molecules do not extend much beyond a few nearest neighbors, and the molecules are relatively large. However, many other features are observed, depending on the system under investigation [37,80, 101,104,123,128,140,142,150,158,164,166,176,208,217,324,373–377]. Interface dipoles have been observed by Hamima et al. for tetracyanoquinodimethane (TCNQ) on tetrathianaphthacene (TTN), from vacuum levels shifts [375]. Similarly, studies of PTCDA on phthalocyanines, (InCl and Zn, ClInPc, and ZnPc, respectively) have demonstrated by Deshpande et al. vacuum level shifts attributed to dipole formations at the interfaces. In addition, UPS by Schlaf et al. results in combination with XPS measurements reveal that band bending occurs at the PTCDA/Pc interfaces [376]. Conversely, Hill and co-workers show that other donor–acceptor type molecular solid interfaces do not form appreciable interface dipoles [377]. Tang et al. demonstrated the interface band bending depended on the substrate beneath the organic heterojunction [323]. Gao et al. showed that band bending of organic heterojunction could be induced by carrier accumulation, which might in turn result in carrier mobility enhancement in the interface region [324].

4.1. Organic/organic interface energy level alignment

The UPS spectra of N,N?-bis-(1-naphthyl)-N,N?-diphenyl-1,1?-biphenyl-4,4?-diamine (NPB)/Alq by Forsythe et al. are shown in Fig. 4.1(a) [374]. The symbols A and B mark features unique to Alq and NPB, respectively. Their shifts as the thickness Θ_{NPB} increases again indicate the interface energy level bending at the interface. More detailed information can be obtained by spectrum subtraction. As shown in Fig. 4.1(b), the NPB contribution in the spectrum of $\Theta_{NPB} = 5 \text{ \AA}$ is isolated by first scaling the Alq spectrum ($\Theta_{NPB} = 0 \text{ \AA}$) to the ratio of the A feature in the two spectra, followed by aligning the features and subtracting the scaled spectra. The resulting difference spectrum is nearly identical to that of NPB of $\Theta_{NPB} = 55 \text{ \AA}$ except a rigid shift to the lower BE. Such spectrum subtraction allows one to distinguish the highest occupied molecular orbital (HOMO) of NPB, which increases from -1.0 eV to -1.4 eV as a function of increasing Θ_{NPB} . The HOMO is defined as the intersection of the leading edge and the baseline of the spectrum as shown in Fig. 4.1(b). A similar procedure was also conducted for the Alq contribution UPS spectrum with $\Theta_{NPB} = 2 \text{ \AA}$. The resulting Alq UPS spectrum is identical to ($\Theta_{NPB} = 0 \text{ \AA}$) and a HOMO level increase of 0.1 eV to higher binding energy after the first NPB coverage. For $\Theta_{NPB} \geq 5 \text{ \AA}$, the Alq contribution to the UPS spectrum could not be isolated from the NPB contribution. These gradual shifts of occupied molecular orbital features provide a clear picture of energy level bending in both NPB and Alq. Another remarkable feature is the lack of interface states, indicating little

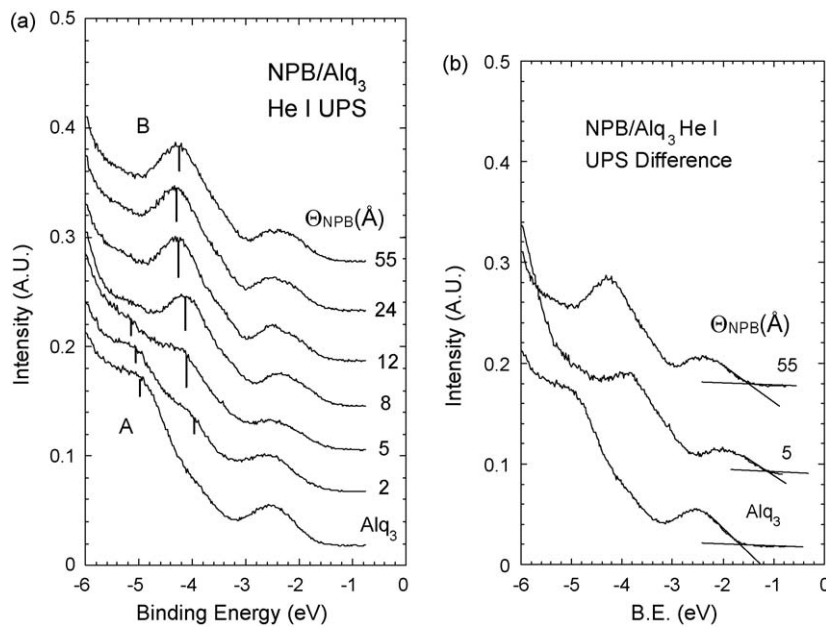


Fig. 4.1. (a) Ultra-violet photoemission spectroscopy of NPB/Alq films as a function of NPB coverage Θ_{NPB} . The symbols A and B mark features unique to Alq and NPB, respectively. (b) The NPB contribution is isolated by spectral subtraction (from Ref. [374]).

wavefunction overlap or charge transfer between the two organic semiconductors.

The schematics of the interface energy diagram of NPB/Alq is given in Fig. 4.2 [374]. Taking an optical band gap of 2.8 eV and 3.1 eV for Alq and NPB respectively, the LUMO energy level position for Alq is 0.8 eV below the NPB LUMO, while the HOMO levels for Alq and NPB are offset in the bulk by 0.3 eV. In addition to the bulk level offsets, the peculiar downward energy level shift of Alq and upward shift of NPB toward the interface enhance the HOMO discontinuity from the bulk value of 0.3 eV to 0.7 eV. For Alq, the band bending region is determined from the shift in the core levels as determined from XPS, which is approximately 0.4 eV. The UPS difference spectra cannot distinguish Alq contributions beyond the first NPB coverage. This additional energy level bending at the interface may contribute traps and additional

barriers for the carrier transport across the interface. From the LUMO level alignment, a substantial barrier exists for electrons to be injected from the Alq side of the heterostructure to the NPB with a relatively smaller barrier for holes to tunnel into the Alq. This energy level alignment favors electron confinement in the emissive Alq layer of the heterostructure.

A summary of the alignment of organic levels at twelve organic/organic heterointerfaces by Kahn and his coworkers is presented in Fig. 4.3 [104]. It is found that the vacuum levels align at almost all organic/organic heterointerfaces within the experimental uncertainty of 0.1 eV. This is not too surprising, considering the closed-shell nature of the molecules that comprise both constituents of the heterointerface. Charge exchange and/or chemical bonding between different molecular species is not expected. Perhaps the most interesting cases are those where measurable dipoles do exist: CuPc/PTCDA (0.4 eV), PTCDA/Alq (0.5 eV), α -NPD/Alq (-0.25 eV), and 2,9-dimethyl-4,7-diphenyl-1,10-phenanthroline (BCP) on bathocuproin3,4,9,10 perylene-tetracarboxylic bisbenzimidazole (PTCBI, 0.4 eV) where the dipole derived vacuum level shift is defined as positive when the vacuum level of the second material is at a higher energy than the first. It can be noted that three of the constituents of the interfaces possessing dipoles also exhibit a limited range of Fermi level movement at heterointerfaces (PTCDA, PTCBI, BCP). It is therefore possible that the Fermi levels of these materials are pinned by impurity related gap states, and the dipoles are the result of (de) populating a high density of impurity states near the interfaces. The 0.5 eV dipole observed at the PTCD/Alq interface cannot be explained on this basis, given the above observation that the Fermi level is completely free to move within the Alq gap. Considering the mechanisms suggested above, and the counter examples, one must conclude that neither of the suggested mechanisms for dipole formation at organic/organic heterointerfaces is sufficient to explain all of the observed behavior [104]. It is also suggested that the concept of alignment of charge neutrality levels (CNL), originally derived from metal-organic interactions, can be used to explain and predict interface dipole and molecular level offset at organic/organic heterojunctions [142].

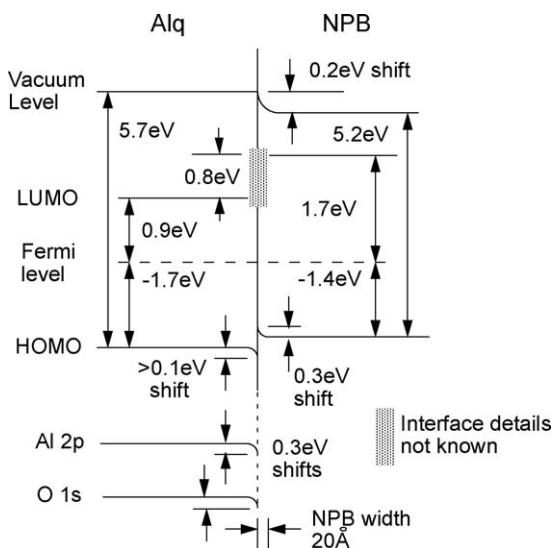


Fig. 4.2. Energy diagram with the HOMO and work function position from the UPS and core level positions from XPS (from Ref. [374]).

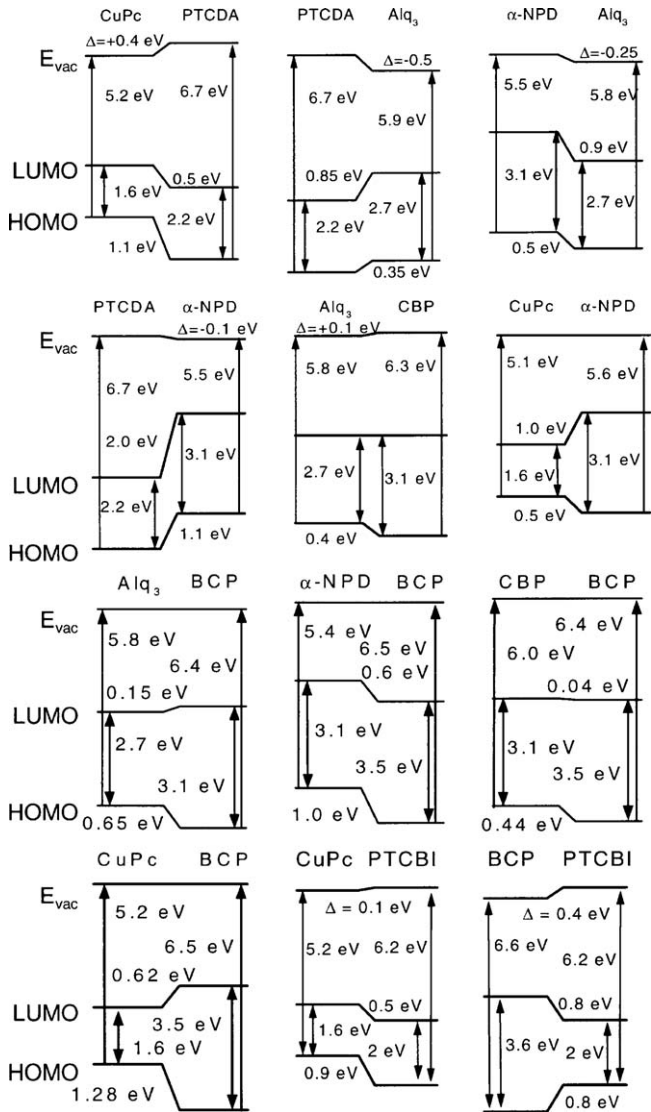


Fig. 4.3. The alignment of molecular levels at 12 organic/organic heterointerfaces. Most vacuum levels align within the experimental uncertainty of 0.1 eV.(from Ref. [104]).

4.2. Band bending and carrier accumulation at organic/organic interface

Further investigations on the energy level alignment of organic/organic interface reveals that the energy level alignment may depend on the substrate and the formation of a space charge layer may result in substantial band bending. The energy diagrams of the CuPc/Alq heterojunction on indium-tin-oxide (ITO) and Mg substrates obtained with UPS and XPS by Tang et al. are depicted in Fig. 4.4 [323]. The Fermi levels in the two materials are aligned in a thermodynamic equilibrium state. In the schematic energy diagram, the LUMO edge E_{LUMO} is derived via the charge transport gaps of 4.2 and 1.7 eV for Alq and CuPc, respectively. ITO and Mg substrates shift the E_F position in Alq film from 1.5 to 3.2 eV above the HOMO edge. The energy level lineup at the CuPc/Alq interface on ITO is consistent with the traditional concept of vacuum level alignment. However, the same heterojunction formed on the Mg substrate shows remarkably different electronic structures. The HOMO offset in the bulk of the two organics on the Mg substrate is estimated to be 1.7 eV, which is different from the value of 0.9 eV in the same junction formed on ITO. As shown in Fig. 4.4(b), the built-in potential

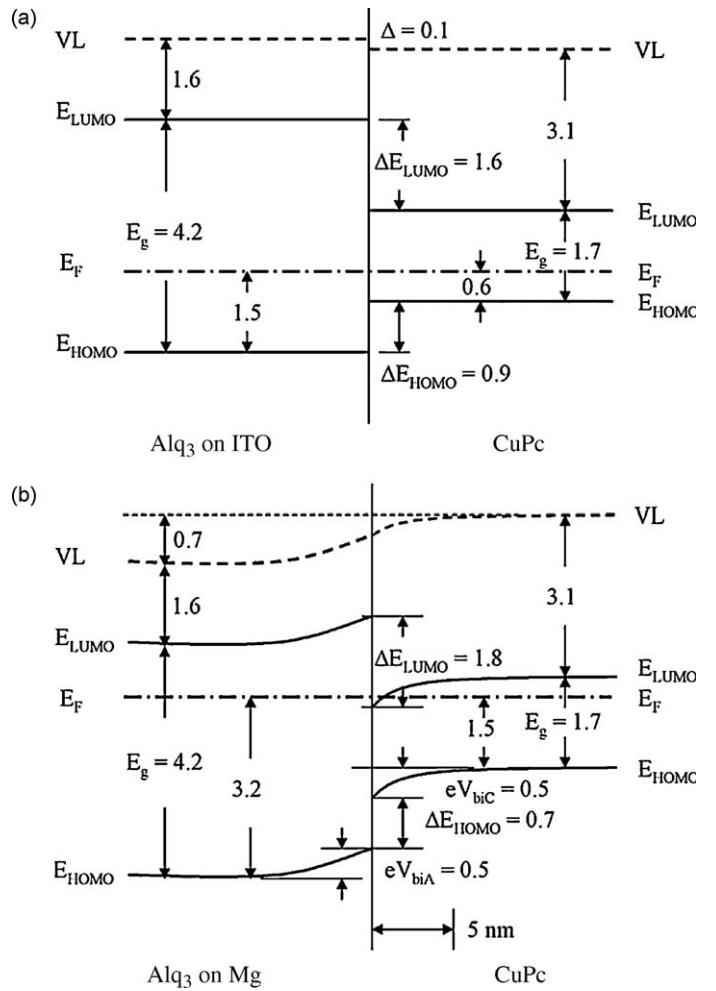


Fig. 4.4. Schematic energy level diagrams of the CuPc/Alq junction on (a) ITO and (b) Mg substrates, showing the energy level alignment and band bending dependence on the substrate. (from Ref. [323]).

barriers in Alq and CuPc (eV_{biA} and eV_{biC}) represent the energy level bending in the space charge regions. Taking into account the total energy level bending, the HOMO offset directly at the interface E_{HOMO} for CuPc/Alq on Mg is, however, reduced to 0.7 eV, while the LUMO offset E_{LUMO} is increased to 1.8 eV. Before the formation of the CuPc/Alq heterojunction, the EA of CuPc is larger than that of the work function of Alq when Mg is used as the substrate (see Fig. 4.4(b)). In order to achieve thermal equilibrium with Fermi level alignment, charge carriers will spontaneously flow across the interface, giving rise to the formation of an accumulation layer of electrons in CuPc and a depletion layer in Alq adjacent to the interface. The space charges are stored in states generated by the extension of occupied and unoccupied orbitals in the energy gap. Therefore, built-in potential barriers are formed on both sides of the heterojunction. Since the LUMO of CuPc for the CuPc/Alq junction on Mg is close to the Fermi level, we expect a large number of energy states for electrons and thus a narrow space charge width ($\sim 50 \text{ \AA}$) in the CuPc layer. On the contrary, when ITO is used as the substrate, the above conditions are not satisfied and thus the vacuum level alignment occurs (Fig. 4.4(a)). The results observed here indicate that the energy level alignment at organic heterojunction is affected by the E_F position in the energy gap, and the applicability of the traditional concept of vacuum level alignment at an organic heterojunction is limited to some specific conditions [323].

Carrier accumulation at the organic heterojunction can have profound effects on the transport properties. A device configura-

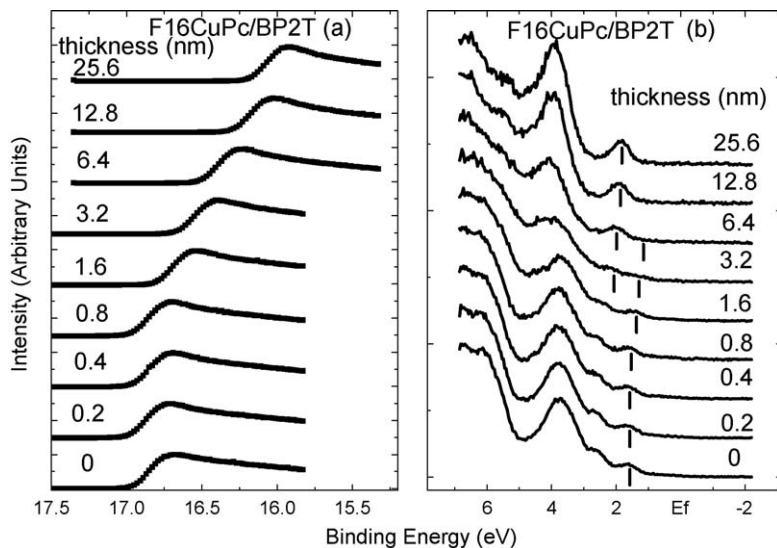


Fig. 4.5. Evolution of the cutoff (a) and the HOMO region (b) of the UPS spectra as $F_{16}\text{CuPc}$ is deposited on BP2T. The HOMO peaks of $F_{16}\text{CuPc}$ and of BP2T are marked (from Ref. [324]).

tion based on organic heterojunction of 2,5-bis(4-biphenyl)l bithiophene (BP2T) and copper-hexadecafluoro-phthalocyanine ($F_{16}\text{CuPc}$) by Shi et al. exhibited three different operating modes, governed by Θ_B , the thickness of the BP2T film [378]. For BP2T film thicknesses below 2 nm, the devices exhibited n-channel unipolar transport characteristics. The electron mobility increased with increasing BP2T film thickness, reached a maximum at $\Theta_B \sim 5$ nm, and then diminished exponentially. The hole mobility increased and reached a maximum at $\Theta_B = 6$ nm, and then reduced slightly to a saturation value. It is remarkable that at the maxima, the hole and electron mobility are improved by 3 and 12 folds from the bulk values, respectively [378].

In Fig. 4.5, the UPS spectra of the cutoff region (a) and the valence region (b) are shown as $F_{16}\text{CuPc}$ is deposited on to a 20 nm BP2T film by Gao et al. [324]. The highest occupied molecular orbital (HOMO) peak positions are marked by short bars. It can be seen that at low $F_{16}\text{CuPc}$ coverages ($\Theta_F \leq 0.8$ nm), there is hardly any change in the spectrum, indicating negligible interface reaction and dipole formation. Spectral changes start to be apparent for higher $F_{16}\text{CuPc}$ coverages. Most significantly, the HOMO peak positions of both $F_{16}\text{CuPc}$ and BP2T can be seen to shift to lower binding energy as Θ_F increases, which clearly demonstrates band bending in the heterojunction in both materials. The BP2T HOMO can be observed up to $\Theta_F = 3.2$ nm, above which it is hardly visible because of the attenuation by the $F_{16}\text{CuPc}$ overlayer. The shift of the BP2T HOMO is measured to be 0.36 eV at this stage. At the same stage, the overlayer $F_{16}\text{CuPc}$ features become discernible, and dominate for higher $F_{16}\text{CuPc}$ coverages. The total shift of the $F_{16}\text{CuPc}$ HOMO can be deduced to be 0.30 eV. At the final coverage $\Theta_F = 25.6$ nm, the valence spectrum becomes completely that of $F_{16}\text{CuPc}$, and similar to that of CuPc with a rigid shift of 0.6 eV to higher BE.¹⁴ The cutoff shift shown in Fig. 4.7(a), which reflects the vacuum level change of the surface, gives a trend very close to that in the valence region, and the total shift of 0.78 eV is slightly larger than the sum of the observed band bending in BP2T and $F_{16}\text{CuPc}$. The small difference occurs mainly as the $F_{16}\text{CuPc}$ HOMO peak position is saturated, and is therefore likely due to a change in the morphology at the surface that in turn modifies the ionization potential of the $F_{16}\text{CuPc}$.

The data presented in Fig. 4.5 clearly demonstrated that in the $F_{16}\text{CuPc}/\text{BP2T}$ heterojunction formed by $F_{16}\text{CuPc}$ deposition on BP2T is characterized by no interface dipole and reaction, and by band bending in both materials. Given that the $F_{16}\text{CuPc}$ shift is mostly saturated at $\Theta_F = 12.8$ nm, it can be deduced that the Debye

length, an important parameter that characterizes the distance over which an electric field can be effectively screened by the semiconductor, is about 3 nm in $F_{16}\text{CuPc}$. To learn the band bending region and obtain the Debye length in BP2T, we reversed the deposition order, and measured the interface electronic structure as BP2T is deposited onto a 20 nm $F_{16}\text{CuPc}$ film. The measured UPS spectra of the cutoff and the valence region from the BP2T/ $F_{16}\text{CuPc}$ heterojunction are shown in Fig. 4.6(a) and (b), respectively, and the HOMO peak positions are marked [324]. At initial BP2T coverages ($\Theta_B \leq 1.6$ nm), the UPS spectra of BP2T/ $F_{16}\text{CuPc}$ show little change, which is similar to $F_{16}\text{CuPc}/\text{BP2T}$ and confirms that between the two materials there is neither interface reaction nor dipole formation. Interestingly, as the BP2T coverage increases from $\Theta_B = 1.6$ nm, the vacuum level starts to move, while the HOMO peak of $F_{16}\text{CuPc}$ remains stationary as long as it can still be distinguished at $\Theta_B = 6.4$ nm. In contrast, the HOMO peak of BP2T, first discernable at $\Theta_B = 3.2$ nm, continuously shifts to the lower BE till its saturation at about 0.83 eV below the Fermi level at $\Theta_B = 25.6$ nm. The shift of BP2T HOMO in the BP2T/ $F_{16}\text{CuPc}$ interface is consistent to that in the $F_{16}\text{CuPc}/\text{BP2T}$ interface, i.e. bending upward from the bulk BP2T to the interface. The total band bending of BP2T, as judged by the vacuum level and HOMO peak shift, is 0.33 eV, which is quite consistent to the BP2T portion in the $F_{16}\text{CuPc}/\text{BP2T}$ interface. The band bending region in BP2T is about 15 nm, indicating that the Debye length in BP2T is similar to that in $F_{16}\text{CuPc}$.

It can be seen that for $F_{16}\text{CuPc}$ on BP2T, there is band bending in both materials, resulting in hole accumulation in the BP2T side and electron accumulation in the $F_{16}\text{CuPc}$ side. For BP2T on $F_{16}\text{CuPc}$, the band bending only occurs in BP2T. The dissimilarity between the two interfaces can be understood from the fact that the replacement of H in CuPc by F substantially increases the ionization potential and pins the Fermi level of bulk $F_{16}\text{CuPc}$ at the edge of the LUMO. As a result of the Fermi level pinning, the energy levels in $F_{16}\text{CuPc}$ remains stationary as BP2T is deposited onto it. Such pinning does not occur for the initial depositions of $F_{16}\text{CuPc}$ on BP2T, since the vacuum level has to be aligned and the amount of $F_{16}\text{CuPc}$ is small. The schematics of the interface electronic structure of $F_{16}\text{CuPc}/\text{BP2T}$ and BP2T/ $F_{16}\text{CuPc}$ are shown in Fig. 4.7 [324]. In the figure, the sequence of deposition is from the left to right. The vacuum level is determined from the maximum of the cutoff derivative. The HOMO and LUMO positions are obtained from the linear extrapolation of the leading edge of

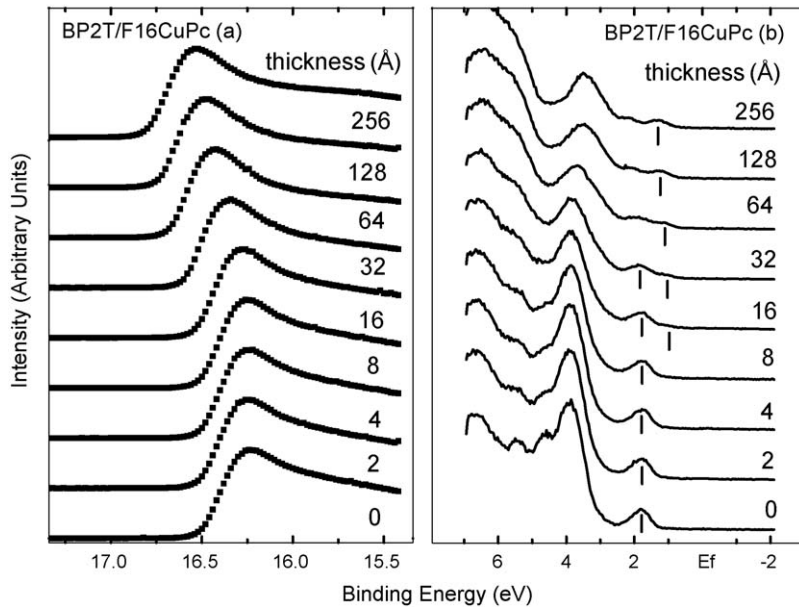


Fig. 4.6. Evolution of the cutoff (a) and the HOMO region (b) of the UPS spectra as BP2T is deposited on F16CuPc. The HOMO peaks of F₁₆CuPc and of BP2T are marked (from Ref. [324]).

UPS and IPES. The most remarkable feature of the F₁₆CuPc/BP2T heterojunction, as shown in Fig. 4.7(a), is that the band bending occurs in both materials, 0.36 eV and 0.30 eV in BP2T and F₁₆CuPc, respectively. Incorporating the band bending, the discontinuity of the HOMO levels at the interface can be deduced to be 1.03 eV. There is also an interface dipole potential of 0.95 eV between BP2T and the Au substrate. For BP2T/F₁₆CuPc (Fig. 4.7(b)), the band bending of 0.33 eV is mainly confined in BP2T, as the Fermi level in bulk F₁₆CuPc is pinned near the edge of its LUMO. The interface dipole between F₁₆CuPc and the Au substrate is measured to be 0.50 eV. The ionization potential for F₁₆CuPc in the two interfaces has some variations, possibly due to the difference in the molecular orientation and alignment.

The Debye length of BP2T and F₁₆CuPc in the interface region can be deduced from the observed band bending, if the latter can be attributed completely to the screening effect of the accumulated charge carriers. The Debye length thus deduced is conventionally referred to as extrinsic, in contrast to the intrinsic one that is from the ionized dopants in the depletion region (see discussions of Fig. 1.4). Here it should be emphasize that large accumulative shift in inorganic semiconductor heterojunctions is rare because the Fermi

level is close to the band edges as there is little defect states tailing into the band gap. For n- or p-type organic semiconductors, the Fermi level can be 0.5 eV or more from the band edges, and the band bending in the accumulation region can be substantial. In the cases of BP2T and F₁₆CuPc, it reaches several tenths of an eV as observed with UPS and shown in Figs. 4.5 and 4.6. The fitting of the band bending by Debye exponential decay is shown in Fig. 4.8. It can be deduced that the Debye lengths in F₁₆CuPc and BP2T are 4.8 nm and 6.4 nm, respectively. The observation of band bending in both BP2T and F₁₆CuPc for F₁₆CuPc/BP2T may offer an interesting explanation to the mobility dependence on the BP2T thickness described in Ref. [378]. The band bending in the heterojunction creates a higher electron (hole) density in F₁₆CuPc (BP2T), filling in shallow traps and resulting in increased electron and hole mobility in the interface region. As the BP2T thickness grows, both the electron and hole mobility increase and reach maximum values above those of the pristine materials. As the BP2T thickness further increases, it screens off the electric field, and the contribution to the mobility by the heterojunction gradually fades away. The same screening effect should also reduce exponentially the apparent n-mobility from F₁₆CuPc as the BP2T thickness increases.

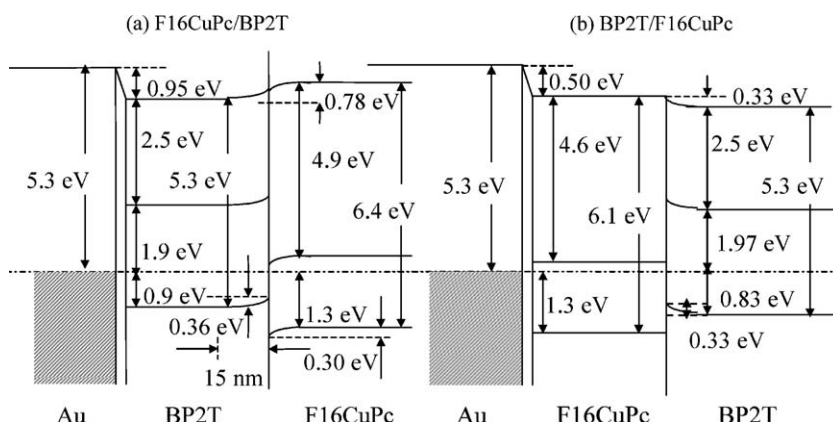


Fig. 4.7. Schematic energy level diagrams of (a) F₁₆CuPc on BP2T and (b) BP2T on F₁₆CuPc (from Ref. [324]).

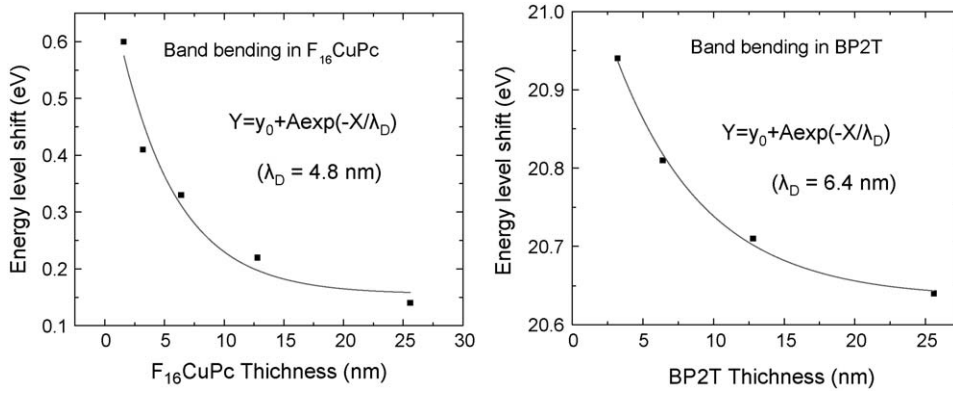


Fig. 4.8. Fitting of the band bending data and deduction of the Debye lengths in F₁₆CuPc and BP2T.

4.3. Interface charge separation and transfer

The charge transfer processes in molecular films can roughly be divided into two classes depending on the nature of the molecular levels involved in the reaction. The first class consists of the charge transfer between the HOMO of the donor and the acceptor and will be referred as HOMO–HOMO transfer in this chapter. The second class includes the transfer reactions between the excited state manifolds or the LUMO of the donor and the acceptor centers and will be referred as LUMO–LUMO transfer. Interestingly, the same molecular species of a particular heterostructure can display both types of CT depending on the nature of the excited states and the excitation energies involved. In the following, we shall focus on the LUMO–LUMO type of electron transfer, although the organic heterostructure studied shows both types of CT.

In the case of LUMO–LUMO transfer, these key factors are the energy level alignment between the LUMO levels of the acceptor and the donor and the strength of the electronic coupling between the excited state manifolds. The first factor is critical in determining whether the reaction is energetically feasible, i.e. whether a barrierless CT can be realized. The second factor determines the overall rate and the efficiency of the reaction, and it is subject not only to the photochemistry of the donor and the acceptor but also to the film and interface properties, e.g. morphology, orientation effects, etc. For a barrierless transition these factors can be incorporated in a simple rate equation [379]:

$$k_{ET} = \frac{2\pi}{\hbar} V^2 \rho. \quad (4.1)$$

Eq. (4.1) defines the effective rate as the product of the electronic coupling V^2 between the two vibrational manifolds and the combined density of states ρ of the donor–acceptor complex. These kinds of barrierless CT reactions in solid systems have been found to be extremely rapid, ranging from a few tens of femtoseconds to a picosecond, with the fast transfer rate being an important manifestation of the high CT efficiencies achievable in molecular systems.

Presented below are the results of time-resolved 2-photon photoemission spectroscopy (TR-2PPE) on an organic heterostructure of N,N'-diphenethyl-3,4,9,10-perylenetetracarboxylic diimide (DPEP) and TPD by Makinen et al. [380,381]. DPEP is an organic photoconductor material, and it is well known for its charge generator properties, and TPD is a widely used organic hole transport material in many photoreceptor applications. Together these two materials form a photoreceptor structure where either of the molecules can act as a donor depending on the excitation energy. In conjunction with the TRPES measurements of the bilayer structures, we measured the UPS spectra on the films after each

TPD evaporation. The progression of the UPS spectra of a TPD/DPEP film is shown in Fig. 4.9 as a function of the kinetic energy observed in the energy analyzer [380,381]. The effect of the added TPD layer can be observed as a shift of the HOMO level starting at 4 Å coverages. The HOMO of the pristine DPEP film is at 29.45 eV whereas at 24 Å the level has shifted to 29.60 eV. At the same time, the vacuum level cut-off of the film with 24 Å TPD is shifted down from the pristine value of 13.85 eV to 13.70 eV. This means that the spectral width of the bilayer film is 0.3 eV wider than the value for the pristine DPEP film. Consequently, the ionization potential of the bilayer film is 5.3 eV, which is 0.3 eV lower than the ionization potential of the pristine film, 5.6 eV. Furthermore, the shift of the vacuum levels in the bilayer films indicates the presence of vacuum level offset between the two constituent films. The observed vacuum level shift of 0.15 eV can be considered small, and it compares well with shifts reported for other organic–organic interfaces. The HOMO level of the TPD/DPEP structure is 0.15 eV higher in energy than the DPEP HOMO level. This will affect the kinetic energy spectrum measured in the TR-2PPE. Fig. 4.9 also includes a UPS spectrum of a pure TPD film. The ionization potential of the 400 Å film was found to be 5.2 eV, which compares relatively well with the value of 5.3 eV for the bilayer structure. There are obvious similarities between the pristine TPD spectrum and the high TPD coverage bilayer spectra. It turns out that the bilayer spectra can mostly be described as a superposition of the pristine DPEP and TPD spectra, which implies that at least energetically the composite layers preserve their own characteristics.

As the TPD coverage on the DPEP films was increased, the TRPES spectra showed longer overall decay times, i.e., the delay spectra appeared broader. It was found that a single exponential function convolved with the instrument response function did not properly describe the time delay spectrum of the composite films any more, and it becomes necessary to include two exponential decay terms:

$$I(t) = R(t) \otimes \left[A_1 \exp\left(\frac{-|t|}{\tau_1}\right) + A_2 \exp\left(\frac{-|t|}{\tau_2}\right) \right], \quad (4.2)$$

where the amplitudes A_1 and A_2 were allowed to vary during the fitting process. Interestingly, the two lifetime components included in the fits are separated by more than an order of magnitude at high TPD coverages, as can be seen in Fig. 4.10, where the deconvoluted lifetimes are plotted as a function of energy above the DPEP HOMO level. The fast components range from 40 to 80 fs, and the long components are from 200 to 800 fs in the TPD/DPEP film. The short components in bilayers are also consistently longer than the corresponding single exponential lifetimes in pristine DPEP films.

The lifetime vs. energy plots reveal another remarkable effect of the added TPD layer. The energy-dependence of the lifetimes is

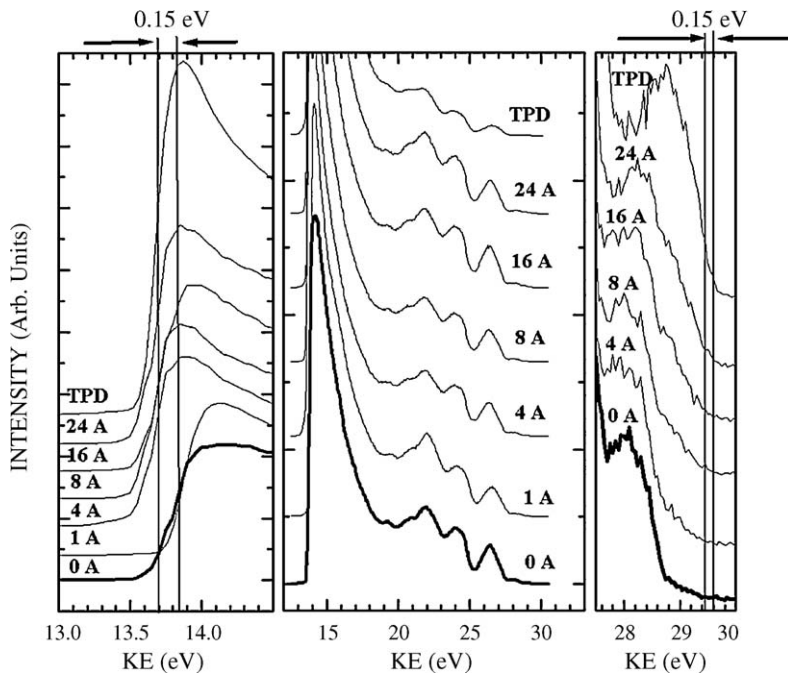


Fig. 4.9. UPS spectra of DPEP film with increasing TPD coverage. The effect of the added TPD layer can be observed as a shift of the HOMO level. (from Ref. [380]).

different in bilayers when compared with the trend found in pristine DPEP films where lifetimes decrease monotonically with increasing energy. In bilayers, the short components seem to be almost energy-independent up to 3.0 eV above the DPEP HOMO. Above 3.0 eV, however, the short components increase with

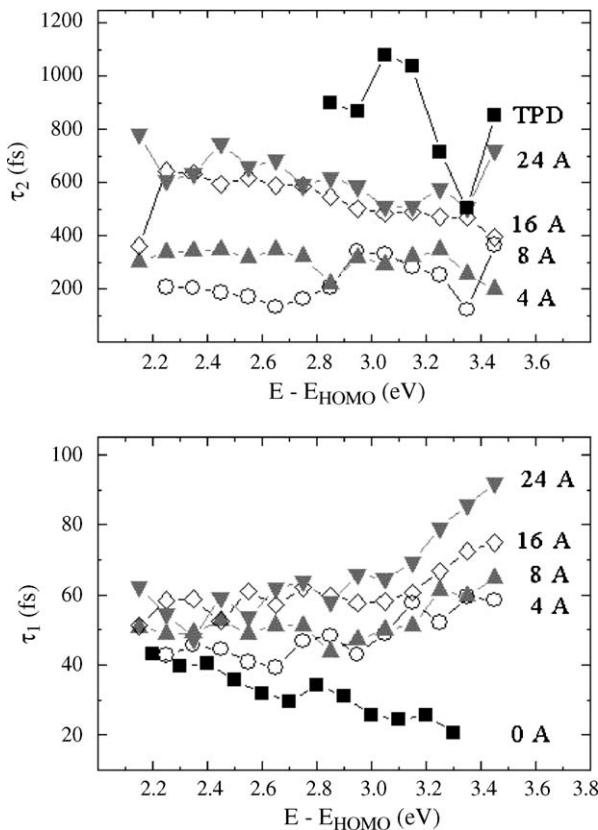


Fig. 4.10. Slow and fast lifetime components in TPD/DPEP-I films as a function of energy. The fast component depends on the energy, whereas the slow one does not (from Ref. [381]).

increasing energy, which is the opposite to what was observed in pristine DPEP films [315]. The most dramatic change observed, as the thickness of the TPD layer is increased, is the sudden growth in the absolute signal intensity. The appearance of two exponential components in the bilayer decay dynamics indicates the presence of two distinct electron populations with different decay mechanisms. It is clear from the pronounced dependence of the lifetime components on the TPD deposition thickness that the decay dynamics observed in TRPES experiments is interface and adlayer driven. Therefore, the first step in understanding the observed decay dynamics is to identify the possible electron populations formed in the bilayer structure upon photoexcitation. The measured intensity for the fast component at energy above HOMO of DPEP, $E - E_{\text{HOMO}} = 2.55 \text{ eV}$, is shown in Fig. 4.11. It can be seen that the intensity increases dramatically as the TPD overlayer thickness increases. Given the fact that the energy is below the

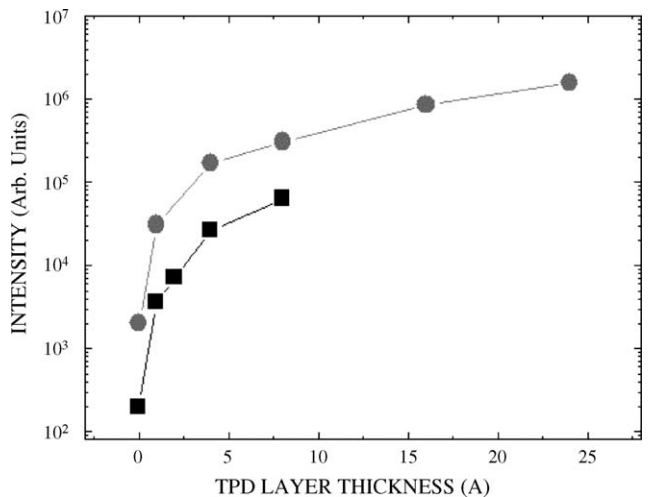


Fig. 4.11. Measured intensity of the fast component at $E - E_{\text{HOMO}} = 2.55 \text{ eV}$ for TPD on amorphous DPEP (squares) and on polycrystalline DPEP (circles). The intensities increase by 3 orders of magnitude as the TPD thickness increases (from Ref. [381]).

LUMO of TPD, the increase can only be attributed to strong electron transfer from TPD to DPEP [380,381].

5. Organic/inorganic interface

Over the past decade, the development of organic thin film transistors has gained a lot of attention, due to their promising potentials in the future applications, such as low-cost, large-area, and mechanical flexible devices [2]. For example, OTFTs based on rubrene single crystal have been reported to achieve a hole mobility of $20 \text{ cm}^2/\text{Vs}$ at room temperature [382], comparable to that of poly-Si. As the charge carrier transport has been shown to occur primarily at the interface between the dielectric and the organic material, the electronic properties of the interface between the organic and the dielectric strongly influences the device characteristics of the OTFTs. Another example of organic/inorganic interface is with indium-tin-oxide. ITO is one of the few metal oxides that combine many technologically interesting properties such as high transparency in the visible, good electrical conductivity and excellent substrate adherence. ITO/organic interface is essential for optoelectronic applications including OLEDs and OPVs.

5.1. Organic/insulator interface

In comparison with metal/organic and organic/organic interfaces, the scale of surface analytical studies of organic/dielectric interfaces is much more moderate [140,173,174,179,182,183, 190,196,296,300,383–389]. As the interactions between dielectric and organic materials are relatively weak and that dielectric materials do not have itinerant charge carriers to support an interface dipole, the organic/dielectric interfaces are typically characterized by vacuum level alignment.

SiO_2 is widely used as a gate dielectric in commercial thin film transistors. With extensive knowledge of the behavior of such devices the use of SiO_2 has also been widely used as a dielectric for organic thin film transistors. SiO_2 is generally used in two ways in organic semiconductor devices: as a buffer layer in various organic light emitting structures [390–392] and as a dielectric in organic thin film transistor structures [393–395]. The role SiO_2 plays differs in each use. When SiO_2 is used as a buffer layer between the organic material and a conducting contact it plays multiple roles. SiO_2 acts as a physical buffer between the organic material and the conducting contact in order to prevent chemical interactions between the contact and the organic material. The SiO_2 layer also acts as a barrier to charge carrier transport that reduces the number of charge carriers that are able to flow from one contact into the organic and thereby balancing the carrier injection of holes and electrons which improves the recombination efficiency. There have been limited non-device studies of the interfaces between SiO_2 and organic semiconductors. Papaefthimiou et al. investigated the interfaces between a conjugated oligomer and Si and SiO_2 using XPS and UPS [179,182,183,196,396]. Band bending was observed at the interface between the oligomer and Si but the energy level alignment at the oligomer and SiO_2 interface was not examined due to problems with charging of the 200 \AA thick layer of SiO_2 during photoelectron spectroscopy measurements [396]. Watkins and Gao investigated pentacene on Si native oxide surface, whose thickness ($\sim 1 \text{ nm}$) eliminates the charging problem while keeping the information about the interface formation intact [300]. In Fig. 5.1 the evolution of Si 2p, C 1s, and O 1s are shown as a function of pentacene deposition onto the native oxide surface of a Si wafer [300]. The C 1s peak exhibits a minimal shift of $\sim 0.05 \text{ eV}$ to higher binding energy followed by a gradual decrease in binding energy as further pentacene is deposited. A high-energy shoulder does disappear as the pentacene is deposited. This shoulder is due to the

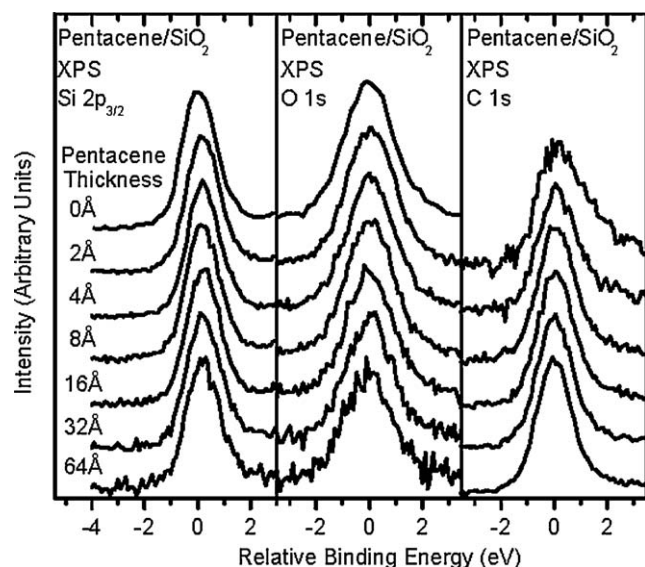


Fig. 5.1. Normalized XPS spectra as a function of pentacene deposition onto SiO_2 . The lack of significant changes in the peak shape indicates that no chemical reactions occur at this interface (from Ref. [300]).

small amount of carbon contamination on the surface of the Si oxide. The O 1s peak exhibits a small change of less than 0.1 eV to higher binding energy upon initial deposition of pentacene that is reversed upon further pentacene deposition. The main Si peak, which is from the unoxidized Si, does exhibit a small shift of $\sim 0.15 \text{ eV}$ to higher binding energy when 2 \AA of pentacene is deposited but remains constant after that. It should be noted that the Si peak that was examined was not the peak that is attributed to the Si oxide but is the peak attributed to the Si substrate. The lack of significant changes in the peak shape indicates that no chemical reactions occur at this interface between the pentacene and Si oxide.

The attenuation, based on Eq. (2.3), of the XPS peaks of the Si oxide substrate can be used to determine the growth mode of pentacene deposition onto Si oxide. As seen in Fig. 5.2, both the Si and the O peaks reduced in intensity by almost identical amounts as a function of pentacene deposition onto the Si oxide surface as would be expected by equal attenuation of both the Si and O by the pentacene [300]. Between 2 and 16 \AA of pentacene deposition the graph of the XPS peak attenuation is linear followed by linear

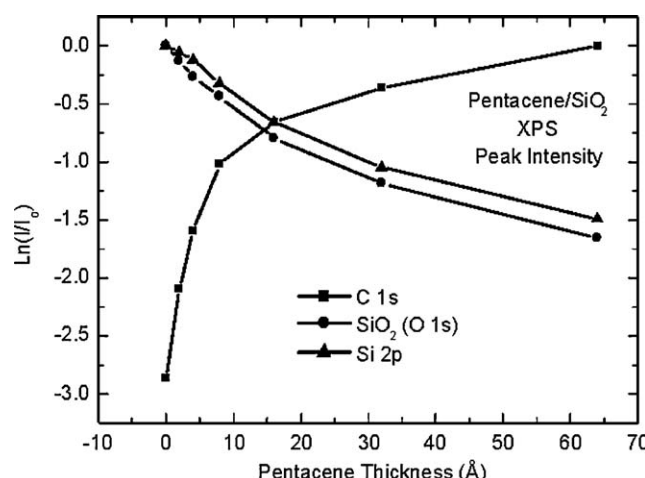


Fig. 5.2. Attenuation of the XPS spectra as a function of pentacene coverage, suggesting Stranski-Krastanov mode or layer+island growth (from Ref. [300]).

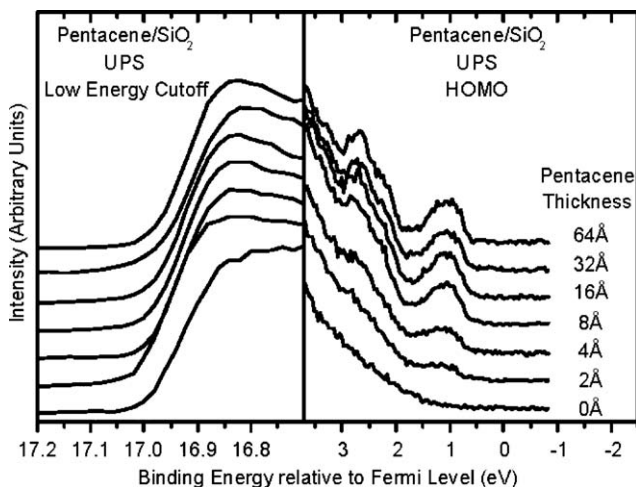


Fig. 5.3. Evolution of the UPS spectra as a function of pentacene deposition onto SiO_2 . The data suggest that there is minimal interaction (from Ref. [309]).

behavior with a slightly different slope from 16 to 64 Å of pentacene. This data leads to an electron escape depth of ~ 23 Å. This value agrees very well with an expected value of ~ 20 Å, suggesting that as pentacene is deposited onto the SiO_2 the first 16 Å of pentacene forms a single layer of pentacene, similar behavior as that seen with pentacene deposition onto a clean Si surface [397], with further pentacene deposition resulting in island growth.

The evolution of the UPS cutoff and HOMO positions as a function of pentacene deposition onto Si oxide is shown in Fig. 5.3 [309]. As indicated by the lack of change in the position of the UPS cutoff, the Vacuum level of the surface remains constant throughout the gradual deposition of 64 Å of pentacene onto the surface. After deposition of only 2 Å of pentacene the HOMO is clearly visible on in the UPS spectra. The immediate appearance of the HOMO suggests that there is minimal interaction between the SiO_2 and pentacene since greater interaction would lead to disruption of the HOMO.

The energy level diagram of the interface formed by pentacene deposition onto SiO_2 is shown in Fig. 5.4(a) [309], as deduced from the XPS and UPS data presented in Figs. 5.1–5.3 [309]. As reflected

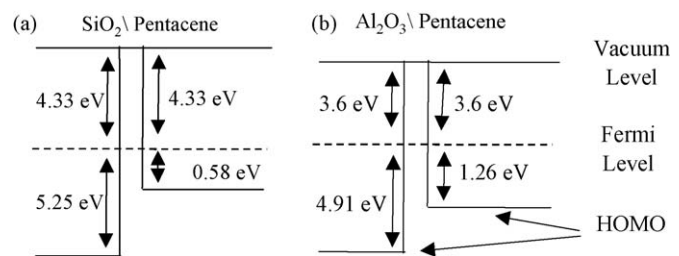


Fig. 5.4. Energy level diagram of pentacene deposition onto (a) SiO_2 and (b) Al_2O_3 , characterized by vacuum level alignment (from Ref. [309]).

in the energy level diagram, there is no significant change of energy levels in either the pentacene or the SiO_2 as pentacene is deposited onto SiO_2 . This reflects the lack of chemical interactions and the minimal electronic interaction at this interface. The alignment of the vacuum levels of the pentacene and SiO_2 indicates that if a SiO_2 layer is inserted between a metal and pentacene (or other organic materials), the vacuum level change will be dominated by the interface dipole between SiO_2 and the metal. A similar vacuum level alignment is observed between pentacene and Al_2O_3 , as shown in Fig. 5.4(b) [309].

Both examples in Fig. 5.4 are for native oxides with a fixed thickness. The dependence of the energy level alignment on the thickness of the dielectric has also been investigated. Shown in Fig. 5.5(a) are the UPS spectra of LiF with thicknesses ranging from 5 to 40 Å in 5 Å steps onto a Au substrate by Watkins et al. [173]. The peak at ~ 9 eV is from F 2p, whose binding energy differs by exactly the same amount as the vacuum level position for different LiF thicknesses. Possible contribution of O_2 or H_2O can be ruled out from the XPS analysis, and the changes in the vacuum level as the LiF layer thickness increases may be attributed to self-doping of LiF by fluorine vacancies. In Fig. 5.5(b) the UPS spectra of 32 Å of pentacene deposited onto the gradual thickness substrate are presented [173]. The major change in the spectra is the appearance of a pentacene feature at a binding energy of ~ 16 eV. An important observation is that no significant shift in the vacuum level position occurs upon deposition of pentacene onto any thickness of LiF on the substrate. This indicates that there is vacuum level alignment at the pentacene/LiF interface.

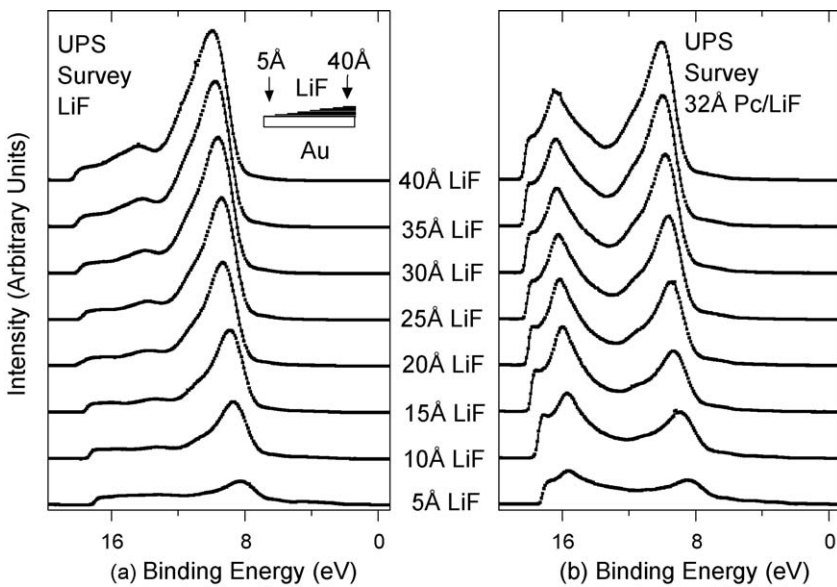


Fig. 5.5. (a) UPS spectra of various thicknesses of LiF deposited onto one Au substrate. The inset shows the sample configuration of multiple LiF thicknesses. (b) UPS spectra of 32 Å of pentacene deposited onto the multiple LiF thicknesses (from Ref. [173]).

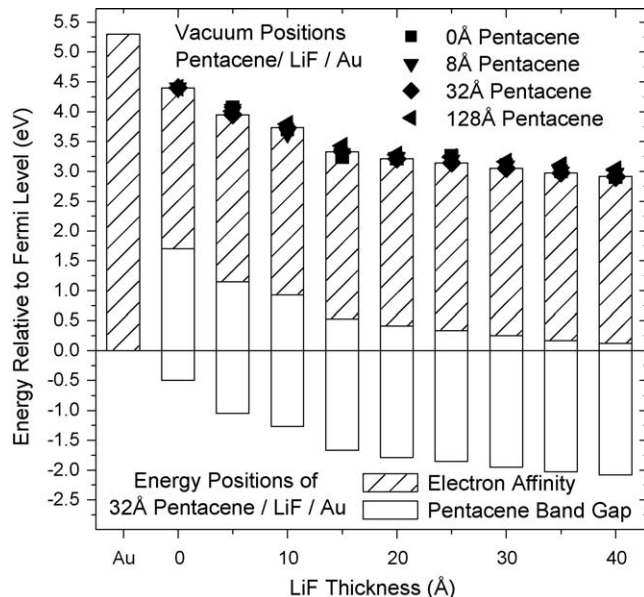


Fig. 5.6. The energy levels of pentacene deposited onto LiF coated Au as a function of the LiF thickness. The Fermi level position within the pentacene bandgap can be tuned by the LiF thickness. (from Ref. [173]).

Fig. 5.6 shows the vacuum level at the top of the columns. A thickness dependent vacuum level offset from the Au vacuum level is ranging from ~ -1.2 eV for 5 Å of LiF on Au to ~ -2.3 eV for 40 Å of LiF on Au. Also shown in **Fig. 5.6** are the measured HOMO at the bottom of the empty rectangles, and the estimated LUMO, using a band gap of 2.2 eV, deduced from combined UPS and IPES measurements, at the top of the empty rectangles [173]. As shown in **Fig. 5.6**, the HOMO of pentacene deposited onto a clean Au surface is located 0.5 eV below the Fermi level. With a LiF thickness of 40 Å the pentacene HOMO is ~ 2.1 eV from the Fermi level while the LUMO, which started ~ 1.7 eV above the Fermi level, is a mere 0.1 eV above the Fermi level. By the insertion of various thicknesses of LiF the Fermi level position within the pentacene bandgap can be tuned to be within 0.5 eV of the HOMO or within

0.1 eV of the LUMO. Attempting to take advantage of the energy level alignment in device design requires that the fundamental insulating nature of LiF be taken into account and the necessity of electron tunneling through the LiF be considered. It is clear that, regardless of the thickness of LiF, upon pentacene deposition onto LiF the pentacene vacuum level aligns with that of LiF.

Recently, an organic electrical bistable device (OBD) has been reported, comprising of a thin metal layer embedded within the organic material by Yang and his coworkers [398,399]. At room temperature, the device shows a huge current bistability, which makes it a potential candidate for memory cells. A simple sandwich structure of organic/metal/organic layers has been exploited to achieve the bistable function. It clearly suggests that the central metal layer is the key factor in the electrical bistable phenomenon. The experiments further show that in order to have a working device, the middle metal layer must be a mixture of oxide and metal nano-particles formed during the vapor deposition in a relatively low vacuum [399].

Shown in **Fig. 5.7** are the low energy secondary cut-off and the HOMO region of the UPS spectra of the Alq/AlO_x/Alq film by Ding et al. [389]. The binding energy shows in the figure are relative to the Fermi Level of the initial Au substrate. The UPS spectrum of the pristine Alq film is plotted at the bottom. The ionization potential I_P , derived from the energy difference between the HOMO extrapolation and the cut-off, is calculated to be 5.7 eV. After 30 Å Al deposition, a 0.56 eV shift toward lower binding energy can be observed in the cut-off region, leading to a work function of 4.2 eV, which is the same as that reported previously [239]. At the same time, the HOMO feature of the pristine Alq film is totally eliminated in the UPS spectrum. This suggests that a strong chemical reaction has taken place during the Al deposition. One should also note that the Fermi level of Al does not shift in comparison to that of the Au substrate. Therefore, no discernable charging effect can be found at this stage. The subsequent oxygen exposure induces a reverse shift of the cut-off. The total shift for 10000 L oxygen exposure is 0.62 eV, a situation similar to those discussed in other studies for oxidization of Al film [174]. In the HOMO region, the features from both Alq and Al become blurred rapidly in oxygen, and the Fermi level is totally eliminated at 1000 L oxygen exposure. The elimination of the Al Fermi level

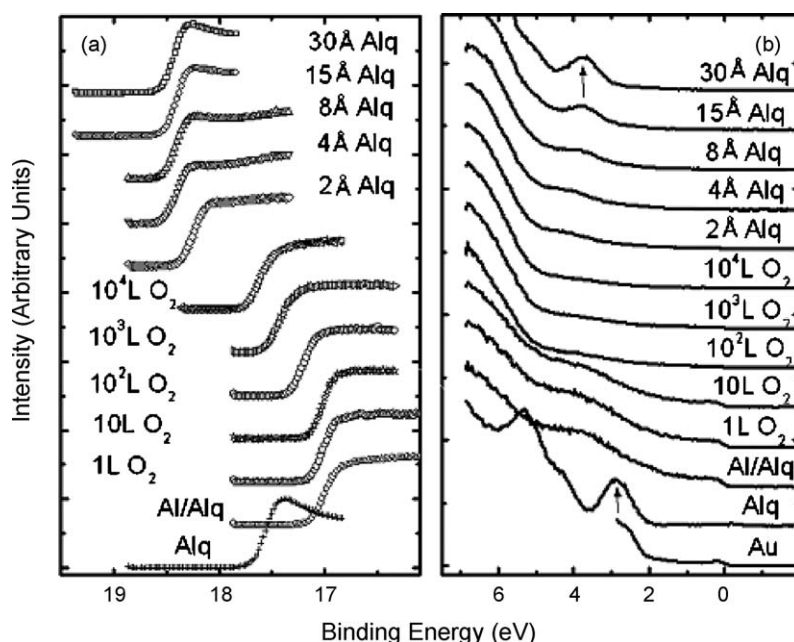


Fig. 5.7. UPS spectra evolution of Alq/AlO_x/Alq film: (a) cut-off and (b) HOMO region (from Ref. [389]).

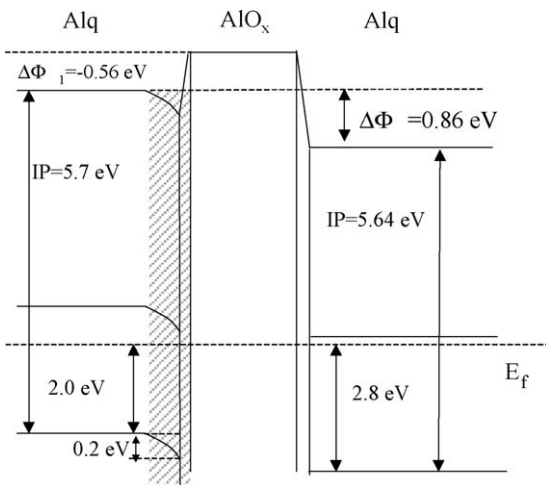


Fig. 5.8. The energy level alignment diagram for Alq/AlO_x/Alq sandwich structure, showing the difference of the top and bottom Alq layer (from Ref. [389]).

indicates that the metallic surface is destroyed by interactions with oxygen molecules, and that an aluminum oxide is formed. Subsequent deposition of a top layer Alq turns out to be more interesting, as shown in the top part of Fig. 5.7. First of all, the cut-off shifts abruptly for about 0.6 eV toward higher binding energy within the first 2 Å of Alq deposition, and after that it becomes gradual and finally saturated. A total shift of about 0.8 eV relative to the bottom Alq layer is obtained at the last step. Meanwhile, the HOMO feature recovers gradually as the coverage of the Alq layer increases. A spectrum that resembles that of a pristine Alq film is observed after 30 Å of Alq deposition. However, the HOMO position of the top Alq layer is 0.8 eV higher than that of the bottom layer. The perfect agreement of the shift in both cut-off and HOMO region leads to an IP of 5.64 eV for the top layer Alq, the same as that of the bottom layer within the experimental uncertainty.

The energy level alignment diagram at the interfaces is summarized in Fig. 5.8 [389]. The vacuum level is obtained at the maximum of the differential curve of the cut-off spectrum. For the bottom Alq film drawn in the left of Fig. 5.8, the HOMO is located 2.0 eV below the Fermi level. The shaded area at the Al/Alq interface indicates the region where the chemical reaction takes place. The changes in core level binding energy reflect a 0.2 eV shift toward higher binding energy at this region after the initial Al deposition, whereas the cut-off gives a 0.56 eV shift toward lower binding energy in the vacuum level. The LUMO, which cannot be observed directly from the photoemission experiment, is estimated by assuming the optical gap of Alq as the difference between the HOMO and LUMO energy. On top of the Al/Alq interface region a metallic Al layer is formed, evidenced by the Fermi level in the UPS spectrum and the workfunction of 4.2 eV.

The subsequent oxygen exposure introduces both metallic and oxidized state at the interface, reducing the work function by about 0.6 eV. However, the energy levels of Alq substrate do not shift much during the process. The deposition of the top Alq layer leads to an abrupt shift in vacuum level within the first 4 Å. Considering the size of the organic molecules, the shift should be attributed to the formation of an interface dipole. As a result, a dramatic asymmetry is observed: there is a 0.8 eV shift toward higher binding energy for all the energy levels of the top layer Alq relative to those of the pristine bottom layer Alq. The electron injection barrier, which is determined by the energy difference between the LUMO and the Fermi level, is reduced at the Alq/AlO_x interface. Considering the 0.2 eV shift induced by chemical interaction at the

Al/Alq interface, a difference of 0.6 eV in the electron injection barrier is obtained at these two interfaces. The LUMO of the top layer Alq is very close to the Fermi level of the system, resulting in a much smaller electron injection barrier from the top side. Although the detailed explanation for the bistable function of this kind of device structure remains unclear, the diagram shown in Fig. 5.8 provides useful information on the electronic structure of the system.

The energy level alignment at the interface between the top layer Alq and the AlO_x reveals a behavior that differs from the usual assumption of a common vacuum level between organic and oxide. It is expected that deposition of organic molecules onto a thick layer of metal oxide will not lead to an interface dipole, since charge transfer does not occur during the process. This is because the oxygen exposure was conducted in a UHV chamber and the sample was kept in pure oxygen, without limited oxygen exposure resemble to that in a typical OBD device fabrication. The low oxygen exposure led to an unsaturated oxidation and the interface electronic structure is still influenced by the remaining metallic feature of the oxygen exposed Al surface [400].

5.2. ITO surface treatment and its interface with organics

ITO is one of the few metal oxides that combines many technologically interesting properties such as high transparency in the visible, good electrical conductivity and excellent substrate adherence [6,38,77,78,80,82–90,92–94,106,111,112,125,135,136,144,152,161,167,168,177,192,194,228,230,233,234,238,242,244,254,258,261,265,270,273–275,289,299,321,322,326,328,353,356–358,386,401–451]. Organic optoelectronic device performance has been further enhanced by a variety of ITO surface treatment technologies including, depositing a thin carbon layer [452], polyanilane (PANI) [453,454], poly(3,4-ethylene dioxythiophene) (PEDOT) [454,455], or by oxygen plasma [1,455,456]. For small molecule devices, the device stability is dramatically increased by interposing a CuPc layer on the ITO anode [457]. It had been suggested that the CuPc layer lowers the drive voltage by reducing the effective barrier between the ITO and the NPB hole transporting layer [96,458]. Conversely other researchers have shown that relatively thick, 15 nm CuPc layers, will in fact reduce the rate of hole injection from the ITO anode leading to a better balance with the electron current arriving from the cathode to the recombination zone [459]. In the latter work it was also demonstrated that an excess of holes in the Alq layer would create an unstable cation population leading to a rapid degradation in device performance.

Fig. 5.9(a) shows a typical UPS spectrum for ITO in kinetic energy scale by Park et al. [451]. The spectrum was taken for -3.000 V sample bias so that the sample inelastic cutoff could be distinguished from that due to the spectrometer which is observable in Fig. 5.9(a) as a small peak near 2 eV. This figure also illustrates the relation between the width of the spectrum, and sample work function ϕ and photon energy. The spectrum width is determined from the distance between the sample inelastic cutoff and the Fermi edge as illustrated in Fig. 5.9(b) and (c), respectively. Ideally, these edges should be infinitely abrupt but due to the limited spectrometer resolution and thermal effects, they are broadened. The actual positions are determined as the center of the slopes as indicated with vertical lines. The measured work function of ITO is 4.4–4.5 eV, depending on the surface treatments, with estimated error less than 0.02 eV. The determination of the position of inelastic cutoff was unambiguous for all samples while the Fermi edge did not readily show up for some samples. However this did not pose a problem because the Fermi edge is the reference point of energy scale in photoelectron spectroscopy and should not change from sample to sample as long as they are grounded. Nevertheless we checked the position of Fermi edge using Au films electrically connected and positioned next to ITO sample [451].

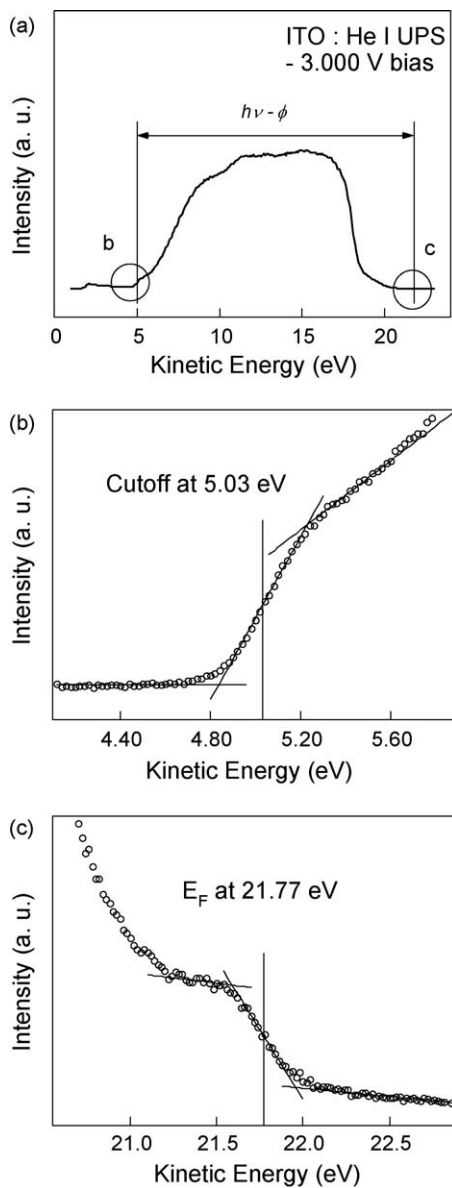


Fig. 5.9. (a) A typical UPS spectrum of ITO, (b) detailed spectrum of inelastic cutoff region, (c) Fermi edge region (from Ref. [451]).

While the workfunction of clean ITO surface is typically 4.5 ± 0.1 eV, it can depend on the composition and surface treatments. Ding et al. reported that ITO surface treated in situ by oxygen plasma possessed a work function of 5.2 eV, while other treatments gave $\Phi = 4.5 \pm 0.1$ eV, including as-loaded, vacuum annealed, ex situ ozone exposed, ozone exposed and annealed, oxygen plasma exposed and annealed treatment [405]. The modification of ITO workfunction can significantly change the hole injection barrier. Fig. 5.10 shows the UPS spectra taken after the NPB deposition on the different ITO surfaces [405]. The barrier height, expressed as the separation between the HOMO threshold and the Fermi level E_F of ITO, can be determined for the differently treated NPB/ITO interfaces. The lowest barrier height here is 0.7 eV, emerging from immediate deposition of NPB onto the ITO treated with $\Phi = 5.2$ eV after in situ oxygen plasma treatment [405].

The most profound effects are found in ITO surfaces treated with phosphoric acid (H_3PO_4) and tetrabutylammonium hydroxide [$N(C_4H_9)_4OH$] that result in the highest work function shifts with respect to that of the standard ITO, +0.7 and -0.6 eV respectively [167,168,449,451]. It is found that the position of the

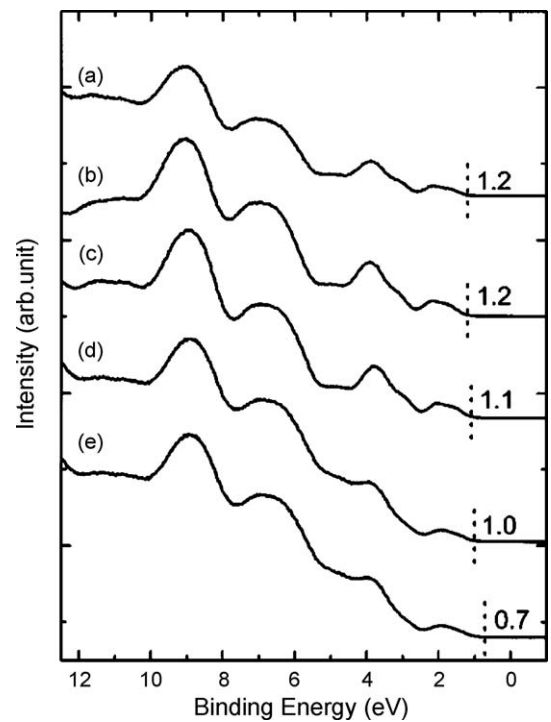


Fig. 5.10. UPS spectra of NPB/ITO with the ITO substrates (a) air exposed or vacuum annealed, (b) *in situ* OPA treated, (c) ozone exposed and annealed, (d) *ex situ* ozone exposed, and (e) *in situ* OP exposed (from Ref. [405]).

HOMO of the deposited organic material depends on the work function of the ITO substrate and that the acid-treated ITO gave the lowest hole injection barrier. No significant reactions are observed between standard ITO and NPB, but acid treated ITO presented interesting effects of the protons in the adsorbed acid layer. The diagrams in Fig. 5.11 summarize the energy alignment at the ITO/NPB interface derived from UPS measurements on the various ITO treatments by Nuesch et al. [449]. The barrier to hole injection from the ITO anode is taken as the energy difference between the Fermi level of ITO and the HOMO of NPB. The barrier height decreases significantly from 1.61 to 1.09 eV for base and acid-treated ITO, respectively, with the standard ITO having an intermediate value (1.35 eV). The microscopic mechanism that governs the improvement in charge injection can be extremely complex, but it is clear in the present case that the increase in the anode work function contributes to the improvement in turn-on voltage of OLEDs.

6. Interface engineering

Interface engineering has been an effective means to improve OSC devices. Early approach of Mg–Ag alloy as cathode has been widely used for OLEDs [1]. However, the reactive nature of Mg is one of the limiting factors to the OLED lifetime, and it is preferable a more stable materials be used for the cathode. More approaches have been attempted for forming an efficient and stable cathode is by introducing a thin layer of an ionic insulator such as LiF [460–462], MgO [460], SiO₂ [390–392] or MgF₂ [463] at the Al/organic interface, or doping the organic layer (or the cathode) with LiF [464] (or Li [465]), which significantly enhance the electron-injection and prolong the device lifetime [38,45,83,85,88,93,122,160,165,187,188,211,227,233,236,239,241,245,250,262,264,274,275,284,287,350,384,419,423,432,438–441,447,466–488].

As with the cathode/organic interface, the hole injection efficiency from the ITO anode to the hole transporting organic

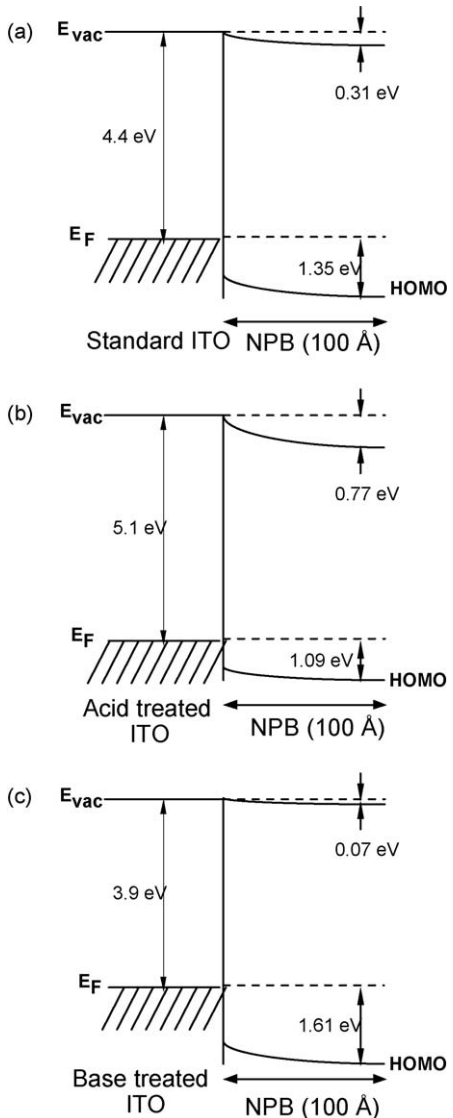


Fig. 5.11. Energy diagram deduced from UPS measurements for (a) NPB/standard ITO, (b) NPB/acid-treated ITO, and (c) base-treated ITO (from Ref. [449]).

layer is tuned through interface engineering and selecting organic molecules with energy alignments that favor ohmic injection from the ITO anode [489].

6.1. Doping

Doping is widely used to improve organic semiconductor devices, analogous to that in the inorganic semiconductor industry [14,48,73,94,95,100,123,128,142,155,169,198,228,235,241,242,253,259,260,279,283,285,291,368–370,400,426,427,430,450,471,472,483,490–516]. Doping in OLEDs is a widely used method to convert the emission wavelength and to improve the efficiency. For alkali metal/organic interface, doping of organic materials often causes significant energy level shift in these materials and it is of both fundamental and practical interest. Kido et al. reported doping of tris (8-hydroxyquinoline) aluminum (Alq) with Li near the cathode interface significantly improved the device performance, and the highest luminescence is observed with the ratio Li/Alq = 1 (atom/molecule) [465]. Lous et al. and Heller et al. observed that doping of C₆₀ can result in the Schottky barrier formation [517,518]. Yang et al. and Sheats et al. successfully used doped polyaniline as a buffer layer between the anode and a hole

transport layer, which results in efficient suppression of leakage currents [519,520]. Alkali metals, which can be easily used as electron donors, are good candidates for prototypical studies due to their simple electronic structures and low electron affinity. Alkali metal doping in commonly used organic semiconductors, such as CuPc [368,369], Alq [241,502], and PTCDA [521,522] has been investigated by several groups [14,48,73,94,95,100,123,128,142,155,198,228,235,239,241,242,253,259,260,279,283,285,291,342,368,369,427,430,471,472,483,490–510,514,523–552]. The experimental results suggest that doping of alkali metals in organic semiconductors induces energy level shift due to electron donation from the outmost s orbital. Doping has also been shown to form polaron lattice in polymers [14,150,190,197,283,328,385,408,479,553,554].

The evolution of the electronic structure of Cs:CuPc for both the HOMO and the LUMO region is plotted in Fig. 6.1 by Ding and Gao [515] as a function of Cs doping ratio R_{Cs} , the Cs atom to CuPc molecule ratio, which is obtained from the XPS core level intensities. For $R_{Cs} < 0.8$, a monotonic shift toward high binding energy can be observed for all the features in the UPS spectra. It is very interesting that the IPES spectra show a similar shift for the low doping ratios. The amount of the shift for the LUMO at $R_{Cs} = 0.8$ is identical to that of the HOMO, which confirms that the shift is rigid shift in energies. It suggests that the electronic structure of CuPc molecule is well preserved under low doping ratios, and that the energy level shift at this stage is mainly due to the Fermi level shift within the energy gap. Another issue worth mentioning is that, due to the downwards shift and the doping-induced broadening, the position of the LUMO onset in the IPES spectrum is very close to the Fermi level at this doping level. For more Cs doping, the shift of all energy levels becomes saturated. The saturation of the energy level shift provides direct evidence for Fermi level pinning in heavily doped system, as proposed previously by Yan et al. [368]. Although the energy level shift has saturated, the shape of both the UPS and IPES spectra are significantly modified at higher doping ratios. A new state emerges from the former energy gap in the UPS spectrum, and its intensity increases monotonically as R_{Cs} increases. The peak separation between the HOMO and the gap state is about 1.0 eV, which remains the same for all doping ratios. At the same time, the intensity of the CuPc LUMO in the IPES spectra starts to decrease as R_{Cs} increases. The increase of the intensity of the gap state, at the expense of that of the LUMO, further confirms the previous assumption that the gap state induced by n-type doping is originated from the filling of the former LUMO in the CuPc molecules [241]. For high doping ratios, the spectral broadening becomes more and more pronounced in both the UPS and IPES. For $R_{Cs} = 3.2$, the HOMO and the gap state are so broad that they almost merge together. Similar broadening can be found in the IPES spectra, where the LUMO becomes too weak to be visually distinguishable. Finally, it should also be noted that no Fermi edge could be observed in the UPS spectra for doping ratios as high as 3.2, indicating a non-metallic surface [515].

Due to the low cross-section of IPES and the vulnerability of organic materials to electron exposure, multiple IPES measurements on the same organic surface are unreliable and as a result, most of the IPES measurements of organic materials are done by taking only once the snap shot of the surface [42,153,171,199,210,230,254,285,310,368,433,466,492–495,499,501,555,556]. The work in Ref. [515] is made possible by moving the sample to have a surface fresh from electron exposure for each IPES measurement while keeping other experimental conditions identical.

The intensity evolution of the frontier orbital is shown in Fig. 6.2 [515]. In this plot, the intensity of the LUMO is calibrated by that of the LUMO + 1 of the same IPES spectrum to remove the uncertainty of the electron flux from measurement to measurement. Similar

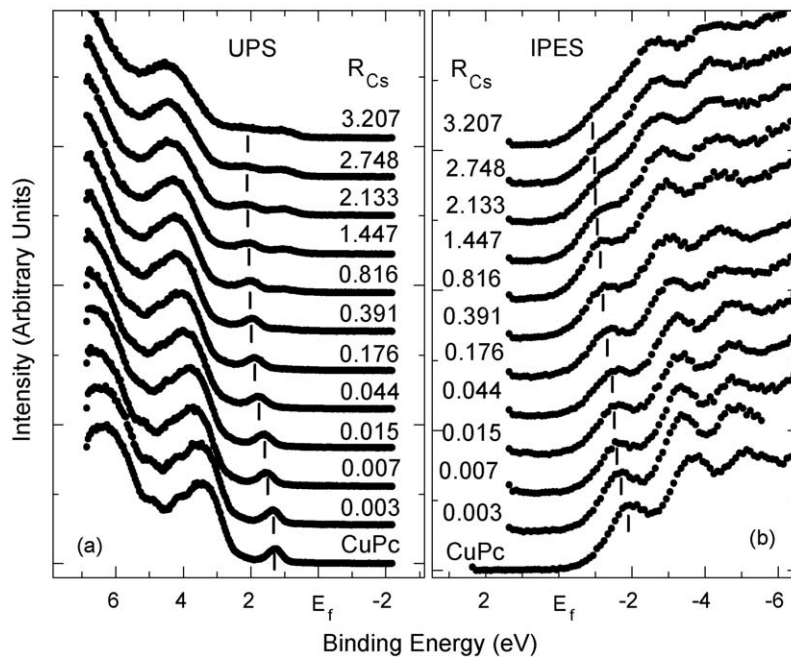


Fig. 6.1. Evolution of the HOMO (a) and the LUMO (b) region in the UPS and IPES spectra of Cs:CuPc as a function of Cs doping ratio R_{Cs} . The increase of the intensity of the gap state is at the expense of that of the LUMO (from Ref. [515]).

calibrations have been employed for the intensity ratio between the gap state and the HOMO in UPS. The assumption is that the intensities of the LUMO + 1 and the HOMO remain relatively unchanged since Cs doping involves mainly the modification of the LUMO and the gap state. There is hardly any change in the LUMO intensity at low doping ratios, and it starts to decrease at the same time when the gap state rises. At $R_{Cs} = 3.2$, the LUMO intensity has been reduced by 60%. Assuming that the first main feature in the IPES spectra consists of only the LUMO with double degeneracy [557], it can be deduced that 2.4 electrons have been transferred into a single CuPc molecule. This doping ratio estimated from LUMO intensity is substantially lower than R_{Cs} from the XPS core level intensities. The discrepancy can be partly attributed to the attenuation of the C 1s core level intensity in the XPS spectra at high ratios, as well as possible incomplete ionization of the Cs

atoms. The charge transfer amount per molecule can be estimated from the gap_state/HOMO intensity ratio as well. According to the gaussian fitting, the gap_state/HOMO intensity ratio at $R_{Cs} = 3.2$ is derived to be about 1.1. The doping ratio can then be estimated to be 2.2, if one can assume that the HOMO consists of only one orbital. Base on these ratios, we suggest that multiply charged CuPc species exist in the heavily doped film. The multiply charged CuPc species must have been stabilized by the nearby Cs^+ counter ions, as multiple charging is energetically unfavorable for isolated CuPc molecule [558].

In Fig. 6.3, the XPS spectra of the C 1s, N 1s, and Cu 2p_{3/2} core level of Cs:CuPc are presented as a function of R_{Cs} [559]. The C 1s core level consists of three visible peaks. The main peak (C 1s(A)) as marked in Fig. 6.3) can be easily associated with the aromatic rings of CuPc. The second peak (C 1s(B)) is due to the pyrrole carbon in contact with N, with some contribution of C 1s(A) satellite. The third (C 1s(C)) is a $\pi-\pi^*$ satellite feature from the pyrrole carbon as pointed by Schwieger et al. [560]. The first thing to notice is that all the three core levels shift toward higher binding energy as R_{Cs} increases. However, the shift of Cu 2p_{3/2} and N 1s saturate or even reverse slightly as R_{Cs} increases beyond 0.8, whereas that of C 1s does not show any obvious reversion. Another important feature is that while the shapes of the Cu and N core levels remain of little change, the three components of C 1s at higher Cs doping ($R_{Cs} \geq 2.7$) merge into one broad and asymmetric peak. The different behaviors of the core levels at higher doping levels indicate that the electronic structure of CuPc is significantly modified at this stage. The evolution of the core levels in alkali metal-doped CuPc turns out to be a general behavior, as similar results found in Na-doped CuPc by Ding et al. [514].

For Cs-doped CuPc, the energy level shifts can be summarized as in Fig. 6.4 [559]. The vacuum level cutoff was obtained at the maximum of the differential curve of the UPS spectrum. HOMO and LUMO were determined by the extrapolation of the leading edge in the UPS and IPES spectra, respectively. The core level shifts were deduced by fitting the spectra with Gaussian curves for C 1s, N 1s, and Cu 2p_{3/2}. The C 1s core level consists of two main components: the leading peak C 1s A, which can be associated with the aromatic carbon of the benzene rings, and second peak C 1s B, which is due

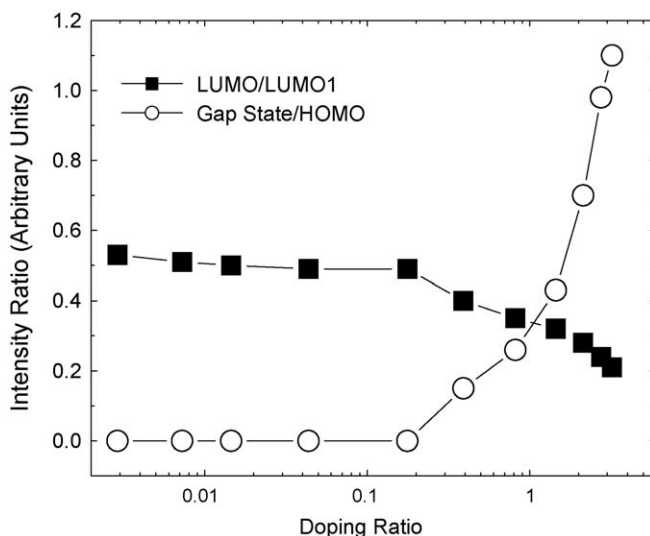


Fig. 6.2. The evolution of the LUMO/LUMO+1 and the gap state/HOMO intensity ratio of Cs:CuPc as a function of R_{Cs} . The data suggest multiply charged CuPc species exist in the heavily doped film (from Ref. [515]).

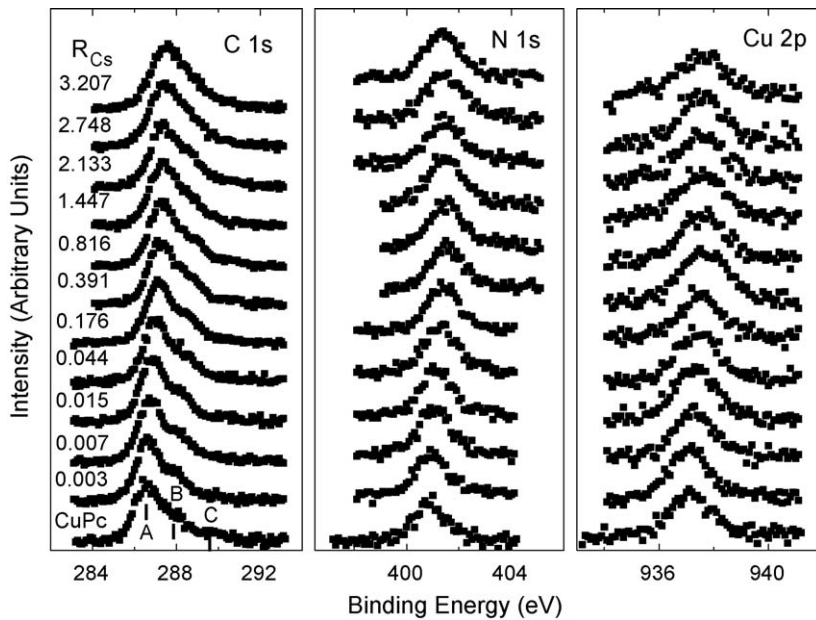


Fig. 6.3. XPS spectra of C 1s, N 1s, and Cu 2p_{3/2} core level as a function of the doping concentration R_{Cs} (from Ref. [559]).

to the pyrrole carbon in contact with N [560]. Note that R_{Cs} is in logarithmic scale to emphasize the initial shift. The energy level shift induced by Cs doping can be seen in two stages. At the first stage where the Cs doping ratio is below 0.8, all energy levels shift simultaneously and linearly in the semi-log plot. By linear fitting, the slope of the energy level shift can be estimated to be 0.127 eV, which is more than four times $k_B T$ (0.026 eV), a value that is dictated by the classical theory for inorganic semiconductors as Eq. (1.8). One should also note here that at this stage, the amounts of the shift for all the energy levels are very close, especially for that of the HOMO and LUMO. This suggests that the rigid shift assumption is still valid under low doping ratios. As the doping ratio increases, the modification of the CuPc electronic structure moves into a second stage, characterized by the diverse behaviors for different energy levels. For the frontier orbital, the HOMO and the LUMO shift simultaneously, while the vacuum level shifts much further toward high binding energy. For the core levels, a reversal of the energy level shift is observed for N 1s, Cu 2p_{3/2}, and

C 1s B, which can be attributed to the correlation effect as the donated electrons start to alter the electronic structure of CuPc. The reversal shift for the core levels occurs coincidentally with the appearance of the gap state in the occupied region and the reduction of the LUMO in the unoccupied region, which further corroborates the explanation given above.

Such a two-stage doping process can also be found in other alkali metal-doped organic semiconductors. The slope of the line drawn from the first several data points is 0.28 eV for Cs-doped Alq, which is even larger than that of the Cs-doped CuPc. The slope of Na-doped Alq deduced from cutoff data is 0.22 eV, noticeably smaller than the case of Cs doping. For cases, both samples show a saturation of the energy level shift, as well as a reverse shift for some of the core levels. At the same time, the electronic structure of Alq has been significantly modified, evidenced by the appearance of the gap state and the splitting of N 1s core level. The difference between Na and Cs doping in Alq may arise from the fact that the electron affinity of Na (0.55 eV) is larger than that of Cs (0.47 eV) [15]. As a result, the ionization of Na is less complete than that of Cs, resulting in some neutral Na capable of further chemical reaction with the O in Alq.

The fundamental difference between an organic and inorganic semiconductor is the bonding. The covalent bonding prevailing in inorganic semiconductors results in a large electronic wavefunction overlap, which is the basis for forming the Bloch waves and band structure. In organic semiconductors, however, the bonding is predominately van der Waals and the electronic structure remains largely molecular and localized. The localized nature of the electronic structure causes large correlation effects, either electron-electron or electron-phonon. If the molecular orbital were fully isolated from the doping metal atom, one would expect a same energy level dependence on the doping density as Eq. (1.8), i.e. logarithmic with slope of $k_B T$ in the semi-log plot. However, a broad exponential distribution of the LUMO, caused by metal-organic interaction, may result in a linear behavior in the semi-log plot. The slope is then given by the exponential width Γ that can be much larger than $k_B T$,

$$n \approx N_0 \exp \left[\frac{-(\varepsilon_0 - \varepsilon_F)}{\Gamma} \right], \quad (6.1)$$

where ε_0 and N_0 are the energy and density of the LUMO, respectively. Another surprise from the alkali metal doping

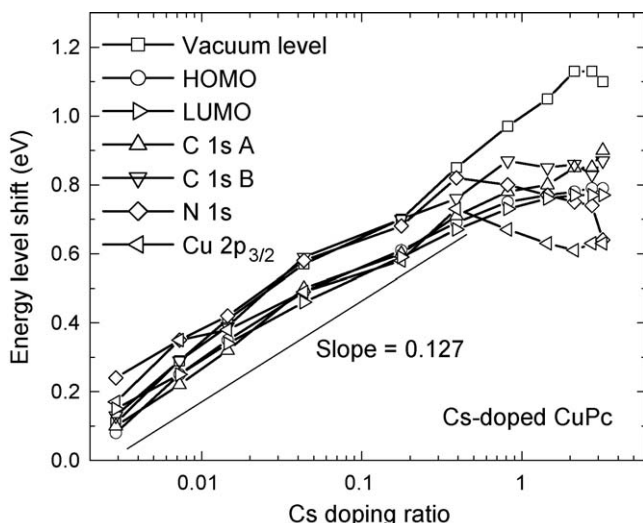


Fig. 6.4. The energy level shift of Cs-doped CuPc as a function of R_{Cs} . Note that R_{Cs} is in logarithmic scale to emphasize the initial shift. The slope is four times $k_B T$ (0.026 eV), which is predicted by the classical theory in Eq. 1.8 (from Ref. [559]).

experiments is that the slope cannot be explained by a Gaussian broadening of the LUMO. If the energy distribution is a broad Gaussian, with width $\sigma \gg k_B T$, the electron concentration will be dominated by the Gaussian and the charge density given by

$$n \approx N_0 \left\{ 1 - \operatorname{erf} \left[\frac{(\varepsilon_0 - \varepsilon_F)}{\sigma} \right] \right\}, \quad (6.2)$$

where $\operatorname{erf}(x)$ is the error function. Experimentally, both UPS and IPES peaks appear to be Gaussian. My group has attempted to fit the data in Fig. 6.4 with Eq. (6.2) to see if the energy level shift can be explained by Gaussian broadening. However, the curve from Eq. (6.2) bends opposite to that of the experimental data, indicating that Eq. (6.2) cannot be applied in this case.

6.2. Reversal of doping induced energy level shift

The above results indicate that by alkali metal doping, the electronic structures of the organic semiconductors can be modified and the electron injection barrier can be minimized to achieve a lower driving voltage and higher efficiency. However, fundamental issues still remain, such as whether the electronic structure modification is simply due to charge transfer, or more profound molecular structure modifications and chemical reactions are responsible. At the same time, the environment for the doped organic thin films can be complicated in the real device applications. Therefore, it is interesting to study the energy level modification of doped organic semiconductors under the presence of the opposite dopant, such as Au and oxygen.

Shown in Fig. 6.5 are the UPS spectra of both the low energy secondary cutoff and the HOMO region for Au deposition on Cs-doped Alq film by Ding and Gao [511]. The Fermi level derived from the Au substrate is drawn as the dashed line. Determined from the XPS core level intensities, 0.86 (atom to molecule ratio) Cs was doped into the Alq film before Au evaporation. According to a previous studies [495,516], the energy level shifts are fully saturated at this doping density. It can be seen that, after doping, the cutoff shifts toward high binding energy by about 1.0 eV, and a significant gap state 1.6 eV above the HOMO is introduced. It is very interesting that the initial deposition of 1 Å Au completely quenches the gap state while not inducing much shift in the cutoff

and HOMO. As the Au coverage increases, the cutoff shifts backward to low binding energy until it saturates after 30 Å of Au deposition. The total reverse shift is about 0.7 eV, and the final work function of 3.4 eV is substantially lower than that of pure Au (5.4 eV). Similar reversal of the Cs-induced shift can also be observed in the HOMO region. The Alq peaks become broadened and shift monotonically toward the Fermi level as the Au coverage increases. However, an important difference from the cutoff shift is that the HOMO shifts faster and the saturation position actually turns out to be that of the pristine Alq film. Another interesting observation is that, after the annihilation of the gap state, the shape of the Alq HOMO peak does not change much by further Au depositions. The persistence of Alq HOMO feature even up to 60 Å of Au indicates that no significant chemical reaction has taken place. Finally, it should be noticed that the Fermi level, which can be seen beyond 15 Å Au coverage, is the same as that of the Au substrate. Therefore, the charging effect during the measurement was insignificant at this stage [511].

The simplest explanation of the reversal of the energy level shift is the compensation of the n-doping Cs by the p-doping Au as frequently observed in crystalline inorganic semiconductors. However, more detailed analysis shows that the situation in an organic semiconductor can be more complicated. The energy level shifts of Au on Cs and Na doped Alq are summarized in Fig. 6.6(a) and (b), respectively by Ding and Gao [502]. The core level shifts were deduced by fitting the spectra with Gaussian curves for C 1s, Cs 3d_{5/2}, and Au 4f_{7/2}. The vacuum level cutoff was obtained at the maximum of the differential curve of the UPS spectra. The cutoff and HOMO positions of the pristine Alq film are also presented as the very first points to compare with the doped cases. The deposition of Au causes a significant reversal of both the frontier orbital and the core levels. There is a dramatic shift of 0.6 eV for Cs 3d_{5/2} at low Au coverage (1~2 Å), while the shift for C 1s, on the same time, is less than 0.1 eV. The abrupt shift of Cs 3d_{5/2} may stem from the removal of the donated electron from the N of Alq⁻. This explanation is supported by the quenching of the gap state in the HOMO region, which is observed to be affiliated to the formation of Alq⁻. Another important observation is that while the HOMO shift totally back to that of the undoped Alq, the C 1s peak does not. It saturates after shifting about 0.4 eV, which is only halfway toward

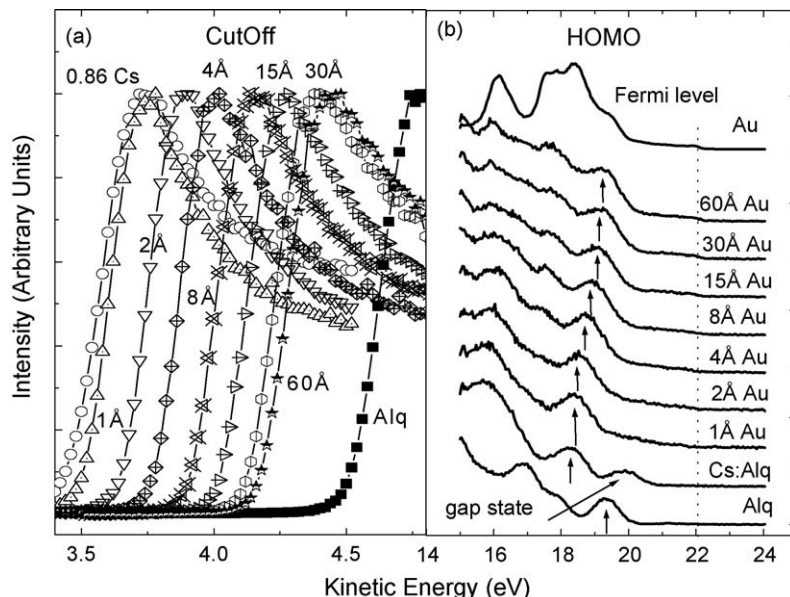


Fig. 6.5. The UPS spectra evolution as a function of Au thickness deposited onto the Cs-doped Alq film: (a) cutoff and (b) the HOMO region. As the Au coverage increases, the Cs induced shift is gradually reversed. (from Ref. [511]).

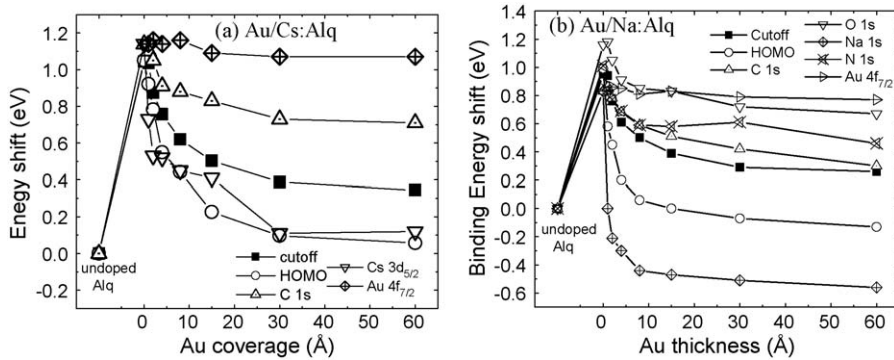


Fig. 6.6. The summarization curves of energy level shifts for Au on Cs-doped Alq (a) and Na-doped Alq (b) film. The modification of the Alq electron energy levels by Cs doping cannot be fully compensated by simply removing the electrons from the host (from Ref. [502]).

that of the pristine Alq film. Apparently, the modification of the Alq electron energy level shift by Cs doping cannot be fully compensated by simply removing the electrons from the host [502].

6.3. Insertion of ultra-thin interlayers

Inserting an ultra-thin interlayer has been an important means in modifying the performance of OSC devices. Here LiF is taken as an example to illustrate some of the characteristics observed with surface analytical tools. Thin LiF layer between the electron-transporting organic layer and metal cathode has been widely practiced in organic optoelectronic devices to enhance electron transport from the organic to the cathode. Early suggestion by Hung et al. [460] was that the LiF layer reduced the electron-injection barrier height, but it is also found that it depends strongly on the metal deposited on top of the LiF [561]. Schlauf et al. measured the electronic structure of LiF on Al and Pt, and attributed the injection improvement to band bending in LiF caused by charged defect [562]. Wang et al. attributed the improvement to energy level realignment by interface dipole [563]. More recently, Zhao et al. suggested that tunneling in LiF and thus induced energy level realignment are responsible to the electron injection improvement [564].

In Fig. 6.7, the UPS spectra by Le et al. are presented for Al depositions onto clean Alq and Alq with the 5 Å LiF buffer layer [239]. The HOMO and is attributed to the π -orbital located on the

phenoxide side of the quinolate ligand [565]. Deposition of an Al layer as thin as 0.2 Å represents a significant change in the valence spectrum of Alq and induces the formation of new states which extend into the energy gap. The fingerprint of the Alq structure has virtually vanished after deposition of 0.7 Å Al, indicating the relatively strong reaction between the Al atoms and the Alq molecules. The appearance of the Al Fermi level for $\Theta_{\text{Al}} = 4 \text{ \AA}$ is in good agreement with the XPS results, for which the Al metallic peak begins to grow after deposition of the same Al thickness [239]. The spectra observed with Al deposition are consistent with an extensive chemical reaction forming a product significantly different from Alq. The new states observed in the energy gap are a reflection of the molecular orbital structure of this reaction product.

As shown in Fig. 6.7, the presence of a thin LiF layer on the Alq surface does not substantially modify the HOMO position of Alq. The deposition of aluminum induces new states above the HOMO in the energy gap, and results in a shift of the HOMO position to higher BE. These states are fundamentally different from those formed in the absence of LiF. The molecular orbital structure of Alq is preserved with LiF present. States are shifted to higher binding energy and the gap-state that is formed is well defined. In the absence of LiF, the molecular orbital structure of Alq is broadened beyond recognition even at very low coverages of Al. The states that are formed in the gap appear to result simply from an extreme line broadening as a result of the Alq decomposition process. The presence of the LiF layer not only decreases the extent of the

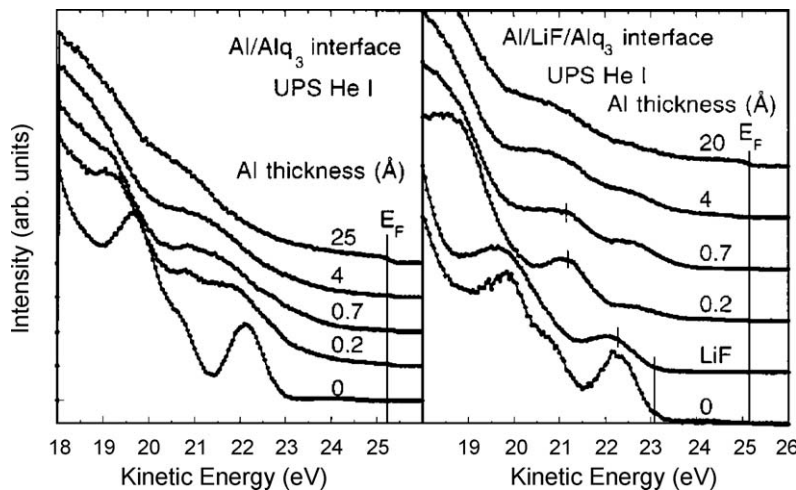


Fig. 6.7. Evolution of the UPS spectra as a function of Al thickness for Al/Alq and Al/LiF/Alq interfaces. The deposition of Al on LiF covered Alq causes significant energy level shift (from Ref. [239]).

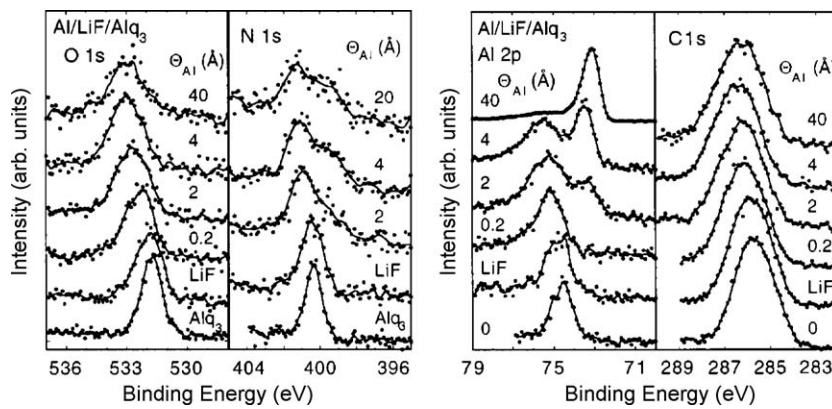


Fig. 6.8. Evolution of XPS O 1s, N 1s, Al 2p, and C 1s spectra as a function of Al coverage observed at the Al/LiF/Alq interface. The data suggest that LiF partially protects the Alq surface from reaction with the deposited Al (from Ref. [239]).

reaction with Al, it decreases the thickness of the reacted layer. The Alq valence band is still identifiable at $\Theta_{\text{Al}} = 4 \text{ \AA}$, and the Fermi level is observed at an Al coverage as low as 2 \AA .

Shown Fig. 6.8 are the O 1s, N 1s, Al 2p, and C 1s spectra with 5 \AA LiF insertion layer and with increasing Al coverage [239]. An unfortunate result of the LiF deposition is a significant increase in the observed line widths. This probably results from the incomplete coverage of the surface that causes it to be very inhomogeneous. With the exception of the C 1s peak, all core levels showed significant broadening with LiF and subsequent Al deposition. The increased full width at half maximum (FWHM) with overlayer deposition makes it difficult to resolve multi-component lines. This effect is most relevant in the O 1s spectrum. Although this appears to remains a single-component peak for all Θ_{Al} and shows none of the asymmetry characteristics of the Al/Alq interface, some asymmetry may be hidden by the increased line width. The FWHM does increase from 1.17 to 1.45 eV with the deposition of LiF and to 1.89 eV for $\Theta_{\text{Al}} = 20 \text{ \AA}$. Even though no splitting is observed, such a significant increase in line width suggests a substantial alteration of the oxygen environment. In contrast to the O 1s spectrum, a new component in the N 1s spectrum is observable at $\approx 1.6 \text{ eV}$ to lower binding energy, even at the lowest coverage of Al. The intensity of this reacted component is higher than in the case of Al on Alq in the absence of the LiF layer. The pyridyl species appears to be significantly modified by even a small amount of deposited Al. The evolution of the Al 2p signals is similar to that of the Al/Alq interface but the magnitude of the shift is significantly greater. Furthermore, the metallic component appears at a significantly lower coverage suggesting that that LiF, at least, partially protects the Alq surface from reaction with the deposited Al. In the absence of LiF, the metallic signal is first noticeable at a coverage of $\Theta_{\text{Al}} = 4 \text{ \AA}$, whereas a similar relative contribution of the metal is observed at $\Theta_{\text{Al}} = 2 \text{ \AA}$ when the LiF layer is present.

The XPS and UPS spectra of Al on Alq shown in Section 3 appear to be understandable simply in terms of a “destructive” chemical reaction between the organic and the reactive metal. To understand the role of LiF in modifying this interface, we consider the results of previous work involving alkali and alkali earth metals deposited on Alq. The metals: Ca, Mg, Na, K, or Li on Alq have been studied by XPS and UPS and show remarkably similar characteristics [241]. In all cases the core levels shift to higher binding energy. The N 1s peak splits with a separation between 1.6 and 1.8 eV, and the O 1s broadens significantly but symmetrically. In the UPS spectra, the HOMO shifts to higher binding energy and a new state is formed in the previously existing energy gap and is separated from the original HOMO by 1.6 eV. All of these characteristics are observed in our case of aluminum deposited

on the Alq with the thin layer of LiF, and essentially proved that the modifications to the spectra are due the formation of the Alq radical anion. It can be concluded that when Al, LiF and Alq are all present, that Li is liberated and reacts with Alq to form the radical anion [239,241]. The beneficial effects on reactive metal deposition can be achieved without actually employing the metals themselves.

In Fig. 6.9(a) and (b), the UPS spectra are presented by Ding and Gao for Au depositions onto Alq with a 5 \AA LiF buffer layer [483]. The presence of the thin LiF layer on the Alq surface preserve most of the valence features, although it does induce a 0.14 eV shift toward higher binding energy and some broadening. The deposition of Au initially produces a slight shift of the HOMO position to higher BE, reaching a maximum of 0.26 eV at gold coverage $\Theta_{\text{Au}} = 0.5 \text{ \AA}$. Further Au deposition gradually reverses the shift toward lower BE. The final Alq HOMO position, however, cannot be observed from the valence spectra since the Au features dominate after $\Theta_{\text{Au}} = 4 \text{ \AA}$. Shown in Fig. 6.9(a) are the low-energy secondary cutoff regions of the UPS spectra. The vacuum level shifts of 0.15 eV toward lower energy, as reflected in the cutoff spectra, when LiF is deposited. The existence of an interface dipole can be ruled out since the HOMO in Fig. 6.9(b) show the same shift at this stage, reflecting vacuum level alignment. For the initial Au deposition ($\Theta_{\text{Au}} \leq 0.5 \text{ \AA}$), the vacuum level shift is consistent with that of the valence features in Fig. 6.9(b), indicating the nature of rigid shift for the lower coverages. As the Au overlayer grows thicker, the vacuum level shifts upward toward that of pure Au, but saturates at $\Theta_{\text{Au}} = 8 \text{ \AA}$ at a position of 1.1 eV below that of pure Au, whose workfunction is 5.3 eV [511]. This phenomenon has been observed in other Au deposition on organic systems, and can be attributed to Au intermixing with and clustering in the substrate material [170].

It is very intriguing to compare the valence energy level evolution of the Au/LiF/Alq interface with that of Al/LiF/Alq, reproduced here in Fig. 6.9(c). For both interfaces, the molecular orbital structure of Alq is preserved with LiF present. It is less of a surprise for the Au case than for Al, since the latter would induce significant chemical reaction with Alq if LiF was not present [239]. As seen in Fig. 6.9(a) and (b), Au induces little energy level shift, and leaving a “flat-band” in Alq in the interface region. As a result, the electron injection barrier is unaltered compared to that of pristine Alq. The situation is dramatically different in the case of Al/LiF/Alq, as can be seen in Fig. 6.9(c), where the deposition of Al on 5 \AA LiF/Alq shifts the Alq HOMO to the higher BE by as much as 1.0 eV. Within the rigid shift assumption, the LUMO is also lowered by the same amount, resulting a significant reduction of electron injection barrier that can lead to substantial improvement in electron injection as observed in devices. Such improvement can be attributed to doping by Li released through the interface

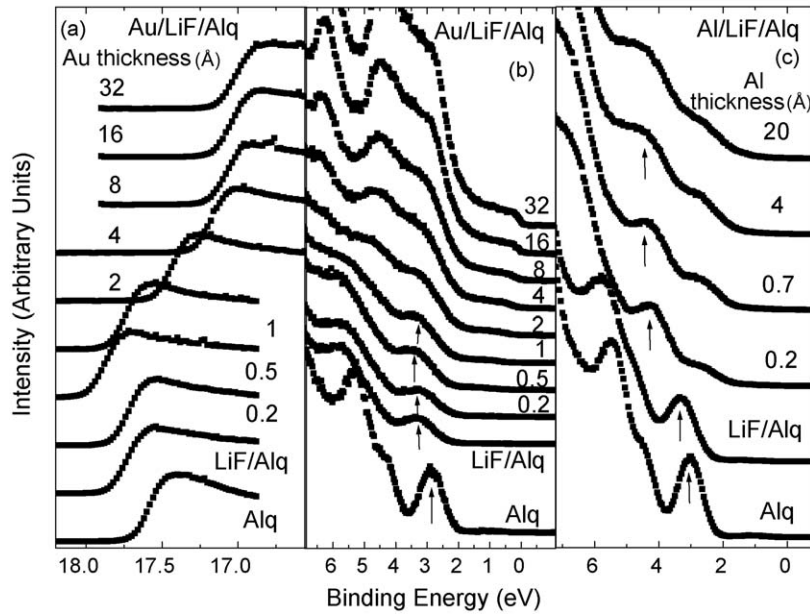


Fig. 6.9. Evolution of the cutoff (a) and the HOMO region (b) of the UPS spectra as a function of Au thickness for Au/LiF/Alq. (c) Evolution of the HOMO region as a function of Al thickness for Al/LiF/Alq (from Ref. [483]).

reaction by Al deposition. The assessment of doping is also supported by the gap state and new N 1s component. More direct evidence of the existence of Li⁺ in such a system has been demonstrated by Wu et al. with synchrotron radiation photoemission spectroscopy, where the high photon flux allows direct observation of Li 1s [566]. For the case of Au/LiF/Alq, the lack of doping is further supported by the fact that neither the gap state nor the extra N 1s component could be observed [483].

7. Structural, electronic, and electrical studies on ordered systems

In most of the thin organic devices, the organic films are either amorphous or polycrystalline. There inevitably exist structural and chemical defects that may hinder the investigation of the physical properties at the interfaces such as the molecular ordering, interface bonding, electron-phonon coupling, and their effects on the electrical and optical characteristics. Hetero-epitaxial growth of organic films has been demonstrated possible, which allows more detailed studies of the properties of the organic materials and

the interface formation of these materials [38,84,117,125,139, 158,201,203,208,225,284,488,556,567–581]. Over the past years researchers have tried a number of substrates that might be suitable for epitaxial growth. Forrest et al. and Umbach et al. succeeded in fabricating quasi-epitaxial layers of PTCDA, one of the most favorable and intensely studied molecules used in getting highly ordered organic films, on gold [582], silver [583], and nickel substrates, respectively [569]. In their study of the fundamentals of quasi-epitaxy of PTCDA, Kendrick and Kahn observed that this planar molecule reveals all of three possible growth modes mentioned at the outset of this section when deposited on Se-passivated GaAs (1 0 0) (2 × 1), graphite, and InAs (0 0 1) (4 × 2) substrates respectively [584].

Umbach and his coworkers found that when organic molecules are deposited by vacuum sublimation on ordered substrates, highly ordered organic superstructures may form, and the superstructure can be commensurate to the substrate if covalent and nondissociative bond occurs [98,225,284,567–569,585–594]. Shown in Fig. 7.1 are (a) the STM picture and (b) real space model for PTCDA on Ag(1 1 1) [569]. Each molecule is represented by ten

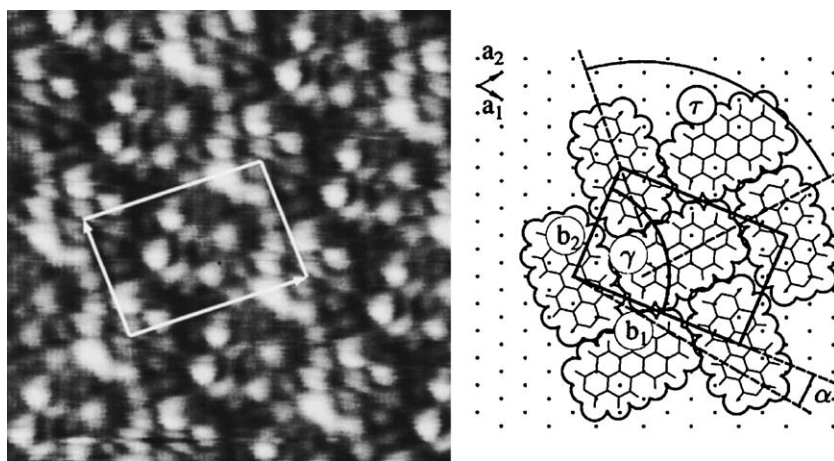


Fig. 7.1. (a) STM picture and (b) real space model for PTCDA on Ag(1 1 1). The intramolecular STM structure is identical to the symmetry of the LUMO of the free molecule (from Ref. [569]).

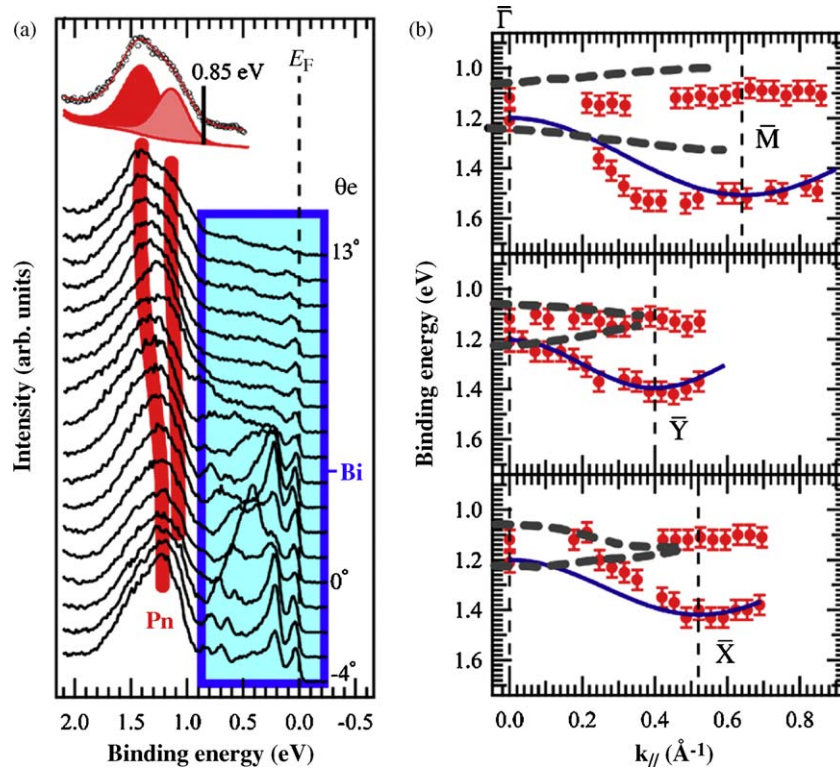


Fig. 7.2. (a) ARPES spectra of 1 ML pentacene on Bi(0 0 1) measured at 140 K along the $\bar{\Gamma} - \bar{Y}$ direction. (b) Band dispersions of the two HOMO-derived bands of the 1 ML pentacene film adsorbed on Bi((0 0 1)) (from Ref. [596]).

current maxima, four of which are slightly more intense. From the orientation of these intense maxima, as well as from the size of the unit cell, one can derive that the unit cell contains two molecules, which are rotated by nearly 90° with respect to each other. The corresponding real-space model is in agreement with all data (NEXAFS, LEED, STM) [569]. The intramolecular STM structure in Fig. 7.1 is identical to the symmetry of the LUMO of the free molecule as derived from calculations by Jung et al. [595].

Kakuta et al. reported the energy dispersions of the highest occupied molecular orbitals (HOMO)-derived bands of pentacene thin film on Bi(0 0 1), obtained with ARPES [596]. The ARPES spectra of the 1ML pentacene film adsorbed on Bi(0 0 1) measured along the $\bar{\Gamma} - \bar{Y}$ direction at 140 K are shown in Fig. 7.2(a). Of the structures observed in the spectra, the intensities of those between $E_B = 0$ and 0.9 eV originate from the Bi(0 0 1) substrate. The structures observed between $E_B = 1.0$ and 1.8 eV are identified as from pentacene HOMO and HOMO-1. The overall dispersions of the HOMO derived bands along the $\bar{\Gamma} - \bar{X}$, $\bar{\Gamma} - \bar{Y}$, and $\bar{\Gamma} - \bar{M}$ are shown in Fig. 7.2(b). The dashed curves shown in Fig. 7.2(b) are the theoretical dispersions of the HOMO-derived bands of the low-density bulk pentacene phase reported in Ref. [597]. Solid curves are the dispersion obtained by analyzing the HOMO-derived band using a simple tight-binding model. The photoemission result indicates that the overlap of the π -orbitals of adjacent pentacene molecules is larger than what was expected from theoretical calculations. Further, of the two HOMO-derived bands, the large dispersion width of the band with higher binding energy suggests that this one mainly contributes to the band like charge transport in a pentacene crystal [596].

Although an isolated individual molecule clearly has only one ionization potential, multiple values are found for molecules in ordered assemblies. Koch et al. used photoelectron spectroscopy to investigated ordered π -conjugated organic compounds α -sexithiophene (6T) and α , ω -dihexyl-sexithiophene (DH6T) on Ag(1 1 1) in combination with first-principles calculations and

electrostatic modeling reveal the existence of a surface dipole built into molecular layers [158]. Conceptually different from the surface dipole at metal surfaces, its origin lies in details of the molecular electronic structure and its magnitude depends on the orientation of molecules relative to the surface of an ordered assembly. Suitable pre-patterning of substrates to induce specific molecular orientations in subsequently grown films thus permits adjusting the ionization potential of one molecular species over up to 0.6 eV via control over monolayer morphology. Shown in Fig. 7.3 are (a) the energy-level diagram for the lying-6T/lying-DH6T-monolayer/Ag(1 1 1) structure, and (b) energy-level diagram for the standing-6T/standing-DH6T/lying-DH6T-monolayer/Ag(1 1 1) structure. The intrinsic surface dipole due to the π -electron clouds over the molecular planes in the lying layer(s) is highlighted. The work function of the pristine Ag(1 1 1) surface (=4.4 eV) as well as the interface dipole (=0.7 eV) are also shown [158].

Surface analytical tools can also be used to examine the idealized devices based on organic single crystal layers. Frisbee and his coworkers have applied AFM with conductive tip to investigate OTFTs with single crystal domains and observed electric potential variations at the interfaces and grain boundaries that can be correlated to charge injection and trapping [339,598–603]. The potential profile across the channel of an operating sexithiophene-based field-effect transistor (FET) was investigated using an atomic force microscope with a conducting probe. A high impedance electrometer recorded the probe potential when it was placed in contact at fixed points with the channel surface. A scheme depicting the potentiometry experiment is shown in Fig. 7.4(a) [603]. The potential sensing tip was a conventional tapping mode Si cantilever coated with Cr/Au \sim 70/750 Å. The topography of the FET structure was imaged in tapping mode before and after each individual measurement using the same metal-coated tip in order to verify that no damage to the device had occurred. Fig. 7.4(b) shows potential profiles as a function of the drain voltage, for zero applied gate voltage V_G [603]. Each profile was obtained along the

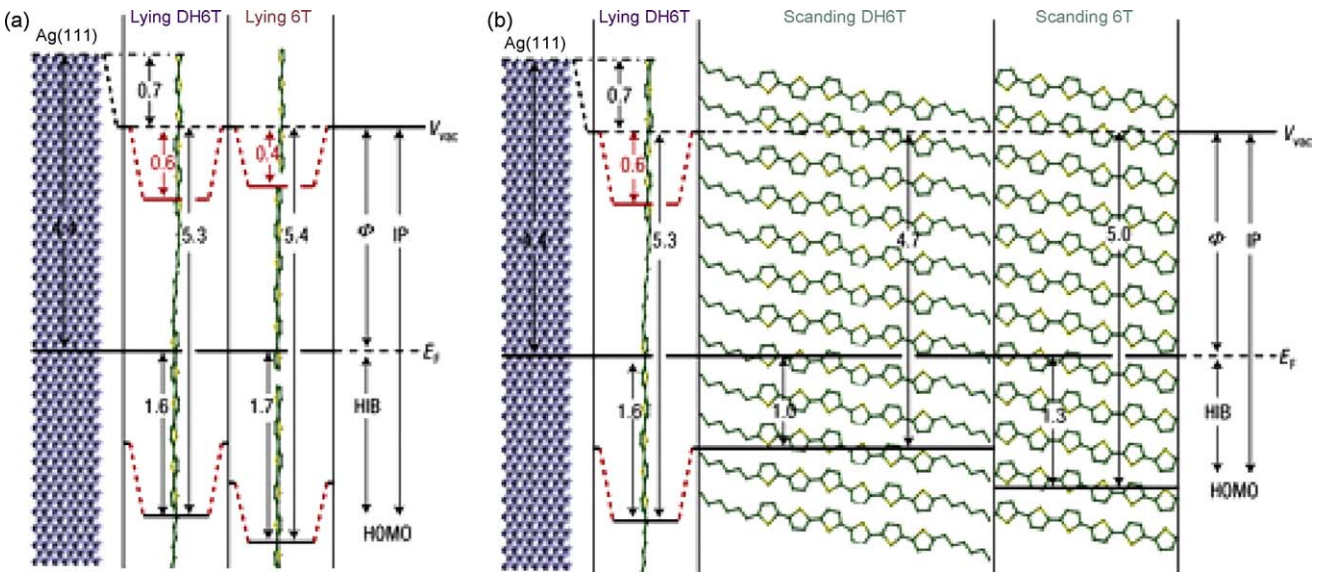


Fig. 7.3. Energy-level diagram for (a) lying-6T/lying-DH6T-monolayer/Ag(111), (b) standing-6T/standing-DH6T/lying-DH6T-monolayer/Ag(111) structure (from Ref. [158]).

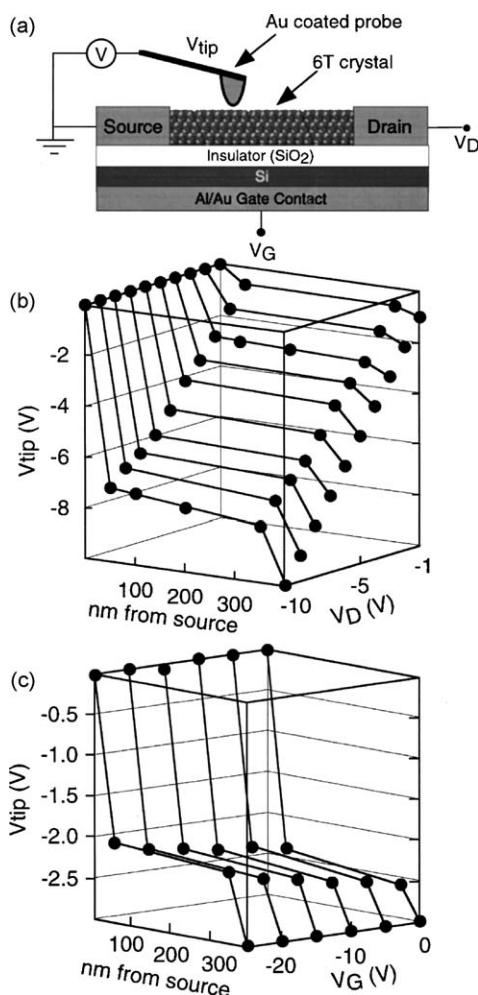


Fig. 7.4. (a) Scheme of the AFM potentiometry experiment. (b) Potential profiles as a function of distance from the source electrode, for different drain biases V_D with $V_G = 0$ V. (c) Potential profiles for varying gate biases. The drain bias V_D was kept at 23 V (from Ref. [603]).

same straight-line path between the two Au electrodes. On the Fig. 7.4(b) plot, distance is measured relative to the source electrode. It is evident from the figure that a significant voltage drop occurs at the Au–6T contacts, irrespective of the bias across the device. Fig. 7.4(c) shows potential profiles at fixed V_D (23 V) as a function of V_G [603]. Again, at each value of V_G , the majority of the 3 V applied to the drain is dropped at the source and drain contacts. The potential profiles in Fig. 7.4 clearly indicate that the FET is contact limited. Moreover, the potential drop was not fixed but depended on the applied drain and gate voltages. This study demonstrates the utility of AFM and potential profiling for identifying high resistance bottlenecks to charge transport in organic-based devices [603].

Ordered organic films can grow without registry to the substrates, or even on amorphous ones. In these cases, only polycrystalline samples with various domain sizes can be expected. Shown in top panel of Fig. 7.5 are some representative tapping mode AFM images of pentacene thin films evaporated on SiO_2 substrate by Zorba *et al.* [604]. It can be observed, for the initial stages of the growth, that the number and size of the mounds increase with growth time. This increase stops once the individual islands become large enough to touch each other. However, new monolayers start nucleating a good deal without waiting the underlying monolayer(s) to fully form. This could be seen in the top panel of Fig. 7.5. A closer look at the AFM images of the pentacene film in Fig. 7.5 reveals that the ordered growth of pentacene is really a very peculiar one that incorporates a number of different growth mechanisms, not just fractal growth as caused by diffusion limited aggregation (DLA) mechanism. It can be seen from the top panel of Fig. 7.5 that pentacene forms a mixture of both regular and irregular-sized mounds on SiO_2 surface. In addition, one can readily observe the monolayer structures forming pyramidlike mounds. In fact, the average step size of the monolayers was found to be 15.8 Å, which matches closely with the length of a pentacene molecule [605]. Moreover, these terraced mounds are in a shape that bespeaks fat-DLA growth. DLA forms via diffusion of molecules through pure random walk and their sticking to a cluster to create irregularly branched and chaotic patterns. Fat DLA forms when the particles are allowed to diffuse on the boundary of the cluster to increase the number of nearest neighbors [606]. Indeed, the fractal dimension analysis of Fig. 7.5 revealed a

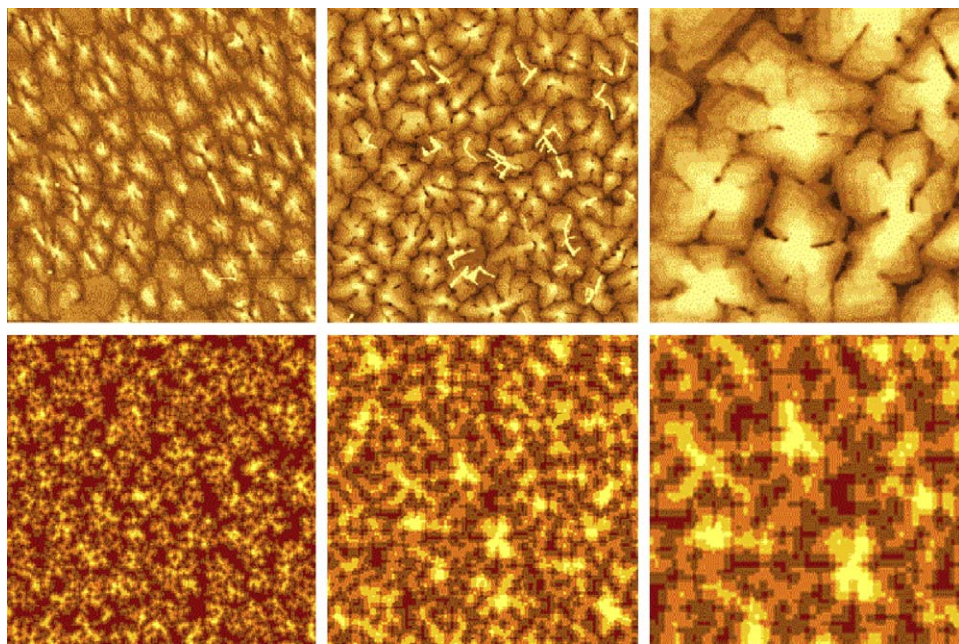


Fig. 7.5. Top panel: some representative surface morphologies of pentacene scanned by tapping mode AFM with (a) 20 Å and (b) 50 Å pentacene ($5 \times 5 \mu\text{m}^2$). (c) Area zoomed in (b). Bottom panel: Monte Carlo simulation results (from Ref. [604]).

dimension of about 1.6, which agrees very closely with that of a DLA surface [21]. What one has as the dominant growth mechanisms behind pentacene's growth seems to be an interplay between the DLA-type growth and mound growth [604].

Bottom panel of Fig. 7.5 shows Monte Carlo simulation results [604]. To the eye, the real morphology data and the simulation morphology data resemble each other closely. In fact, one can easily distinguish the DLA-type formation in the initial coverages (lower panel Fig. 7.5(c)). With more particles landing, due to the uphill diffusion bias driven by the Schwoebel barrier effect, newer DLA-type monolayers formed on top of existing ones in a much faster fashion. As a result, as can be seen in the simulation figures, a novel morphology was generated that closely mimics that of pentacene. In both sets of data individual monolayer terraces can easily be identified. DLA with dendritic patterns can also be seen.

The ordered growth of pentacene on Si has been investigated by Heringdorf et al. using photoelectron emission microscopy (PEEM), with a resolution of 125 nm limited by the pixel resolution of the video camera [397]. In the PEEM images, contrast between pentacene in the first few molecular layers arises from differences in electronic structure. The 1st molecular layer appears bright on a dark Si surface (Fig. 7.6(a)). In Fig. 7.6(b), the 2nd molecular layer appears dark on the 1st layer, and in Fig. 7.6(c) the 3rd layer appears darker still [397]. With increasing film thickness, contrast

disappears as the electronic properties of the surface layer approach those of the bulk. During the initial stages of growth, stable two-dimensional islands nucleate on the surface. The nucleation density depends on the deposition rate and on the preparation of the substrate. Whereas the nucleation density on clean silicon surfaces is of the order of $10^{-3} \mu\text{m}^{-2}$, it can easily be 100 times larger on SiO_2 [397].

Near-edge X-ray absorption fine structure has been used extensively on the orientation, lateral order, interface bonding, and electronic structure of organic layers [202,225,279,284,325,367, 569,579,607–611]. Shown in Fig. 7.7 are the C 1s NEXAFS spectra for PTCDA on $\text{Ag}(1\ 1\ 1)$ and $\text{Ni}(1\ 1\ 1)$ with different incident angles by Umbach et al. [569]. Dash lines mark the three most prominent π resonances of the multilayer spectra. The δ spectra of the submonolayers are omitted since they look very similar to those of the multilayers. Comparison between the submonolayer and the multilayer spectra taken at 70° reveals that significant changes occur in the fine structure when the molecules are adsorbed directly on the substrate. These changes indicate that the LUMO is strongly involved in the bonding to the surface. A detailed analysis reveals that the molecules are oriented parallel to the surface in the monolayer, derived from the nearly complete disappearance of these resonances when normal (0°) instead of grazing (70°) incidence is used [569].

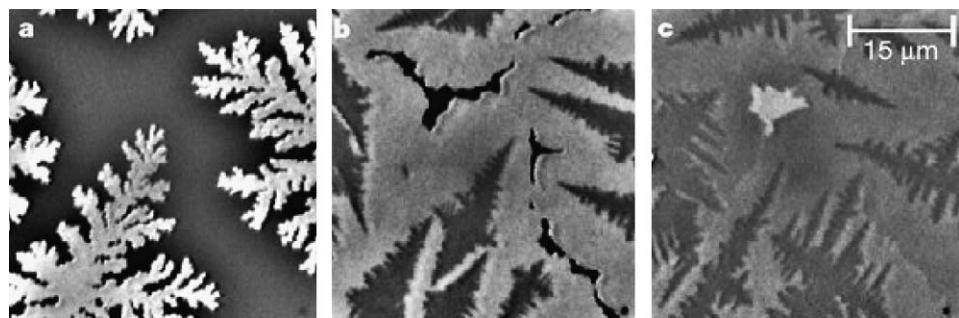


Fig. 7.6. PEEM picture of pentacene on SiO_2 with (a) one (b) two (c) three layers (from Ref. [397]).

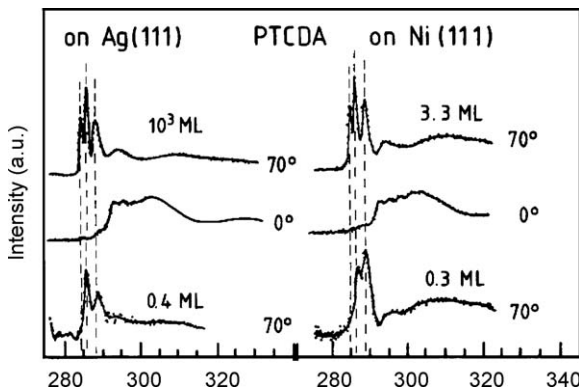


Fig. 7.7. The C 1s NEXAFS spectra for PTCDA on Ag(111) and Ni(111) with different incident angles (from Ref. [569]).

8. Possible damage by surface analytical probes

Extensive studies using surface analytical tools on organic materials have generated important information on the electronic structures and interface properties. However, these probes also may cause degradation of the materials [100,234,468,612,613]. The damage always depends on the energy quanta and dosage. For example, XPS is more detrimental than UPS if the same number of photons is involved, and a monochromatized XPS source is less damaging than a non-monochromatized one. It also depends on the interaction of the probe with the organic materials. As electrons interact strongly with a solid film, characterized by the mean free path typically orders of magnitude less than that of the photons of similar energy, IPES is much more damaging than PES. Generally, one should observe the spectral change as the measurement progresses, and determines within what dosage the spectrum is still reliable. For PES, spectral shift occurs much sooner than spectral shape change, indicating charging of the organic thin films. Very small current must be used for STM because of the low conductivity of the OSCs. In AFM, one uses typically the tapping mode to avoid alternating the surface of the soft organic materials.

Fig. 8.1 shows the evolution of 4PV valence band spectra taken by Choong et al. with a 21.2 eV He I UV source as a function of UV exposure time t [348]. The highest occupied molecular orbital (HOMO) feature, which was attributed to the delocalized π orbitals of the vinylene groups, starts at about binding energy 1.9 eV and peaks at 2.8 eV, with respect to the Fermi level. The Fermi level was obtained by evaporating a metal on the organic layer and locating the Fermi edge. The peak observed at about 4.3 eV is due to the π orbitals localized in the phenylene rings. As the exposure times increased, two distinct changes are observed. First, the 2.8 eV HOMO feature observed in the $t = 0$ spectrum started to disappear, indicating the destruction of the vinylene bonds. Second, the 4.3 eV feature is seen to shift to higher binding energies, up to the $t = 10$ min spectrum, before stabilizing at roughly 4.5 eV. Although the position of this feature has shifted, the peak shape is largely unaffected [16], indicating that the phenylene π orbitals are not affected by the UV radiation. The inset shows the evolution of XPS C 1s peak obtained for 4PV as a function of X-ray exposure time. No discernible changes were observed in the peak shape and position up to $t = 16$ min. On the other hand, UV exposure quenches PL very effectively, and results in a total quenching of PL in 30 minutes. It shows that the damage to the molecular species are much more sensitively probed by luminescence measurements, as excitons are quickly quenched by the newly created defects [348].

As described in Section 3, metal deposition also produces extensive PL quenching (see Fig. 3.15). It is interesting to compare

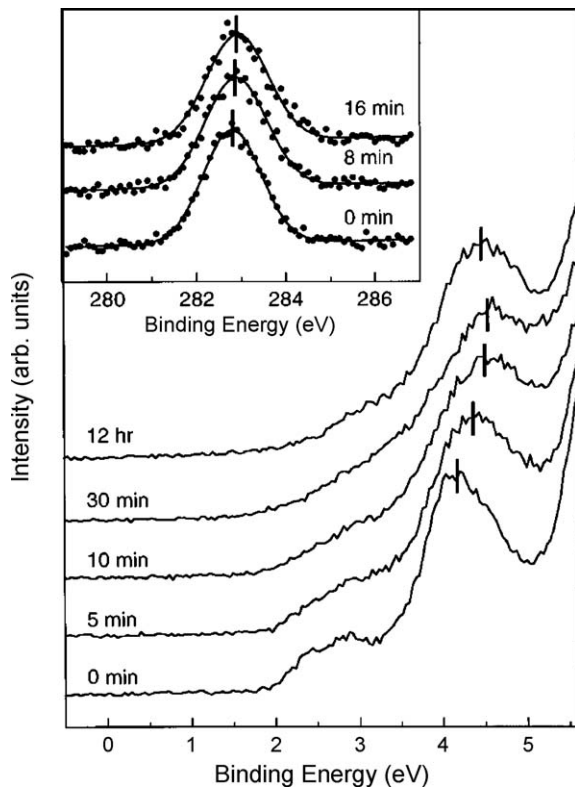


Fig. 8.1. Evolution of UPS spectra for 4PV as a function of UV exposure time t . The inset shows no discernible changes in the position and shape of the XPS C 1s (from Ref. [348]).

the modification of the electronic structure of 4PV due to UV radiation and metal quenching processes. A portion of a 4PV/ITO film was illuminated with the UV radiation for 35 min, after which, 5 Å of Ca was deposited on the entire film. UPS measurements were then performed at various exposure times up to $t = 30$ min for both the dead (UV exposed) spot, and a fresh (not exposed) spot. The UPS spectra of the valence region of both the dead and fresh spots, taken at $t = 30$ min, are shown in Fig. 8.2 [348]. Due to Ca-induced changes in the valence electronic structure, the feature attributed to the phenylene ring has moved to higher binding energy by about

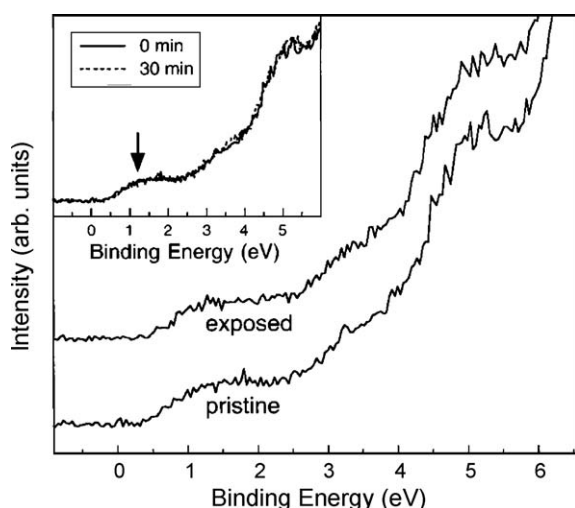


Fig. 8.2. The UPS spectra of a Ca/4PV/ITO sample for both the dead and fresh spots, taken at $t = 30$ min. The inset shows the UPS spectra for the fresh spot taken at $t = 0$ and 30 min (from Ref. [348]).

1.1 eV. No discernible differences were seen between the spectra of the fresh and dead spots. The inset of Fig. 8.2 shows the valence band spectra for the fresh spot for $t = 0$ and 30 min. Again no discernible differences were seen between the two. The results indicate that the metal induced changes dominates the valence electronic structure and masks the radiation induced ones.

9. Final remarks

In this review I have examined contributions to the understanding of interfaces in organic semiconductors by using surface analytical techniques. It means to illustrate that the electronic and structural properties of the organic materials and their interfaces are the key to the understanding of their characteristics in devices. Surface and interface analytical investigations have generated critical insight of the fundamental processes at interfaces involving organic semiconductors. It is established through these investigations that the interface energy level alignment between metal–organic interfaces depends on the formation of interface dipole instead of a common vacuum level. Furthermore, surface analytical studies have provided insight on the detailed interface interactions including charge transfer, chemical reaction, intermixing, diffusion, and cluster formation. The insight thus generated can be useful for the improvement of the performance of organic semiconductor devices through better understanding of the basic mechanisms, and through engineering of the interfaces and device structures. It should also be mentioned that although the investigations are quite extensive, a large number of questions remain open for interface processes in OSC devices, including the kinetic requirements and the role of interface polarizability, exciton transport rates, interfacial electronic states, the crucial process of interfacial charge-carrier recombination, the relationship of charge transfer across and exciton transport toward the interface, etc. Future efforts are needed to integrate the findings from the surface analytical studies and the performance of the OSC devices. In that regard, the effects of the conditions in typical device fabrication should be considered such as poorer vacuum in comparison to the UHV typical for surface analysis. It is also indispensable to investigate well-controlled systems such as crystalline or epitaxial systems, and use these idealized systems to understand the underlining basic mechanisms. One may expect that more systematic studies on the interfaces and more tools that probe the electronic structure of materials will be applied in the future, and a more complete picture of the interface formation in organic semiconductor devices can be expected to emerge as a result.

Acknowledgment

The work is support in part by NSF DMR-0602870.

References

- [1] C.W. Tang, S.A. VanSlyke, *Appl. Phys. Lett.* 51 (1987) 183–185.
- [2] G. Horowitz, *Adv. Mater.* 10 (1998) 365.
- [3] A. Hagfeldt, M. Gratzel, *Acc. Chem. Res.* 33 (2000) 269.
- [4] W.R. Salaneck, S. Stafstrom, J.-L. Bredas, *Conjugated Polymer Surfaces and Interfaces*, Cambridge University Press, New York, 1996.
- [5] Y.L. Gao, *Acc. Chem. Res.* 32 (1999) 247–255.
- [6] H. Ishii, K. Sugiyama, E. Ito, K. Seki, *Adv. Mater.* 11 (1999) 605.
- [7] N. Koch, *J. Phys. Cond. Matter.* 20 (2008) 184008.
- [8] N. Ueno, S. Kera, *Prog. Surf. Sci.* 83 (2008) 490–557.
- [9] S. Braun, W.R. Salaneck, M. Fahlman, *Adv. Mater.* 21 (2009) 1450.
- [10] J. Hwang, A. Wan, A. Kahn, *Mater. Sci. Eng. R-Rep.* 64 (2009) 1–31.
- [11] W. Shockley, *Phys. Rev.* 56 (1939) 317.
- [12] N.W. Ashcroft, N.D. Mermin, *Solid State Physics*, Harcourt, New York, 1976.
- [13] E.A. Silinsh, V. Capek, *Organic Molecular Crystals*, AIP, New York, 1994.
- [14] M. Fahlman, J.L. Bredas, W.R. Salaneck, *Synth. Metals* 78 (1996) 237–246.
- [15] R.C. Weast, M.J. Astle, W.H. Beyer (Eds.), *CRC Handbook of Chemistry and Physics*, CRC Boca Raton, 1985.
- [16] X.Y. Zhu, *Surf. Sci. Rep.* 56 (2004) 1–83.
- [17] W. Schottky, R. Stormer, F. Waibel, *Z. Hochfrequenztechnik* 37 (1931) 62.
- [18] S.M. Sze, *Physics of Semiconductor Devices*, Wiley, New York, 1981.
- [19] C. Kittel, H. Kroemer, *Thermal Physics*, Freeman, New York, 1980.
- [20] B.A. Gregg, M.C. Hanna, *J. Appl. Phys.* 93 (2003) 3605–3614.
- [21] A.-L. Barabasi, H.E. Stanley, *Fractals Concepts in Surface Growth* Cambridge, New York, 1995.
- [22] R. L. Park, M. G. Lagally (Eds.), *Solid State Physics: Surfaces*, Academic Press, Orlando, 1985.
- [23] D.P. Woodruff, T.A. Delchar, *Modern Techniques of Surface Science*, Cambridge University Press, New York, 1986.
- [24] J.C. Rivière, *Surface Analytical Techniques*, Clarendon Press, New York, 1990.
- [25] W. Neagle, D.R. Randell, (Eds.), *Surface analysis techniques and applications*/ edited by Cambridge, New York, 1990.
- [26] S. Hüfner, *Photoelectron Spectroscopy: Principles and Applications*, Springer-Verlag, New York, 2003.
- [27] L.J. Brillson (Ed.) *Handbook on Semiconductors*, New York, Elsevier Science Publishers, New York, 1992.
- [28] A. Einstein, *Annalen der Physik* 17 (1905) 132–148.
- [29] M.P. Seah, W.A. Dench, *Surf. Interf. Anal.* 1 (1979) 2.
- [30] W.R. Salaneck, K. Seki, A. Kahn, J.J. Pireaux (Eds.), *Conjugated Polymer and Molecular Interfaces: Science and Technology for Photonic and Optoelectronic Applications*, Marcel Dekker, New York, 2001.
- [31] Y. Gao, *Interface electronic structure and organic photovoltaic devices*, in: S. Sun, N. Sariciftci (Eds.), *Organic Photovoltaics*, Taylor and Francis, New York, 2004.
- [32] U. Gelius, *Phys. Scr.* 9 (1974) 133.
- [33] K.E. Smith, S.D. Kevan, *Prog. Solid State Chem.* 21 (1991) 49–131.
- [34] A. Damascelli, Z. Hussain, Z.X. Shen, *Rev. Modern Phys.* 75 (2003) 473–541.
- [35] W.A. Harrison, *Electronic Structure and the Properties of Solids*, Dover, New York, 1989.
- [36] Y. Hirose, W. Chen, E.I. Haskal, S.R. Forrest, A. Kahn, *Appl. Phys. Lett.* 64 (1994) 3482–3484.
- [37] K. Seki, H. Ishii, *J. Elect. Spectrosc. Related Phen.* 88 (1998) 821–830.
- [38] H. Ishii, E. Morikawa, S.J. Tang, D. Yoshimura, E. Ito, K. Okudaira, T. Miyamae, S. Hasegawa, P.T. Sprunger, N. Ueno, K. Seki, V. Saile, *J. Elect. Spectrosc. Related Phen.* 103 (1999) 559–564.
- [39] I.G. Hill, A.J. Mäkinen, Z.H. Kafafi, *J. Appl. Phys.* 88 (2000) 889–895.
- [40] P.G. Schroeder, C.B. France, B.A. Parkinson, R. Schlaf, *J. Appl. Phys.* 91 (2002) 9095–9107.
- [41] M. Knupfer, H. Peisert, *Phys. Status Solidi Appl. Res.* 201 (2004) 1055–1074.
- [42] F. Amy, C. Chan, A. Kahn, *Org. Electron.* 6 (2005) 85–91.
- [43] T. Munakata, T. Sugiyama, Y. Sonoda, *Surf. Sci.* 593 (2005) 38–42.
- [44] L. Zhang, H. Peisert, I. Biswas, M. Knupfer, D. Batchelor, T. Chasse, *Surf. Sci.* 596 (2005) 98–107.
- [45] S. Ryu, J. Chang, H. Kwon, S.K. Kim, *J. Vac. Sci. Technol. A* 24 (2006) 1454–1459.
- [46] L. Gundlach, R. Ernstorfer, F. Willig, *Prog. Surf. Sci.* 82 (2007) 355–377.
- [47] L. Gundlach, R. Ernstorfer, F. Willig, *Appl. Phys. A Mater. Sci. Process.* 88 (2007) 481–495.
- [48] T.W. Pi, T.C. Yu, *Surf. Rev. Lett.* 14 (2007) 377–385.
- [49] H.J. Ding, Y.L. Gao, M. Cinchetti, J.P. Wustenberg, M. Sanchez-Albaneda, O. Andreiev, M. Bauer, M. Aeschlimann, *Phys. Rev. B* 78 (2008) 075311.
- [50] K. Hong, J.W. Lee, S.Y. Yang, K. Shin, H. Jeon, S.H. Kim, C. Yang, C.E. Park, *Org. Electron.* 9 (2008) 21–29.
- [51] H. Peisert, A. Petershans, T. Chasse, *J. Phys. Chem. C* 112 (2008) 5703–5706.
- [52] A. Ruocco, F. Evangelista, R. Gotter, A. Attili, G. Stefani, *J. Phys. Chem. C* 112 (2008) 2016–2025.
- [53] N.V. Smith, D.P. Woodruff, *Prog. Surf. Sci.* 21 (1986) 295–370.
- [54] G. Borstel, G. Thorner, *Surf. Sci. Rep.* 8 (1988) 1–41.
- [55] N.V. Smith, *Rep. Prog. Phys.* 51 (1988) 1227–1294.
- [56] F.J. Himpsel, *Surf. Sci. Rep.* 12 (1990) 1–48.
- [57] P.D. Johnson, S.L. Hulbert, *Rev. Sci. Instrum.* 61 (1990) 2277–2288.
- [58] J.A. Stroscio, W.J. Kaiser, *Scanning Tunneling Microscopy*, Academic Press, San Diego, 1993.
- [59] R. Howland, L. Benatar, *A Practical Guide to Scanning Probe Microscopy*, Park Scientific Instruments, Sunnyvale, 1993.
- [60] S. Zorba, *Morphological and electrical studies of organic semiconductor thin films*, in: *Physics and Astronomy*, vol. Doctor of Philosophy, University of Rochester, Rochester, 2004, p. 120.
- [61] J. Stöhr, *NEXAFS Spectroscopy*, Springer-Verlag, New York, 1992.
- [62] L. Kelvin, *Philos. Mag.* 46 (1898) 82.
- [63] E.O. Kane, *Phys. Rev.* 127 (1962) 131.
- [64] M. Pope, C.E. Swenberg, *Electronic Processes in Organic Crystals and Polymers*, Oxford, New York, 1999.
- [65] V.V. Afanas'ev, *Internal Photoemission Spectroscopy: Principles and Applications*, Elsevier, New York, 2007.
- [66] R.K. Willadson, A.C. Beer (Eds.), *Injection Phenomena*, Academic, New York, 1970.
- [67] Y. Harada, S. Masuda, H. Ozaki, *Chem. Rev.* 97 (1997) 1897.
- [68] V. Cermak, *J. Chem. Phys.* 44 (1966) 3781.
- [69] J.J. Thomson, *Phil. Mag.* 20 (1910) 752–767.
- [70] A. Benninghoven, F.G. Rüdenauer, H.W. Werner, *Secondary Ion Mass Spectrometry: Basic Concepts, Instrumental Aspects, Applications and Trends*, Wiley, New York, 1987.
- [71] E.W. Forsythe, Y. Gao, *Interfaces in organic light emitting devices*, in: H.S. Nalwa (Ed.), *Handbook of Surfaces and Interfaces of Materials*, vol. 1, Academic Press, New York, 2001.
- [72] Y. Harima, T. Kodaka, H. Okazaki, Y. Kunugi, K. Yamashita, H. Ishii, K. Seki, *Chem. Phys. Lett.* 240 (1995) 345–350.

- [73] K. Seki, T. Tani, H. Ishii, *Thin Solid Films* 273 (1996) 20–26.
- [74] H. Ishii, S. Hasegawa, D. Yoshimura, K. Sugiyama, S. Narioka, M. Sei, Y. Ouchi, K. Seki, Y. Harima, K. Yamasaki, *Mol. Cryst. Liq. Cryst. Sci. Technol. Sect. A-Mol. Cryst. Liquid Cryst.* 296 (1997) 427–444.
- [75] H. Ishii, K. Seki, *IEEE Trans. Electr. Dev.* 44 (1997) 1295–1301.
- [76] H. Ishii, D. Yoshimura, K. Sugiyama, S. Narioka, Y. Hamatani, I. Kawamoto, T. Miyazaki, Y. Ouchi, K. Seki, *Synth. Metals* 85 (1997) 1389–1390.
- [77] K. Seki, E. Ito, H. Ishii, *Synth. Metals* 91 (1997) 137–142.
- [78] K. Sugiyama, D. Yoshimura, E. Ito, T. Miyazaki, Y. Hamatani, I. Kawamoto, H. Ishii, Y. Ouchi, K. Seki, *Synth. Metals* 86 (1997) 2425–2426.
- [79] D. Yoshimura, H. Ishii, S. Narioka, M. Sei, T. Miyazaki, Y. Ouchi, S. Hasegawa, Y. Harima, K. Yamashita, K. Seki, *Synth. Metals* 86 (1997) 2399–2400.
- [80] H. Ishii, K. Sugiyama, D. Yoshimura, E. Ito, Y. Ouchi, K. Seki, *IEEE J. Selected Top. Quant. Electron.* 4 (1998) 24–33.
- [81] K. Sugiyama, D. Yoshimura, T. Miyamae, T. Miyazaki, H. Ishii, Y. Ouchi, K. Seki, *J. Appl. Phys.* 83 (1998) 4928–4938.
- [82] E. Ito, H. Oji, M. Furuta, H. Ishii, K. Oichi, Y. Ouchi, K. Seki, *Synth. Metals* 101 (1999) 654–655.
- [83] H. Oji, E. Ito, M. Furuta, K. Kajikawa, H. Ishii, Y. Ouchi, K. Seki, *J. Electr. Spectrosc. Related Phen.* 103 (1999) 517–521.
- [84] D. Yoshimura, H. Ishii, Y. Ouchi, E. Ito, T. Miyamae, S. Hasegawa, K.K. Okudaira, N. Ueno, K. Seki, *Phys. Rev. B* 60 (1999) 9046–9060.
- [85] D. Yoshimura, T. Yokoyama, E. Ito, H. Ishii, Y. Ouchi, S. Hasegawa, K. Seki, *Synth. Metals* 102 (1999) 1145–1146.
- [86] H. Ishii, H. Oji, E. Ito, N. Hayashi, D. Yoshimura, K. Seki, *J. Lumin.* 87–89 (2000) 61–65.
- [87] K. Sugiyama, H. Ishii, Y. Ouchi, K. Seki, *J. Appl. Phys.* 87 (2000) 295–298.
- [88] E. Ito, H. Oji, N. Hayashi, H. Ishii, Y. Ouchi, K. Seki, *Appl. Surf. Sci.* 175 (2001) 407–411.
- [89] K. Seki, N. Hayashi, H. Oji, E. Ito, Y. Ouchi, H. Ishii, *Thin Solid Films* 393 (2001) 298–303.
- [90] K. Seki, E. Ito, H. Oji, D. Yoshimura, N. Hayashi, Y. Sakurai, Y. Hosoi, T. Yokoyama, T. Imai, Y. Ouchi, H. Ishii, *Synth. Metals* 119 (2001) 19–24.
- [91] N. Hayashi, H. Ishii, Y. Ouchi, K. Seki, *J. Appl. Phys.* 92 (2002) 3784–3793.
- [92] E. Ito, Y. Washizu, N. Hayashi, H. Ishii, N. Matsuike, K. Tsuboi, Y. Ouchi, Y. Harima, K. Yamashita, K. Seki, *Synth. Metals* 137 (2003) 911–912.
- [93] T. Yokoyama, D. Yoshimura, E. Ito, H. Ishii, Y. Ouchi, K. Seki, *Jpn. J. Appl. Phys. Part 1-Reg. Papers Short Notes Rev. Papers* 42 (2003) 3666–3675.
- [94] H. Ishii, N. Hayashi, E. Ito, Y. Washizu, K. Sugi, Y. Kimura, M. Niwano, Y. Ouchi, K. Seki, *Phys. Status Solidi A-Appl. Res.* 201 (2004) 1075–1094.
- [95] Y. Sakurai, T. Yokoyama, Y. Hosoi, H. Ishii, Y. Ouchi, G. Salvan, A. Kobitski, T.U. Kampen, D.R.T. Zahn, K. Seki, *Synth. Metals* 154 (2005) 161–164.
- [96] I.G. Hill, A. Kahn, *J. Appl. Phys.* 84 (1998) 5583–5586.
- [97] I.G. Hill, A. Rajagopal, A. Kahn, *J. Appl. Phys.* 84 (1998) 3236–3241.
- [98] F. Baier, F. von Ludowig, A. Soukopp, C. Vaterlein, J. Laubender, P. Bauerle, M. Sokolowski, E. Umbach, *Opt. Mater.* 12 (1999) 285–290.
- [99] T. Chasse, C.I. Wu, I.G. Hill, A. Kahn, *J. Appl. Phys.* 85 (1999) 6589–6592.
- [100] R. Schlaf, C.D. Merritt, L.A. Crisafulli, Z.H. Kafafi, *J. Appl. Phys.* 86 (1999) 5678–5686.
- [101] R. Schlaf, B.A. Parkinson, P.A. Lee, K.W. Nebesny, N.R. Armstrong, *J. Phys. Chem. B* 103 (1999) 2984–2992.
- [102] R. Schlaf, P.G. Schroeder, M.W. Nelson, B.A. Parkinson, P.A. Lee, K.W. Nebesny, N.R. Armstrong, *J. Appl. Phys.* 86 (1999) 1499–1509.
- [103] I.G. Hill, A.J. Makinen, Z.H. Kafafi, *Appl. Phys. Lett.* 77 (2000) 1825–1827.
- [104] I.G. Hill, D. Milliron, J. Schwartz, A. Kahn, *Appl. Surf. Sci.* 166 (2000) 354–362.
- [105] G. Koller, R.I.R. Blyth, S.A. Sardar, F.P. Netzer, M.G. Ramsey, *Appl. Phys. Lett.* 76 (2000) 927–929.
- [106] H. Peisert, T. Schwieger, M. Knupfer, M.S. Golden, J. Fink, *J. Appl. Phys.* 88 (2000) 1535–1540.
- [107] R. Schlaf, P.G. Schroeder, M.W. Nelson, B.A. Parkinson, C.D. Merritt, L.A. Crisafulli, H. Murata, Z.H. Kafafi, *Surf. Sci.* 450 (2000) 142–152.
- [108] P.G. Schroeder, M.W. Nelson, B.A. Parkinson, R. Schlaf, *Surf. Sci.* 459 (2000) 349–364.
- [109] R.I.R. Blyth, R. Duschek, G. Koller, F.P. Netzer, M.G. Ramsey, *Monatshefte Fur Chemie* 132 (2001) 509–518.
- [110] S. Park, T.U. Kampen, D.R.T. Zahn, W. Braun, *Appl. Phys. Lett.* 79 (2001) 4124–4126.
- [111] H. Peisert, T. Schwieger, M. Knupfer, M.S. Golden, J. Fink, *Synth. Metals* 121 (2001) 1435–1436.
- [112] R. Schlaf, C.D. Merritt, L.C. Picciolo, Z.H. Kafafi, *J. Appl. Phys.* 90 (2001) 1903–1910.
- [113] P. Sigaud, J.N. Chazalviel, F. Ozanam, O. Stephan, *J. Appl. Phys.* 89 (2001) 466–470.
- [114] X. Crispin, V. Geskin, A. Crispin, J. Cornil, R. Lazzaroni, W.R. Salaneck, J.L. Bredas, *J. Am. Chem. Soc.* 124 (2002) 8131–8141.
- [115] H. Peisert, M. Knupfer, J. Fink, *Surf. Sci.* 515 (2002) 491–498.
- [116] H. Peisert, M. Knupfer, T. Schwieger, J.M. Auerhammer, M.S. Golden, J. Fink, *J. Appl. Phys.* 91 (2002) 4872–4878.
- [117] M. Tengelin-Nilsson, L. Ilver, J. Kanski, *Org. Electron.* 3 (2002) 73–79.
- [118] S.C. Veenstra, A. Heeres, G. Hadzioannou, G.A. Sawatzky, H.T. Jonkman, *Appl. Phys. A-Mater. Sci. Process.* 75 (2002) 661–666.
- [119] D.R.T. Zahn, S. Park, T.U. Kampen, *Vacuum* 67 (2002) 101–113.
- [120] D.M. Alloway, M. Hofmann, D.L. Smith, N.E. Gruhn, A.L. Graham, R. Colorado, V.H. Wysocki, T.R. Lee, P.A. Lee, N.R. Armstrong, *J. Phys. Chem. B* 107 (2003) 11690–11699.
- [121] G. Cabailh, J.W. Wells, I.T. McGovern, V.R. Dhanak, A.R. Vearey-Roberts, A. Bushell, D.A. Evans, *J. Phys. Cond. Matter* 15 (2003) S2741–S2748.
- [122] D.A. Evans, H.J. Steiner, A.R. Vearey-Roberts, V. Dhanak, G. Cabailh, S. O'Brien, I.T. McGovern, W. Braun, T.U. Kampen, S. Park, D.R.T. Zahn, *Appl. Surf. Sci.* 212 (2003) 417–422.
- [123] W.Y. Gao, A. Kahn, *Appl. Phys. Lett.* 82 (2003) 4815–4817.
- [124] T.U. Kampen, G. Gavrilova, H. Mendez, D.R.T. Zahn, A.R. Vearey-Roberts, D.A. Evans, J. Wells, I. McGovern, W. Braun, *J. Phys. Cond. Matter* 15 (2003) S2679–S2692.
- [125] A.S. Komolov, P.J. Moller, E.F. Lazneva, *J. Electr. Spectrosc. Related Phen.* 131 (2003) 67–75.
- [126] G. Paasch, H. Peisert, M. Knupfer, J. Fink, S. Scheinert, *J. Appl. Phys.* 93 (2003) 6084–6089.
- [127] H. Peisert, M. Knupfer, T. Schwieger, G.G. Fuentes, D. Olligs, J. Fink, T. Schmidt, *J. Appl. Phys.* 93 (2003) 9683–9692.
- [128] H. Peisert, M. Knupfer, F. Zhang, A. Petr, L. Dunsch, J. Fink, *Appl. Phys. Lett.* 83 (2003) 3930–3932.
- [129] P.G. Schroeder, C.B. France, J.B. Park, B.A. Parkinson, *J. Phys. Chem. B* 107 (2003) 2253–2261.
- [130] X. Crispin, *Solar Energy Mater. Solar Cells* 83 (2004) 147–168.
- [131] S. Kera, Y. Yabuuchi, H. Yamane, H. Setoyama, K.K. Okudaira, A. Kahn, N. Ueno, *Phys. Rev. B* 70 (2004) 085304.
- [132] W. Zhao, W. Wei, J. Lozano, J.M. White, *Chem. Mater.* 16 (2004) 750–756.
- [133] P.S. Bagus, K. Hermann, C. Woll, *J. Chem. Phys.* 123 (2005) 184109.
- [134] M.M. Beerboom, R. Gargagliano, R. Schlaf, *Langmuir* 21 (2005) 3551–3558.
- [135] S.Y. Kim, J.M. Baik, J.L. Lee, *Electrochim. Solid State Lett.* 8 (2005) H79–H81.
- [136] S.Y. Kim, J.L. Lee, *Appl. Phys. Lett.* 87 (2005) 232105.
- [137] L. Lindell, M.P. de Jong, W. Osikowicz, R. Lazzaroni, M. Berggren, W.R. Salaneck, X. Crispin, *J. Chem. Phys.* 122 (2005) 084712.
- [138] X. Liu, M. Knupfer, B.H. Huisman, *Surf. Sci.* 595 (2005) 165–171.
- [139] T. Schwieger, X. Liu, H. Peisert, B. Adolphi, N. Kiriy, M. Knupfer, *J. Appl. Phys.* 97 (2005) 123712.
- [140] H. Vazquez, W. Gao, F. Flores, A. Kahn, *Phys. Rev. B* 71 (2005) 041306.
- [141] A. Wan, J. Hwang, F. Amy, A. Kahn, *Org. Electron.* 6 (2005) 47–54.
- [142] A. Kahn, W. Zhao, W.Y. Gao, H. Vazquez, F. Flores, *Chem. Phys.* 325 (2006) 129–137.
- [143] T.U. Kampen, *Appl. Phys. A-Mater. Sci. Process.* 82 (2006) 457–470.
- [144] S.Y. Kim, J.L. Lee, *Appl. Phys. Lett.* 89 (2006) 223515.
- [145] M. Knupfer, X. Liu, *Surf. Sci.* 600 (2006) 3978–3981.
- [146] K.M. Lau, J.X. Tang, H.Y. Sun, C.S. Lee, S.T. Lee, D.H. Yan, *Appl. Phys. Lett.* 88 (2006) 173513.
- [147] X. Liu, M. Knupfer, L. Dunsch, A. Tabet, H. Hartmann, *Org. Electron.* 7 (2006) 107–113.
- [148] P. Amsalem, L. Giovanelli, J.M. Themlin, M. Koudia, M. Abel, V. Oison, Y. Ksari, M. Mossyan, L. Porte, *Surf. Sci.* 601 (2007) 4185–4188.
- [149] S.W. Cho, K.H. Yoo, K. Jeong, C.N. Whang, Y. Yi, M. Noh, *Appl. Phys. Lett.* 91 (2007) 052102.
- [150] M. Fahlman, A. Crispin, X. Crispin, S.K.M. Henze, M.P. de Jong, W. Osikowicz, C. Tengstedt, W.R. Salaneck, *J. Phys. Cond. Matter.* 19 (2007) 183202.
- [151] M. Grobosch, M. Knupfer, *Org. Electron.* 8 (2007) 625–630.
- [152] S.Y. Kim, K. Hong, J.L. Lee, *Appl. Phys. Lett.* 90 (2007) 183508.
- [153] G. Koller, B. Winter, M. Oehzelt, J. Ivancic, F.P. Netzer, M.G. Ramsey, *Org. Electron.* 8 (2007) 63–68.
- [154] S.L. Lai, M.Y. Chan, M.K. Fung, C.S. Lee, S.T. Lee, *J. Appl. Phys.* 101 (2007).
- [155] G. Paasch, S. Scheinert, *J. Appl. Phys.* 101 (2007) 024514.
- [156] F. Petracchi, V. Papaefthimiou, S. Kennou, *Org. Electron.* 8 (2007) 522–528.
- [157] S.W. Cho, Y. Yi, M. Noh, M.H. Cho, K.H. Yoo, K. Jeong, C.N. Whang, *Synth. Metals* 158 (2008) 539–543.
- [158] S. Duhm, G. Heimel, I. Salzmann, H. Glowatzkl, R.L. Johnson, A. Vollmer, J.P. Rabe, N. Koch, *Nat. Mater.* 7 (2008) 326–332.
- [159] M. Grobosch, M. Knupfer, *Org. Electron.* 9 (2008) 767–774.
- [160] M. Grobosch, M. Knupfer, K. Dorr, R.B. Gangineini, *Phys. Status Solidi B-Basic Solid State Phys.* 245 (2008) 799–803.
- [161] S.Y. Kim, J.L. Lee, *Org. Electron.* 9 (2008) 678–686.
- [162] L. Lindell, M. Unge, W. Osikowicz, S. Stafstrom, W.R. Salaneck, X. Crispin, M.P. de Jong, *Appl. Phys. Lett.* 92 (2008) 163302.
- [163] C. Risko, C.D. Zangmeister, Y. Yao, T.J. Marks, J.M. Tour, M.A. Ratner, R.D. van Zee, *J. Phys. Chem. C* 112 (2008) 13215–13225.
- [164] J.X. Tang, Y.C. Zhou, Z.T. Liu, C.S. Lee, S.T. Lee, *Appl. Phys. Lett.* 93 (2008) 043512.
- [165] Y.Q. Zhan, M.P. de Jong, F.H. Li, V. Dediu, M. Fahlman, W.R. Salaneck, *Phys. Rev. B* 78 (2008).
- [166] W. Zhao, E. Salomon, Q. Zhang, S. Barlow, S.R. Marder, A. Kahn, *Phys. Rev. B* 77 (2008) 165336.
- [167] Q.T. Le, F. Nuesch, L.J. Rothberg, E.W. Forsythe, Y.L. Gao, *Appl. Phys. Lett.* 75 (1999) 1357–1359.
- [168] Q.T. Le, E.W. Forsythe, F. Nuesch, L.J. Rothberg, L. Yan, Y. Gao, *Thin Solid Films* 363 (2000) 42–46.
- [169] L. Yan, M.G. Mason, C.W. Tang, Y.L. Gao, *Appl. Surf. Sci.* 175 (2001) 412–418.
- [170] N.J. Watkins, L. Yan, Y.L. Gao, *Appl. Phys. Lett.* 80 (2002) 4384–4386.
- [171] L. Yan, Y.L. Gao, *Thin Solid Films* 417 (2002) 101–106.
- [172] L. Yan, N.J. Watkins, S. Zorba, Y.L. Gao, C.W. Tang, *Appl. Phys. Lett.* 81 (2002) 2752–2754.
- [173] N.J. Watkins, Y. Gao, *J. Appl. Phys.* 94 (2003) 1289–1291.
- [174] N.J. Watkins, S. Zorba, Y.L. Gao, *J. Appl. Phys.* 96 (2004) 425–429.
- [175] I.G. Hill, A. Rajagopal, A. Kahn, Y. Hu, *Appl. Phys. Lett.* 73 (1998) 662–664.
- [176] A. Rajagopal, C.I. Wu, A. Kahn, *J. Appl. Phys.* 83 (1998) 2649–2655.

- [177] P. He, S.D. Wang, W.K. Wong, C.S. Lee, S.T. Lee, *Appl. Phys. Lett.* 79 (2001) 1561–1563.
- [178] N. Koch, E. Zoyer, A. Rajagopal, J. Ghijssen, R.L. Johnson, G. Leising, J.J. Pireaux, *Adv. Funct. Mater.* 11 (2001) 51–58.
- [179] V. Papaefthimiou, A. Siokou, S. Kennou, *J. Appl. Phys.* 91 (2002) 4213–4219.
- [180] H. Peisert, M. Knupfer, J. Fink, *Appl. Phys. Lett.* 81 (2002) 2400–2402.
- [181] P. Sigaud, J.N. Chazalviel, F. Ozanam, *J. Appl. Phys.* 92 (2002) 992–996.
- [182] V. Papaefthimiou, A. Siokou, S. Kennou, *Thin Solid Films* 459 (2004) 32–36.
- [183] V. Papaefthimiou, A. Siokou, S. Kennou, *Surf. Sci.* 569 (2004) 207–218.
- [184] H. Vazquez, F. Flores, R. Oszwaldowski, J. Ortega, R. Perez, A. Kahn, *Appl. Surf. Sci.* 234 (2004) 107–112.
- [185] H. Vazquez, R. Oszwaldowski, P. Pou, J. Ortega, R. Perez, F. Flores, A. Kahn, *Europhys. Lett.* 65 (2004) 802–808.
- [186] X.Y. Zhu, *J. Phys. Chem. B* 108 (2004) 8778–8793.
- [187] S.K.M. Jonsson, E. Carlegrim, F. Zhang, W.R. Salaneck, M. Fahlman, *Jpn. J. Appl. Phys. Part 1-Regular Papers Short Notes Rev. Papers* 44 (2005) 3695–3701.
- [188] S.K.M. Jonsson, W.R. Salaneck, M. Fahlman, *J. Appl. Phys.* 98 (2005) 014901.
- [189] S.G. Ray, H. Cohen, R. Naaman, H.Y. Liu, D.H. Waldeck, *J. Phys. Chem. B* 109 (2005) 14064–14073.
- [190] P. Szymanski, S. Garrett-Roe, C.B. Harris, *Prog. Surf. Sci.* 78 (2005) 1–39.
- [191] M. Ambroto, M. Losurdo, P. Capezzutto, G. Bruno, T. Ligonzo, H. Haick, *Appl. Surf. Sci.* 252 (2006) 7636–7641.
- [192] P. Destruel, H. Bock, I. Seguy, P. Jolinat, M. Oukachmih, E. Bedel-Pereira, *Polym. Int.* 55 (2006) 601–607.
- [193] R. Hunger, W. Jaegermann, A. Merson, Y. Shapira, C. Pettenkofer, J. Rappich, *J. Phys. Chem. B* 110 (2006) 15432–15441.
- [194] Y.J. Lin, J.H. Hong, Y.C. Lien, B.Y. Liu, *Appl. Phys. Lett.* 89 (2006) 262110.
- [195] O.V. Molodtsova, M. Knupfer, *J. Appl. Phys.* 99 (2006) 053704.
- [196] V. Papaefthimiou, A. Siokou, S. Kennou, *Surf. Sci.* 600 (2006) 3987–3991.
- [197] C. Tengstedt, W. Osikowicz, W.R. Salaneck, I.D. Parker, C.H. Hsu, M. Fahlman, *Appl. Phys. Lett.* 88 (2006) 053502–053504.
- [198] S.D. Wang, K. Kanai, E. Kawabe, Y. Ouchi, K. Seki, *Mol. Cryst. Liquid Cryst.* 455 (2006) 339–346.
- [199] S. Balaz, A.N. Caruso, N.P. Platt, D.I. Dimov, N.M. Boag, J.I. Brand, Y.B. Losovyj, P.A. Dowben, *J. Phys. Chem. B* 111 (2007) 7009–7016.
- [200] S. Braun, W. Osikowicz, Y. Wang, W.R. Salaneck, *Org. Electron.* 8 (2007) 14–20.
- [201] P. He, *Int. J. Nanotechnol.* 4 (2007) 100–109.
- [202] J. Lee, J.S. Lim, H.J. Shin, Y. Park, *Appl. Phys. Lett.* 91 (2007) 261902.
- [203] H. Yamane, D. Yoshimura, E. Kawabe, R. Sumii, K. Kanai, Y. Ouchi, N. Ueno, K. Seki, *Phys. Rev. B* 76 (2007) 165436.
- [204] F. Zhang, A. Vollmer, J. Zhang, Z. Xu, J.P. Rabe, N. Koch, *Org. Electron.* 8 (2007) 606–614.
- [205] W.H. Zhang, X. Mo, G.D. Wang, L.W. Wang, F.Q. Xu, H.B. Pan, M.M. Shi, H.Z. Chen, M. Wang, *Acta Phys. Sin.* 56 (2007) 4936–4942.
- [206] M.G. Betti, A. Kanjalil, C. Mariani, H. Vazquez, Y.J. Dappe, J. Ortega, F. Flores, *Phys. Rev. Lett.* 100 (2008) 027601.
- [207] F. Evangelista, A. Ruocco, D. Pasca, C. Baldacchini, M.G. Betti, V. Corradini, C. Mariani, *Surf. Sci.* 566 (2004) 79–83.
- [208] W. Chen, S. Chen, H. Huang, D.C. Qi, X.Y. Gao, A.T.S. Wee, *Appl. Phys. Lett.* 92 (2008) 063308–063310.
- [209] P.A. Dowben, J. Xiao, B. Xu, A. Sokolov, B. Doudin, *Appl. Surf. Sci.* 254 (2008) 4238–4244.
- [210] T. He, H.J. Ding, N. Peor, M. Lu, D.A. Corley, B. Chen, Y. Ofir, Y.L. Gao, S. Yitzchaik, J.M. Tour, *J. Am. Chem. Soc.* 130 (2008) 1699–1710.
- [211] M.G. Helander, Z.B. Wang, L. Mordoukhovski, Z.H. Lu, *J. Appl. Phys.* 104 (2008) 094510.
- [212] E. Kawabe, H. Yamane, R. Sumii, K. Koizumi, Y. Ouchi, K. Seki, K. Kanai, *Org. Electron.* 9 (2008) 783–789.
- [213] N. Koch, A. Gerlach, S. Duhm, H. Glowatzki, G. Heimel, A. Vollmer, Y. Sakamoto, T. Suzuki, J. Zegenhagen, J.P. Rabe, F. Schreiber, *J. Am. Chem. Soc.* 130 (2008) 7300–7304.
- [214] G.B. Murdoch, M. Greiner, M.G. Helander, Z.B. Wang, Z.H. Lu, *Appl. Phys. Lett.* 93 (2008) 083309.
- [215] R.T. Tung, *Phys. Rev. Lett.* 84 (2000) 6078–6081.
- [216] N.D. Lang, *Phys. Rev. Lett.* 46 (1981) 842–845.
- [217] H. Vazquez, F. Flores, A. Kahn, *Org. Electron.* 8 (2007) 241–248.
- [218] J.X. Tang, C.S. Lee, S.T. Lee, Y.B. Xu, *Chem. Phys. Lett.* 396 (2004) 92–96.
- [219] M. Schlüter, *Phys. Rev. B* 17 (1978) 5044.
- [220] J.L. Brillson, *Surf. Sci. Rep.* 2 (1982) 123–326.
- [221] I.H. Campbell, D.L. Smith, *Appl. Phys. Lett.* 74 (1999) 561–563.
- [222] E. Tutis, M.N. Bussac, L. Zuppiroli, *Appl. Phys. Lett.* 75 (1999) 3880–3882.
- [223] T. Kampen, A. Bekkali, I. Thurzo, D.R.T. Zahn, A. Bolognesi, T. Ziller, A. Di Carlo, P. Lugli, *Appl. Surf. Sci.* 234 (2004) 313–320.
- [224] V.Y. Aristov, O.V. Molodtsova, V.M. Zhilin, Y.A. Ossipyan, D.V. Vyalikh, B.P. Doyle, S. Nannarone, M. Knupfer, *Euro. Phys. J. B* 57 (2007) 379–384.
- [225] M. Bassler, R. Fink, C. Heske, J. Müller, P. Vaterlein, J.U. vonSchutz, E. Umbach, *Thin Solid Films* 284 (1996) 234–237.
- [226] A. Brevet, L. Imhoff, M.C.M. de Lucas, B. Domenichini, S. Bourgeois, *Thin Solid Films* 515 (2007) 6407–6410.
- [227] M.Y. Chan, S.L. Lai, M.K. Fung, S.W. Tong, C.S. Lee, S.T. Lee, *Appl. Phys. Lett.* 82 (2003) 1784–1786.
- [228] K. Fehse, S. Olthof, K. Walzer, K. Leo, R.L. Johnson, H. Glowatzki, B. Broker, N. Koch, *J. Appl. Phys.* 102 (2007) 073719.
- [229] M.A. Filler, S.F. Bent, *Prog. Surf. Sci.* 73 (2003) 1–56.
- [230] M. Gorgoi, D.R.T. Zahn, *J. Phys. IV* 132 (2006) 337–340.
- [231] Y. Hirose, A. Kahn, V. Aristov, P. Soukiassian, *Appl. Phys. Lett.* 68 (1996) 217–219.
- [232] Y. Hirose, A. Kahn, V. Aristov, P. Soukiassian, V. Bulovic, S.R. Forrest, *Phys. Rev. B* 54 (1996) 13748–13758.
- [233] L.S. Hung, S.T. Lee, *Mater. Sci. Eng. B-Solid State Mater. Adv. Technol.* 85 (2001) 104–108.
- [234] N. Isomura, T. Satoh, M. Suzuki, T. Ohwaki, Y. Taga, *Jpn. J. Appl. Phys. Part 2-Lett.* 40 (2001) L1038–L1039.
- [235] S. Kwon, S.C. Kim, Y. Kim, S. Kim, K. Jeong, *Appl. Phys. Lett.* 79 (2001) 4595–4597.
- [236] S.L. Lai, M.Y. Chan, C.S. Lee, S.T. Lee, *J. Appl. Phys.* 94 (2003) 7297–7299.
- [237] R. Lazzaroni, M. Logdlund, A. Calderone, J.L. Bredas, P. Dannerun, C. Fauquet, C. Fredriksson, S. Stafstrom, W.R. Salaneck, *Synth. Metals* 71 (1995) 2159–2162.
- [238] Q.T. Le, L. Yan, V.E. Choong, E.W. Forsythe, M.G. Mason, C.W. Tang, Y.L. Gao, *Synth. Metals* 102 (1999) 1014–1015.
- [239] Q.T. Le, L. Yan, Y.G. Gao, M.G. Mason, D.J. Giesen, C.W. Tang, *J. Appl. Phys.* 87 (2000) 375–379.
- [240] J.T. Lim, J.H. Lee, Y.S. Kim, G.Y. Yeom, *J. Korean Phys. Soc.* 52 (2008) 476–480.
- [241] M.G. Mason, C.W. Tang, L.S. Hung, P. Raychaudhuri, J. Madathil, D.J. Giesen, L. Yan, Q.T. Le, Y. Gao, S.T. Lee, L.S. Liao, L.F. Cheng, W.R. Salaneck, D.A. dos Santos, J.L. Bredas, *J. Appl. Phys.* 89 (2001) 2756–2765.
- [242] T. Naito, T. Inabe, H. Niimi, K. Asakura, *Synth. Metals* 152 (2005) 289–292.
- [243] M. Onoue, M. Shionoiri, S. Kera, K.K. Okudaira, N. Ueno, *J. Elect. Spectrosc. Related Phen.* 137 (2004) 131–135.
- [244] W. Osikowicz, X. Crispin, C. Tengstedt, L. Lindell, T. Kugler, W.R. Salaneck, *Appl. Phys. Lett.* 85 (2004) 1616–1618.
- [245] S. Park, T.U. Kampen, W. Braun, D.R.T. Zahn, *Appl. Surf. Sci.* 175 (2001) 249–254.
- [246] S.A. Sardar, J.A. Syed, K. Tanaka, F.P. Netzer, M.G. Ramsey, *Surf. Sci.* 519 (2002) 218–228.
- [247] K. Seino, W.G. Schmidt, M. Preuss, F. Bechstedt, *J. Phys. Chem. B* 107 (2003) 5031–5035.
- [248] C. Shen, A. Kahn, J. Schwartz, *J. Appl. Phys.* 89 (2001) 449–459.
- [249] C.F. Shen, A. Kahn, J. Schwartz, *J. Appl. Phys.* 90 (2001) 6236–6242.
- [250] J.X. Tang, C.S. Lee, S.T. Lee, *Appl. Surf. Sci.* 252 (2006) 3948–3952.
- [251] J. Thompson, R.I.R. Blyth, V. Arima, Y. Zou, R. Fink, E. Umbach, G. Gigli, R. Cingolani, *Mater. Sci. Eng. B—Solid state materials for advanced technology* 105 (2003) 41–43.
- [252] N.J. Watkins, G.P. Kushto, A.J. Mäkinen, *J. Appl. Phys.* 104 (2008) 013712.
- [253] C.I. Wu, C.T. Lin, Y.H. Chen, M.H. Chen, Y.J. Lu, C.C. Wu, *Appl. Phys. Lett.* 88 (2006) 152104.
- [254] X.W. Zhan, C. Risko, F. Amy, C. Chan, W. Zhao, S. Barlow, A. Kahn, J.L. Bredas, S.R. Marder, *J. Am. Chem. Soc.* 127 (2005) 9021–9029.
- [255] R.Q. Zhang, C.S. Lee, S.T. Lee, *J. Chem. Phys.* 112 (2000) 8614–8620.
- [256] A. Rajagopal, A. Kahn, *J. Appl. Phys.* 84 (1998) 355–358.
- [257] A. Rajagopal, N. Koch, J. Ghijssen, R.L. Johnson, K. Kaeriyama, G. Leising, J.J. Pireaux, *J. Appl. Phys.* 87 (2000) 1331–1336.
- [258] T.P. Nguyen, J. Ip, P. Jolinat, P. Destruel, *Appl. Surf. Sci.* 172 (2001) 75–83.
- [259] G. Parthasarathy, C. Shen, A. Kahn, S.R. Forrest, *J. Appl. Phys.* 89 (2001) 4986–4992.
- [260] C. Shen, A. Kahn, *J. Appl. Phys.* 90 (2001) 4549–4554.
- [261] T.P. Nguyen, J. Ip, *Appl. Surf. Sci.* 195 (2002) 251–262.
- [262] M.Y. Chan, S.L. Lai, C.S. Lee, S.T. Lee, *Chem. Phys. Lett.* 380 (2003) 298–303.
- [263] A.C. Durr, N. Koch, M. Kelsch, A. Ruhm, J. Ghijssen, R.L. Johnson, J.J. Pireaux, J. Schwartz, F. Schreiber, H. Dosch, A. Kahn, *Phys. Rev. B* 68 (2003) 115428.
- [264] M.K. Fung, S.W. Tong, S.L. Lai, S.N. Bao, C.S. Lee, W.W. Wu, M. Inbasekaran, J.J. O'Brien, S.Y. Liu, S.T. Lee, *J. Appl. Phys.* 94 (2003) 2686–2694.
- [265] J. Ip, T.P. Nguyen, P. Le Rendu, *Synth. Metals* 138 (2003) 107–111.
- [266] S.K.M. Jonsson, M.P. de Jong, L. Groenendaal, W.R. Salaneck, M. Fahlman, *J. Phys. Chem. B* 107 (2003) 10793–10800.
- [267] M. Onoue, J. Miyachi, M. Shionoiri, S. Kera, K.K. Okudaira, Y. Harada, N. Ueno, *Jpn. J. Appl. Phys. Part 2-Lett.* 42 (2003) L1465–L1468.
- [268] L. Lozzi, S. Santucci, S. La Rosa, *J. Vacuum Sci. Technol. A* 22 (2004) 1477–1481.
- [269] T.P. Nguyen, P. Le Rendu, P.D. Long, S.A. De Vos, *Surf. Coat. Technol.* 180 (2004) 646–649.
- [270] S.M. Tadayyon, H.M. Grandin, K. Griffiths, L.L. Coatsworth, P.R. Norton, H. Aziz, Z.D. Popovic, *Org. Electron.* 5 (2004) 199–205.
- [271] V.Y. Aristov, O.V. Molodtsova, V.M. Zhilin, D.V. Vyalikh, M. Knupfer, *Phys. Rev. B* 72 (2005) 165318.
- [272] M. Shionoiri, I. Yamamoto, M. Onoue, S. Kera, K.K. Okudaira, N. Ueno, *Synth. Metals* 152 (2005) 301–304.
- [273] T.P. Nguyen, J. Ip, C. Renaud, C.H. Huang, C. Guillen, J. Herrero, *Appl. Surf. Sci.* 252 (2006) 8388–8393.
- [274] G.P. Ou, Z. Song, Y.Y. Wu, X.Q. Chen, F.J. Zhang, *Chin. Phys.* 15 (2006) 1296–1300.
- [275] Q.L. Song, M.L. Wang, E.G. Obbard, X.Y. Sun, X.M. Ding, X.Y. Hou, C.M. Li, *Appl. Phys. Lett.* 89 (2006).
- [276] K.P. Weidkamp, R.M. Tromp, R.J. Hamers, *J. Phys. Chem. C* 111 (2007) 16489–16497.
- [277] M. Batzill, K. Katsiev, U. Diebold, *Appl. Phys. Lett.* 85 (2004) 5766–5768.
- [278] S. Braun, W.R. Salaneck, *Chem. Phys. Lett.* 438 (2007) 259–262.
- [279] W. Chen, X.Y. Gao, D.C. Qi, S. Chen, Z.K. Chen, A.T.S. Wee, *Adv. Funct. Mater.* 17 (2007) 1339–1344.
- [280] W. Chen, C. Huang, X.Y. Gao, L. Wang, C.G. Zhen, D.C. Qi, S. Chen, H.L. Zhang, K.P. Loh, Z.K. Chen, A.T.S. Wee, *J. Phys. Chem. B* 110 (2006) 26075–26080.
- [281] S. Duhm, A. Gerlach, I. Salzmann, B. Broker, R.L. Johnson, F. Schreiber, N. Koch, *Org. Electron.* 9 (2008) 111–118.
- [282] S. Duhm, H. Glowatzki, V. Cimpeanu, J. Klankermayer, J.P. Rabe, R.L. Johnson, N. Koch, *J. Phys. Chem. B* 110 (2006) 21069–21072.

- [283] M.K. Fung, S.L. Lai, S.N. Bao, C.S. Lee, S.T. Lee, W.W. Wu, M. Inbasekaran, J.J. O'Brien, *J. Vacuum Sci. Technol. A—Vacuum Surf. Films* 20 (2002) 911–918.
- [284] D. Gador, C. Buchberger, A. Soukopp, E. Sokolowski, R. Fink, E. Umbach, *J. Elect. Spectrosc. Related Phen.* 103 (1999) 529–537.
- [285] W.Y. Gao, A. Kahn, *J. Appl. Phys.* 94 (2003) 359–366.
- [286] L. Giovannelli, P. Amsalem, J.M. Themlin, Y. Ksari, M. Abel, L. Nony, M. Koudia, F. Bondino, E. Magnano, M. Mossoyan-Deneux, L. Porte, *J. Phys. Chem. C* 112 (2008) 8654–8661.
- [287] S.C. Kim, J.W. Kim, J. Lee, Y. Park, *J. Korean Phys. Soc.* 53 (2008) 812–817.
- [288] N. Koch, S. Duhm, J.P. Rabe, A. Vollmer, R.L. Johnson, *Phys. Rev. Lett.* 95 (2005) 237601.
- [289] A. Komolov, P.J. Moller, *Colloids Surf. A—Physicochem. Eng. Aspects* 239 (2004) 49–54.
- [290] A.J. Makinen, M. Uchida, Z.H. Kafafi, *J. Appl. Phys.* 95 (2004) 2832–2838.
- [291] H. Peisert, M. Knupfer, F. Zhang, A. Petr, L. Dunsch, J. Fink, *Surf. Sci.* 566 (2004) 554–559.
- [292] H. Peisert, A. Petr, L. Dunsch, T. Chasse, M. Knupfer, *Chemphyschem* 8 (2007) 386–390.
- [293] L. Romaner, G. Heimel, J.L. Bredas, A. Gerlach, F. Schreiber, R.L. Johnson, J. Zegenhagen, S. Duhm, N. Koch, E. Zoyer, *Phys. Rev. Lett.* 99 (2007) 256801.
- [294] T. Schwieger, H. Peisert, M. Knupfer, *Chem. Phys. Lett.* 384 (2004) 197–202.
- [295] S.K. Sengupta, H. Ahn, J.E. Whitten, *Surf. Sci.* 520 (2002) 207–216.
- [296] J.X. Tang, C.S. Lee, M.Y. Chan, S.T. Lee, *Appl. Surf. Sci.* 254 (2008) 7688–7692.
- [297] J.X. Tang, Y.Q. Li, X. Dong, S.D. Wang, C.S. Lee, L.S. Hung, S.T. Lee, *Appl. Surf. Sci.* 239 (2004) 117–124.
- [298] H. Razafitrimo, E. Etchedgui, L.H. Guo, G.L. McLendon, Y. Gao, *Appl. Phys. Lett.* 67 (1995) 2621–2623.
- [299] Q.T. Le, F.M. Avendano, E.W. Forsythe, L. Yan, Y.L. Gao, C.W. Tang, *J. Vacuum Sci. Technol.* 17 (1999) 2314–2317.
- [300] N.J. Watkins, Y. Gao, *J. Appl. Phys.* 94 (2003) 5782–5786.
- [301] V.E. Choong, M.G. Mason, C.W. Tang, Y.G. Gao, *Appl. Phys. Lett.* 72 (1998) 2689–2691.
- [302] Y. Park, V. Choong, E. Etchedgui, Y. Gao, B.R. Hsieh, T. Wehrmeister, K. Mullen, *Appl. Phys. Lett.* 69 (1996) 1080–1082.
- [303] Y. Park, V.E. Choong, B.R. Hsieh, C.W. Tang, Y. Gao, *Phys. Rev. Lett.* 78 (1997) 3955–3958.
- [304] Y. Park, V.E. Choong, B.R. Hsieh, C.W. Tang, T. Wehrmeister, K. Mullen, Y. Gao, *J. Vacuum Sci. Technol. A—Vacuum Surf. Films* 15 (1997) 2574–2578.
- [305] L. Yan, Charge transfer and injection barrier at metal-organic interfaces, in: *Physics and Astronomy*, vol Doctor of Philosophy, University of Rochester, Rochester, 2002, p. 158.
- [306] N.J. Watkins, A.J. Makinen, Y. Gao, M. Uchida, Z.H. Kafafi, *J. Appl. Phys.* 100 (2006) 103706.
- [307] N.J. Watkins, Y. Li, Y.L. Gao, *Abstracts of Papers of the American Chemical Society* 224 (2002) U60–U160.
- [308] N.J. Watkins, Q.T. Le, S. Zorba, L. Yan, Y. Gao, S.F. Nelson, C.S. Kuo, T.N. Jackson, *SPIE Proc.* 4466 (2001) 1.
- [309] N.J. Watkins, Interface studies of organic thin film transistors, in: *Physics and Astronomy*, vol Doctor of Philosophy, University of Rochester, Rochester, 2002, p. 204.
- [310] A. Tanaka, L. Yan, N.J. Watkins, Y.L. Gao, *J. Elect. Spectrosc. Related Phen.* 144 (2005) 327–329.
- [311] H. Razafitrimo, K.T. Park, E. Etchedgui, Y. Gao, B.R. Hsieh, *Polym. Int.* 36 (1995) 147–153.
- [312] S. Pyo, L.P. Ma, J. He, Q.F. Xu, Y. Yang, Y.L. Gao, *J. Appl. Phys.* 98 (2005) 054303.
- [313] Y. Park, E. Etchedgui, Y. Gao, B.R. Hsieh, K. Mullen, *Abstracts of Papers of the American Chemical Society* 210 (1995) 166–POLY.
- [314] T.P. Nguyen, S. Lefrant, S. deVos, Y. Gao, *Synth. Metals* 84 (1997) 659–660.
- [315] A.J. Makinen, S. Xu, Z. Zhang, S.J. Diol, Y.L. Gao, M.G. Mason, A.A. Muenter, D.A. Mantell, A.R. Melnyk, *Appl. Phys. Lett.* 74 (1999) 1296–1298.
- [316] A.J. Makinen, S. Xu, Z. Zhang, S.J. Diol, Y. Gao, M.G. Mason, A.A. Muenter, D.A. Mantell, A.R. Melnyk, *J. Vacuum Sci. Technol. A—Vacuum Surf. Films* 17 (1999) 2329–2332.
- [317] H.G. Lee, S. Kim, C. Hwang, V. Choong, Y. Park, Y. Gao, B.R. Hsieh, *J. Appl. Phys.* 82 (1997) 4962–4965.
- [318] N. Koch, R. Pairleitner, Q.T. Le, E.W. Forsythe, Y. Gao, G. Leising, *Appl. Phys. Lett.* 76 (2000) 3738–3740.
- [319] C. Hochfilzer, G. Leising, Y. Gao, E. Forsythe, C.W. Tang, *Appl. Phys. Lett.* 73 (1998) 2254–2256.
- [320] L.H. Guo, G. McLendon, H. Razafitrimo, Y.L. Gao, *J. Mater. Chem.* 6 (1996) 369–374.
- [321] E.W. Forsythe, M.A. Abkowitz, Y.L. Gao, C.W. Tang, *J. Vacuum Sci. A—Vacuum Surf. Films* 18 (2000) 1869–1874.
- [322] E.W. Forsythe, M.A. Abkowitz, Y.L. Gao, *Journal of Physical Chemistry B* 104 (2000) 3948–3952.
- [323] J.X. Tang, K.M. Lau, C.S. Lee, S.T. Lee, *Appl. Phys. Lett.* 88 (2006) 232103.
- [324] Y.L. Gao, H.J. Ding, H.B. Wang, D.H. Yan, *Appl. Phys. Lett.* 91 (2007) 142112.
- [325] E. Etchedgui, H. Razafitrimo, Y. Gao, B.R. Hsieh, W.A. Feld, M.W. Ruckman, *Phys. Rev. Lett.* 76 (1996) 299–302.
- [326] M. Westphalen, U. Kreibig, J. Rostalski, H. Luth, D. Meissner, *Solar Energy Mater. Solar Cells* 61 (2000) 97–105.
- [327] N. Koch, J. Ghijssen, R.L. Johnson, J. Schwartz, J.J. Pireaux, A. Kahn, *J. Phys. Chem. B* 106 (2002) 4192–4196.
- [328] N. Koch, A.C. Durr, J. Ghijssen, R.L. Johnson, J.J. Pireaux, J. Schwartz, F. Schreiber, H. Dosch, A. Kahn, *Thin Solid Films* 441 (2003) 145–149.
- [329] E. Moons, A. Goossens, T. Savenije, *J. Phys. Chem. B* 101 (1997) 8492–8498.
- [330] M. Eschle, E. Moons, M. Gratzel, *Opt. Mater.* 9 (1998) 138–144.
- [331] L. Zuppipoli, L. Si-Ahmed, K. Kamaras, F. Nuesch, M.N. Bussac, D. Ades, A. Siove, E. Moons, M. Gratzel, *Euro. Phys. J. B* 11 (1999) 505–512.
- [332] L. Burgi, H. Sirringhaus, R.H. Friend, *Appl. Phys. Lett.* 80 (2002) 2913–2915.
- [333] N.E. Cant, H.L. Zhang, K. Critchley, T.A. Mykhalyk, G.R. Davies, S.D. Evans, *J. Phys. Chem. B* 107 (2003) 13557–13562.
- [334] R.A. Hatton, M.R. Willis, M.A. Chesters, F.J.M. Rutten, D. Briggs, *J. Mater. Chem.* 13 (2003) 38–43.
- [335] A.B. Sieval, C.L. Huisman, A. Schonecker, F.M. Schuurmans, A.S.H. van der Heide, A. Goossens, W.C. Sinke, H. Zuilhof, E.J.R. Sudholter, *J. Phys. Chem. B* 107 (2003) 6846–6852.
- [336] A.D.Q. Li, L.S. Li, *J. Phys. Chem. B* 108 (2004) 12842–12850.
- [337] O. Tal, W. Gao, C.K. Chan, A. Kahn, Y. Rosenwaks, *Appl. Phys. Lett.* 85 (2004) 4148–4150.
- [338] T. Nishikawa, S. Kobayashi, T. Nakanoowatari, T. Mitani, T. Shimoda, Y. Kubozono, G. Yamamoto, H. Ishii, M. Niwano, Y. Iwasa, *J. Appl. Phys.* 97 (2005) 104509.
- [339] K. Puntambekar, J.P. Dong, G. Haugstad, C.D. Frisbie, *Adv. Funct. Mater.* 16 (2006) 879–884.
- [340] S. Ikeda, T. Shimada, M. Kiguchi, K. Saiki, *J. Appl. Phys.* 101 (2007) 094509.
- [341] S.H. Jee, S.H. Kim, K.H. Lee, J.H. Ko, Y.S. Yoon, *J. Korean Phys. Soc.* 50 (2007) 915–919.
- [342] I. Muzikante, V. Parra, R. Dobulans, E. Fonavs, J. Latvels, M. Bouvet, *Sensors* 7 (2007) 2984–2996.
- [343] R.R. Chance, A. Prock, A.R. Silbey, *Adv. Chem. Phys.* 37 (1978) 1.
- [344] V. Choong, Y. Park, Y. Gao, T. Wehrmeister, K. Mullen, B.R. Hsieh, C.W. Tang, *Appl. Phys. Lett.* 69 (1996) 1492–1494.
- [345] V. Choong, Y. Park, Y. Gao, T. Wehrmeister, K. Mullen, B.R. Hsieh, C.W. Tang, *Abstracts of Papers of the American Chemical Society* 212 (1996) 277–POLY.
- [346] V.E. Choong, Y. Park, Y. Gao, *Abstracts of Papers of the American Chemical Society* 213 (1997) 280–POLY.
- [347] V.E. Choong, Y. Park, Y. Gao, T. Wehrmeister, K. Mullen, B.R. Hsieh, C.W. Tang, *J. Vacuum Sci. Technol. A—Vacuum Surf. Films* 15 (1997) 1745–1749.
- [348] V.E. Choong, Y. Park, B.R. Hsieh, Y. Gao, *Phys. Rev. B* 55 (1997) 15460–15463.
- [349] V.E. Choong, Y. Park, N. Shivaparan, C.W. Tang, Y. Gao, *Appl. Phys. Lett.* 71 (1997) 1005–1007.
- [350] V.E. Choong, Y. Park, Y. Gao, M.G. Mason, C.W. Tang, *J. Vacuum Sci. Technol. A—Vacuum Surf. Films* 16 (1998) 1838–1841.
- [351] V.E. Choong, Y. Park, Y.L. Gao, B.R. Hsieh, C.W. Tang, *Macromol. Symp.* 125 (1998) 83–97.
- [352] N. Dam, M.M. Beerbom, J.C. Braunagel, R. Schlaf, *J. Appl. Phys.* 97 (2005) 024909.
- [353] Z.B. Deng, X.M. Ding, L.S. Liao, X.Y. Hou, S.T. Lee, *Displays* 21 (2000) 79–82.
- [354] S. Gardonio, L. Gregoratti, D. Scaini, C. Castellarin-Cudia, P. Dudin, P. Melpignano, V. Biondo, R. Zamboni, S. Caria, M. Kiskinova, *Org. Electron.* 9 (2008) 253–261.
- [355] M. Grobosch, M. Knupfer, *Adv. Mater.* 19 (2007) 754.
- [356] S.Y. Kim, K. Hong, J.H. Son, G.H. Jung, J.L. Lee, K.H. Choi, K.H. Song, K.C. Ahn, *Jpn. J. Appl. Phys.* 47 (2008) 862–866.
- [357] E.S. Lee, J.H. Choi, H.K. Baik, *Surf. Coat. Technol.* 201 (2007) 4973–4978.
- [358] S.K. So, W.K. Choi, C.H. Cheng, L.M. Leung, C.F. Kwong, *Appl. Phys. a-Mater. Sci. Process.* 68 (1999) 447–450.
- [359] Y. Gao, K.T. Park, B.R. Hsieh, *J. Chem. Phys.* 97 (1992) 6991–6993.
- [360] Y. Gao, K.T. Park, B.R. Hsieh, *J. Appl. Phys.* 73 (1993) 7894–7899.
- [361] E. Etchedgui, H. Razafitrimo, K.T. Park, Y. Gao, B.R. Hsieh, *J. Appl. Phys.* 75 (1994) 7526–7530.
- [362] B.R. Hsieh, E. Etchedgui, K.T. Park, Y. Gao, *Molecular Crystals and Liquid Crystals Science and Technology Section a-Molecular Crystals and Liquid Crystals* 256 (1994) 71–78.
- [363] E. Etchedgui, H. Razafitrimo, K.T. Park, Y. Gao, B.R. Hsieh, *Surf. Interf. Anal.* 23 (1995) 89–98.
- [364] B.R. Hsieh, E. Etchedgui, Y. Gao, *Synth. Metals* 78 (1996) 269–275.
- [365] V.E. Choong, Y. Park, B.R. Hsieh, Y. Gao, *J. Phys. D-Appl. Phys.* 30 (1997) 1421–1426.
- [366] E. Etchedgui, B.R. Hsieh, Y. Gao, *Polym. Adv. Technol.* 8 (1997) 408–416.
- [367] E. Etchedgui, H. Razafitrimo, B.R. Hsieh, W.A. Feld, M.W. Ruckman, Y. Gao, *Photon. Optoelectron. Polym.* 672 (1997) 408–418.
- [368] L. Yan, N.J. Watkins, S. Zorba, Y.L. Gao, C.W. Tang, *Appl. Phys. Lett.* 79 (2001) 4148–4150.
- [369] Y.L. Gao, L. Yan, *Chem. Phys. Lett.* 380 (2003) 451–455.
- [370] B.H. Hamadani, H. Ding, Y. Gao, D. Natelson, *Phys. Rev. B* 72 (2005) 235302.
- [371] E. Etchedgui, H. Razafitrimo, Y. Gao, B.R. Hsieh, M.W. Ruckman, *Synth. Metals* 78 (1996) 247–252.
- [372] E. Etchedgui, H. Razafitrimo, Y. Gao, B.R. Hsieh, *Appl. Phys. Lett.* 67 (1995) 2705–2707.
- [373] J.X. Tang, C.S. Lee, S.T. Lee, *J. Appl. Phys.* 101 (2007) 064504.
- [374] E.W. Forsythe, V.E. Choong, T.Q. Le, Y.L. Gao, *J. Vacuum Sci. Technol. A-Vacuum Surf. Films* 17 (1999) 3429–3432.
- [375] Y. Hamima, K. Yamashita, H. Ishii, K. Seki, *Thin Solid Films* 366 (2000) 237.
- [376] R. Schlaf, B.A. Parkinson, P.A. Lee, K.W. Nebe, N.R. Armstrong, *J. Phys. Chem.* 103 (1999) 2984.
- [377] I.G. Hill, A. Kahn, *J. Appl. Phys.* 86 (1999) 4515–4519.
- [378] J.W. Shi, H.B. Wang, D. Song, H. Tian, Y.H. Geng, D.H. Yan, *Adv. Funct. Mater.* 17 (2007) 397–400.
- [379] J.M. Lanzafame, R.J.D. Miller, A.A. Muenter, B.A. Parkinson, *J. Phys. Chem.* 96 (1992) 2820.
- [380] A.J. Mäkinen, S. Schoemann, Y. Gao, M.G. Mason, A.A. Muenter, A.R. Melnyk, in: W.R. Salaneck, K. Seki, A. Kahn, J.J. Pireaux (Eds.), *Conjugated Polymer and*

- Molecular Interfaces: Science and Technology for Photonic and Optoelectronic Applications, Marcel Dekker, New York, 2001.
- [381] A.J. Mäkinen, Excited state and charge transfer dynamics at organic molecular film surfaces and interfaces, in: Physics and Astronomy, vol Doctor of Philosophy, University of Rochester, Rochester, 2000, p. 152.
- [382] V. Podzorov, E. Menard, A. Borissov, V. Kiryukhin, J.A. Rogers, M.E. Gershenson, Phys. Rev. Lett. 93 (2004) 086602.
- [383] M. Du, R.L. Opila, C. Case, J. Vacuum Sci. Technol. A 16 (1998) 155–162.
- [384] C. Gahl, K. Ishioka, Q. Zhong, A. Hotzel, M. Wolf, Faraday Discuss. (2000) 191–202.
- [385] N.H. Ge, C.M. Wong, C.B. Harris, Acc. Chem. Res. 33 (2000) 111–118.
- [386] H. Kim, S. Sohn, D. Jung, W.J. Maeng, T.S. Kim, J. Hahn, S. Lee, Y. Yi, M.H. Cho, Org. Electron. 9 (2008) 1140–1145.
- [387] J.E. McDermott, M. McDowell, I.G. Hill, J. Hwang, A. Kahn, S.L. Bernasek, J. Schwartz, J. Phys. Chem. A 111 (2007) 12333–12338.
- [388] K. Muller, Y. Burkov, D. Mandal, K. Henkel, I. Paloumpa, A. Goryachko, D. Schmeisser, Phys. Status Solidi A-Appl. Mater. Sci. 205 (2008) 600–611.
- [389] H.J. Ding, S. Zorba, Y.L. Gao, L.P. Ma, Y. Yang, J. Appl. Phys. 100 (2006) 113706.
- [390] J.E. Malinsky, G.E. Jabbour, S.E. Shaheen, J.D. Anderson, A.G. Richter, T.J. Marks, N.R. Armstrong, B. Kippelen, P. Dutta, N. Peyghambarian, Adv. Mater. 11 (1999) 227.
- [391] V. Bliznyuk, B. Ruhstaller, P.J. Brock, U. Scherf, S.A. Carter, Adv. Mater. 11 (1999) 1257.
- [392] Z.B. Deng, X.M. Ding, S.T. Lee, W.A. Gambling, Appl. Phys. Lett. 74 (1999) 2227–2229.
- [393] J.G. Laquindanum, H.E. Katz, A.J. Lovinger, A. Dodabalapur, Chem. Mater. 8 (1996) 2542.
- [394] S.F. Nelson, Y.-Y. Lin, D.J. Gundlach, T.N. Jackson, Appl. Phys. Lett. 72 (1998) 1854–1856.
- [395] C.D. Dimitrakopoulos, I. Kymmissis, S. Purushothaman, D.A. Neumayer, P.R. Duncombe, R.B. Laibowitz, Adv. Mater. 11 (1999).
- [396] V. Papaefthimiou, A. Siokou, S. Kenmou, J. Appl. Phys. 91 (2002) 1372.
- [397] F.-J.M.Z. Heringdorf, M.C. Reuter, R.M. Tromp, Nature 412 (2001) 517–520.
- [398] L.P. Ma, J. Liu, S. Pyo, Y. Yang, Appl. Phys. Lett. 80 (2002) 362–364.
- [399] L.P. Ma, J. Liu, Y. Yang, Appl. Phys. Lett. 80 (2002) 2997–2999.
- [400] H.J. Ding, S. Zorba, Y.L. Gao, L.P. Ma, Y. Yang, J. Appl. Phys. 100 (2006) 113706.
- [401] J.S. Kim, P.K.H. Ho, D.S. Thomas, R.H. Friend, F. Cacialli, G.W. Bao, S.F.Y. Li, Chem. Phys. Lett. 315 (1999) 307–312.
- [402] T. Kugler, W.R. Salaneck, H. Rost, A.B. Holmes, Chem. Phys. Lett. 310 (1999) 391–396.
- [403] L. Chkoda, C. Heske, M. Sokolowski, E. Umbach, Appl. Phys. Lett. 77 (2000) 1093–1095.
- [404] L. Chkoda, C. Heske, M. Sokolowski, E. Umbach, F. Steuber, J. Staudigel, M. Stossel, J. Simmerer, Synth. Metals 111 (2000) 315–319.
- [405] X.M. Ding, L.M. Hung, L.F. Cheng, Z.B. Deng, X.Y. Hou, C.S. Lee, S.T. Lee, Appl. Phys. Lett. 76 (2000) 2704–2706.
- [406] T. Kugler, W.R. Salaneck, Comptes Rendus De L Academie Des Sciences Serie Iv Physique Astrophysique 1 (2000) 409–423.
- [407] L.S. Liao, J. He, X. Zhou, M. Lu, Z.H. Xiong, Z.B. Deng, X.Y. Hou, S.T. Lee, J. Appl. Phys. 88 (2000) 2386–2390.
- [408] S.F. Alvarado, L. Rossi, P. Muller, P.F. Seidler, W. Riess, IBM J. Res. Dev. 45 (2001) 89–100.
- [409] R.I.R. Blyth, R. Duschek, G. Koller, F.P. Netzer, M.G. Ramsey, J. Appl. Phys. 90 (2001) 270–275.
- [410] R.I.R. Blyth, R. Duschek, F.P. Netzer, M.G. Ramsey, Synth. Metals 121 (2001) 1377–1378.
- [411] A.S. Komolov, P.J. Moller, Synth. Metals 123 (2001) 359–363.
- [412] R. Schlaf, H. Murata, Z.H. Kafafi, J. Elect. Spectrosc. Related Phen. 120 (2001) 149–154.
- [413] I. Seguy, R. Mamy, P. Destruel, P. Jolinat, H. Bock, Appl. Surf. Sci. 174 (2001) 310–315.
- [414] H. Peisert, M. Knupfer, T. Schwieger, J. Fink, Appl. Phys. Lett. 80 (2002) 2916–2918.
- [415] H. Yamane, K. Ito, S. Kera, K.K. Okudaira, N. Ueno, Jpn. J. Appl. Phys. Part 1-Regular Papers Short Notes & Review Papers 41 (2002) 6591–6594.
- [416] R.I.R. Blyth, J. Thompson, Y. Zou, R. Fink, E. Umbach, G. Gigli, R. Cingolani, Synth. Metals 139 (2003) 207–213.
- [417] R.J. Holmes, B.W. D'Andrade, S.R. Forrest, X. Ren, J. Li, M.E. Thompson, Appl. Phys. Lett. 83 (2003) 3818–3820.
- [418] R. Naaman, Z. Vager, Acc. Chem. Res. 36 (2003) 291–299.
- [419] T. Nakamura, K. Iwasawa, S. Kera, Y. Azuma, K.K. Okudaira, N. Ueno, Appl. Surf. Sci. 212 (2003) 515–519.
- [420] H. Peisert, M. Knupfer, J. Fink, Synth. Metals 137 (2003) 869–870.
- [421] X.H. Sun, L.F. Cheng, M.W. Liu, L.S. Liao, N.B. Wong, C.S. Lee, S.T. Lee, Chem. Phys. Lett. 370 (2003) 425–430.
- [422] D.Q. Gao, M.Y. Chan, S.W. Tong, F.L. Wong, S.L. Lai, C.S. Lee, S.T. Lee, Chem. Phys. Lett. 399 (2004) 337–341.
- [423] K.H. Lee, H.W. Jang, K.B. Kim, Y.H. Tak, J.L. Lee, J. Appl. Phys. 95 (2004) 586–590.
- [424] S.M. Tadayyon, H.M. Grandin, K. Griffiths, P.R. Norton, H. Aziz, Z.D. Popovic, Org. Electron. 5 (2004) 157–166.
- [425] J.G. Xue, S.R. Forrest, J. Appl. Phys. 95 (2004) 1869–1877.
- [426] E.L. Hanson, J. Guo, N. Koch, J. Schwartz, S.L. Bernasek, J. Am. Chem. Soc. 127 (2005) 10058–10062.
- [427] J. Hwang, A. Kahn, J. Appl. Phys. 97 (2005) 103705.
- [428] D. Ino, K. Watanabe, N. Takagi, Y. Matsumoto, J. Phys. Chem. B 109 (2005) 18018–18024.
- [429] R.J. Murdey, W.R. Salaneck, Jpn. J. Appl. Phys. Part 1-Regular Papers Short Notes & Review Papers 44 (2005) 3751–3756.
- [430] M.Y. Chan, S.L. Lai, K.M. Lau, C.S. Lee, S.T. Lee, Appl. Phys. Lett. 89 (2006) 163515.
- [431] T. Tani, K. Seki, K. Yoshihara, J. Hanna, Int. J. Photoenergy (2006) 18482.
- [432] S.W. Tong, K.M. Lau, H.Y. Sun, M.K. Fung, C.S. Lee, Y. Lifshitz, S.T. Lee, Appl. Surf. Sci. 252 (2006) 3806–3811.
- [433] N. Huby, L. Hirsch, L. Aubouy, P. Gerbier, A. Van der Lee, F. Amy, A. Kahn, Phys. Rev. B 75 (2007) 115416.
- [434] S.J. Jo, C.S. Kim, S.Y. Ryu, J.B. Kim, J.H. Noh, S.J. Lee, H.K. Baik, Jpn. J. Appl. Phys. Part 1-Regular Papers Brief Communications & Review Papers 46 (2007) 6814–6816.
- [435] H. Mendez, I. Thurzo, D.R.T. Zahn, Phys. Rev. B 75 (2007) 045321.
- [436] S. Toyoshima, K. Kuwabara, T. Sakurai, T. Taima, K. Saito, H. Kato, K. Akimoto, Jpn. J. Appl. Phys. Part 1-Regular Papers Brief Communications & Review Papers 46 (2007) 2692–2695.
- [437] A.S. Wan, A.J. Mäkinen, P.A. Lane, G.P. Kushto, Chem. Phys. Lett. 446 (2007) 317–322.
- [438] X.Z. Wang, X.M. Ding, Z.S. Li, Y.Q. Zhan, I. Bergenti, V.A. Dediu, C. Taliani, Z.T. Xie, B.F. Ding, X.Y. Hou, W.H. Zhang, F.Q. Xu, Appl. Surf. Sci. 253 (2007) 9081–9084.
- [439] N.C. Yang, J. Lee, M.W. Song, N. Ahn, M.H. Kim, S. Lee, B.D. Chin, J. Phys. D-Appl. Phys. 40 (2007) 4466–4470.
- [440] S. Blumstengel, S. Sadofov, C. Xu, J. Puls, R.L. Johnson, H. Glowatzki, N. Koch, F. Henneberger, Phys. Rev. B 77 (2008) 085323.
- [441] M.D. Irwin, B. Buchholz, A.W. Hains, R.P.H. Chang, T.J. Marks, Proc. Natl. Acad. Sci. U.S.A. 105 (2008) 2783–2787.
- [442] S.Y. Kim, K. Hong, K. Kim, J.L. Lee, Electron. Mater. Lett. 4 (2008) 63–66.
- [443] S.Y. Kim, K. Hong, J.L. Lee, K.H. Choi, K.H. Song, K.C. Ahn, Solid-State Electron. 52 (2008) 1–6.
- [444] H. Lee, S.W. Cho, K. Han, P.E. Jeon, C.N. Whang, K. Jeong, K. Cho, Y. Yi, Appl. Phys. Lett. 93 (2008) 043308.
- [445] Y. Lee, J. Kim, S. Kwon, C.K. Min, Y. Yi, J.W. Kim, B. Koo, M. Hong, Org. Electron. 9 (2008) 407–412.
- [446] S. Toyoshima, T. Sakurai, T. Taima, K. Saito, H. Kat, K. Akimoto, Jpn. J. Appl. Phys. 47 (2008) 1397–1399.
- [447] F.X. Wang, X.F. Qiao, T. Xiong, D.G. Ma, Org. Electron. 9 (2008) 985–993.
- [448] H. Yanagi, M. Kikuchi, K.B. Kim, H. Hiramatsu, T. Kamiya, M. Hirano, H. Hosono, Org. Electron. 9 (2008) 890–894.
- [449] F. Nuesch, L.J. Rothberg, E.W. Forsythe, Q.T. Le, Y.L. Gao, Appl. Phys. Lett. 74 (1999) 880–882.
- [450] F.M. Avendano, E.W. Forsythe, Y.L. Gao, C.W. Tang, Synth. Metals 102 (1999) 910–911.
- [451] Y. Park, V. Choong, Y. Gao, B.R. Hsieh, C.W. Tang, Appl. Phys. Lett. 68 (1996) 2699–2701.
- [452] A. Gyoutpu, S. Hara, T. Komatsu, M. Shirinashihama, H. Iwanaga, K. Sakanoue, Synth. Metals 91 (1997) 73.
- [453] A.J. Heeger, I.D. Parker, Y. Yang, Synth. Metals 67 (1994) 2160.
- [454] S.A. Carter, M. Angelopoulos, S. Karg, P.J. Brock, J.C. Scott, Appl. Phys. Lett. 70 (1997) 2067–2069.
- [455] J.S. Kim, M. Granström, R.H. Friend, N. Johansson, W.R. Salaneck, R. Daik, W.J. Feast, F. Cacialli, J. Appl. Phys. 84 (1998) 6859.
- [456] S.K. So, W.K. Choi, L.M. Leung, C.F. Kwong, Appl. Phys. A 68 (1999) 447.
- [457] S.A.V. Slyke, C.H. Chen, C.W. Tang, Appl. Phys. Lett. 69 (1996) 2160–2162.
- [458] S.T. Lee, Y.M. Wang, X.Y. Hou, Appl. Phys. Lett. 74 (1999) 670–672.
- [459] H. Aziz, Z.D. Popovic, N.X. Hu, A.M. Hor, G. Xu, Science 283 (1999).
- [460] L.S. Hung, C.W. Tang, M.G. Mason, Appl. Phys. Lett. 70 (1997) 152–154.
- [461] G.E. Jabbour, B. Kippelen, N.R. Armstrong, N. Peyghambarian, Appl. Phys. Lett. 73 (1998) 1185–1187.
- [462] G.E. Jabbour, Y. Kawabe, S.E. Shaheen, J.F. Wang, M.M. Morrell, B. Kippelen, N. Peyghambarian, Appl. Phys. Lett. 71 (1997) 1762–1764.
- [463] C.H. Lee, Synth. Metals 91 (1997) 125.
- [464] K.R. Choudhury, J. Yoon, F. So, Adv. Mater 20 (2008) 145.
- [465] J. Kido, T. Matsumoto, Appl. Phys. Lett. 73 (1998) 2866–2868.
- [466] Y. Hirose, C.I. Wu, V. Aristov, P. Soukiassian, A. Kahn, Appl. Surf. Sci. 114 (1997) 291–298.
- [467] R. Schlaf, B.A. Parkinson, P.A. Lee, K.W. Nebesny, G. Jabbour, B. Kippelen, N. Peyghambarian, N.R. Armstrong, J. Appl. Phys. 84 (1998) 6729–6736.
- [468] L.S. Hung, L.S. Liao, C.S. Lee, S.T. Lee, J. Appl. Phys. 86 (1999) 4607–4612.
- [469] P.M. Kumar, S. Badrinarayanan, M. Sastry, Thin Solid Films 358 (2000) 122–130.
- [470] K.J. Gaffney, A.D. Miller, S.H. Liu, C.B. Harris, J. Phys. Chem. B 105 (2001) 9031–9039.
- [471] G. Greczynski, M. Fahlman, W.R. Salaneck, J. Chem. Phys. 114 (2001) 8628–8636.
- [472] G. Greczynski, W.R. Salaneck, M. Fahlman, Synth. Metals 121 (2001) 1625–1628.
- [473] A.M. Andersson, D.P. Abraham, R. Haasch, S. McLaren, J. Liu, K. Amine, J. Electrochem. Soc. 149 (2002) A1358–A1369.
- [474] M.Y. Chan, S.L. Lai, M.K. Fung, C.S. Lee, S.T. Lee, Chem. Phys. Lett. 374 (2003) 215–221.
- [475] H.C. Choi, M.K. Lee, H.J. Shin, S.B. Kim, J. Elect. Spectrosc. Related Phen. 130 (2003) 85–96.
- [476] M.Y. Chan, S.L. Lai, M.K. Fung, C.S. Lee, S.T. Lee, J. Appl. Phys. 95 (2004) 5397–5402.
- [477] W.J. Song, S.K. So, K.W. Wong, W.K. Choi, L.L. Cao, Appl. Surf. Sci. 228 (2004) 373–377.
- [478] Y. Yuan, D. Grozea, S. Han, Z.H. Lu, Appl. Phys. Lett. 85 (2004) 4959–4961.
- [479] T. Anazawa, M. Tsukada, Y. Kataoka, Microelectron. Eng. 81 (2005) 222–228.
- [480] G. Gavrila, D.R.T. Zahn, W. Braun, Appl. Phys. Lett. 89 (2006) 162102.
- [481] Z. Kin, K. Yoshihara, H. Kajih, K. Hayashi, Y. Ohmori, Jpn. J. Appl. Phys. Part 1-Regular Papers Brief Communications & Review Papers 45 (2006) 3737–3741.

- [482] M.S. Zhou, C.P. Wu, P.D. Edirisinghe, J.L. Drummond, L. Hanley, *J. Biomed. Mater. Res. Part A* 77A (2006) 1–10.
- [483] H. Ding, Y. Gao, *Appl. Phys. Lett.* 91 (2007) 172107.
- [484] O.V. Molodtsova, V.Y. Aristov, V.M. Zhilin, Y.A. Ossipyan, D.V. Vyalikh, B.P. Doyle, S. Nannarone, M. Knupfer, *Appl. Surf. Sci.* 254 (2007) 99–102.
- [485] S. Fukuda, H. Kajii, H. Okuya, T. Ogata, M. Takahashi, Y. Ohmori, *Jpn. J. Appl. Phys.* 47 (2008) 1307–1310.
- [486] Y. Li, L. Duan, Q. Liu, R. Zhang, D.Q. Zhang, L.D. Wang, J. Qiao, Y. Qiu, *Appl. Surf. Sci.* 254 (2008) 7223–7226.
- [487] P. Shakya, P. Desai, R.J. Curry, W.P. Gillin, *J. Phys. D-Appl. Phys.* 41 (2008) 085108.
- [488] A. Yang, S.T. Shipman, S. Garrett-Roe, J. Johns, M. Strader, P. Szymanski, E. Muller, C. Harris, *J. Phys. Chem. C* 112 (2008) 2506–2513.
- [489] C. Giebelser, H. Antoniadis, D.D.C. Bradley, Y. Shirota, *J. Appl. Phys.* 85 (1999) 608.
- [490] W.R. Salaneck, *Philosophical Transactions of the Royal Society of London Series a-Mathematical Physical and Engineering Sciences* 355 (1997) 789–799.
- [491] T. Osada, P. Barta, N. Johansson, T. Kugler, P. Broms, W.R. Salaneck, *Synth. Metals* 102 (1999) 1103–1104.
- [492] N. Sato, H. Yoshida, K. Tsutsumi, *J. Mater. Chem.* 10 (2000) 85–89.
- [493] W.Y. Gao, A. Kahn, *Appl. Phys. Lett.* 79 (2001) 4040–4042.
- [494] W.Y. Gao, A. Kahn, *Org. Electron.* 3 (2002) 53–63.
- [495] L. Yan, N.J. Watkins, C.W. Tang, Y.L. Gao, *Synth. Metals* 137 (2003) 1037–1038.
- [496] J.G. Xue, S.R. Forrest, *Phys. Rev. B* 69 (2004) 245322.
- [497] S. Tanaka, K. Kanai, E. Kawabe, T. Iwahashi, T. Nishi, Y. Ouchi, K. Seki, *Jpn. J. Appl. Phys. Part 1-Regular Papers Short Notes & Review Papers* 44 (2005) 3760–3763.
- [498] A. Vollmer, O.D. Jurchescu, I. Arfaoui, I. Salzmann, T.T.M. Palstra, P. Rudolf, J. Niemax, J. Pflaum, J.P. Rabe, N. Koch, *Euro. Phys. J. E* 17 (2005) 339–343.
- [499] Y. Wang, W.Y. Gao, S. Braun, W.R. Salaneck, F. Amy, C. Chan, A. Kahn, *Appl. Phys. Lett.* 87 (2005) 193501.
- [500] V.Y. Aristov, O.V. Molodtsova, V.M. Zhilin, D.V. Vyalikh, M. Knupfer, *J. De Physique Iv* 132 (2006) 101–104.
- [501] C.K. Chan, E.G. Kim, J.L. Bredas, A. Kahn, *Adv. Funct. Mater.* 16 (2006) 831–837.
- [502] H.J. Ding, Y.L. Gao, *Appl. Surf. Sci.* 252 (2006) 3943–3947.
- [503] T. Nishi, K. Kanai, Y. Ouchi, M.R. Willis, K. Seki, *Chem. Phys.* 325 (2006) 121–128.
- [504] S.D. Wang, K. Kanai, E. Kawabe, Y. Ouchi, K. Seki, *Chem. Phys. Lett.* 423 (2006) 170–173.
- [505] H. Benmansour, F.A. Castro, M. Nagel, J. Heier, R. Hany, F. Nuesch, *Chimia* 61 (2007) 787–791.
- [506] C.K. Chan, W. Zhao, S. Barlow, S. Marder, A. Kahn, *Org. Electron.* 9 (2008) 575–581.
- [507] F.C. Chen, J.L. Wu, S.S. Yang, K.H. Hsieh, W.C. Chen, *J. Appl. Phys.* 103 (2008) 103721.
- [508] M.K. Fung, K.M. Lau, S.L. Lai, C.W. Law, M.Y. Chan, C.S. Lee, S.T. Lee, *J. Appl. Phys.* 104 (2008) 034509.
- [509] H.H. Lee, J. Hwang, T.W. Pi, Y.C. Wang, W.J. Lin, C.P. Cheng, *J. Synchrotron Radiat.* 15 (2008) 91–95.
- [510] D.S. Leem, S.Y. Kim, J.J. Kim, M.H. Chen, C.I. Wu, *Electrochem. Solid State Lett.* 12 (2009) J8–J10.
- [511] H.J. Ding, Y.L. Gao, *Appl. Phys. Lett.* 87 (2005) 213508.
- [512] H. Ding, Y. Gao, *Appl. Phys. Lett.* 91 (2007) 142112.
- [513] H.J. Ding, Y.L. Gao, *J. Appl. Phys.* 102 (2007) 043703.
- [514] H.J. Ding, K.W. Park, K. Green, Y.L. Gao, *Chem. Phys. Lett.* 454 (2008) 229–232.
- [515] H.J. Ding, Y.L. Gao, *Appl. Phys. Lett.* 92 (2008) 053309.
- [516] H.J. Ding, Y.L. Gao, *Appl. Phys. Lett.* 86 (2005) 213508.
- [517] E.J. Lous, P.W.M. Blom, L.W. Molenkamp, D.M.d. Leeuw, *Phys. Rev. B* 51 (1995) 17251.
- [518] C.M. Heller, I.H. Campbell, D.L. Smith, N.N. Barashkov, J.P. Ferraris, *J. Appl. Phys.* 81 (1997) 3227.
- [519] Y. Yang, A.J. Heeger, *Nature* 372 (1994) 344.
- [520] J.R. Sheats, H. Antoniadis, M.R. Hueschen, W. Leonard, J. Miller, R. Moon, D. Roitman, A. Stocking, *Science* 273 (1996) 884.
- [521] J. Wusten, S. Berger, K. Heimer, S. Lach, C. Ziegler, *J. Appl. Phys.* 98 (2005).
- [522] J. Wusten, K. Heimer, S. Lach, C. Ziegler, *J. Appl. Phys.* 102 (2007) 023708.
- [523] Y. Zhiyong, M. Bensimon, V. Sarria, I. Stolitchnov, W. Jardim, D. Laub, E. Mielczarski, J. Mielczarski, L. Kiwi-Minsker, J. Kiwi, *Appl. Catal. B-Environ.* 76 (2007) 185–195.
- [524] W.F. Zhang, P. Schmidt-Zhang, G. Kossmehl, *J. Solid State Electrochem.* 4 (2000) 225–230.
- [525] C.K. Yang, C.M. Yang, H.H. Liao, S.F. Horng, H.F. Meng, *Appl. Phys. Lett.* 91 (2007) 093504.
- [526] M. Willander, A. Assadi, C. Svensson, *Synth. Metals* 57 (1993) 4099–4104.
- [527] D.M. Taylor, N. Alves, *J. Appl. Phys.* 103 (2008) 054509.
- [528] M.C. Tanese, D. Fine, A. Dodabalapur, L. Torsi, *Biosens. Bioelectron.* 21 (2005) 782–788.
- [529] T.T. Tan, J.W. Gardner, J. Farrington, P.N. Bartlett, *Int. J. Electron.* 77 (1994) 173–184.
- [530] W. Takashima, T. Murasaki, S. Nagamatsu, T. Morita, K. Kaneto, *Appl. Phys. Lett.* 91 (2007) 071905.
- [531] Y.L. Shen, A.R. Hosseini, M.H. Wong, G.G. Malliaras, *Chemphyschem* 5 (2004) 16–25.
- [532] G.D. Sharma, S.G. Sangodkar, M.S. Roy, *Synth. Metals* 80 (1996) 249–256.
- [533] G.D. Sharma, S.K. Gupta, M.S. Roy, *J. Mater. Sci.-Mater. Electron.* 9 (1998) 91–97.
- [534] T.J. Savenije, E. Moons, G.K. Boschloo, A. Goossens, T.J. Schaafsma, *Phys. Rev. B* 55 (1997) 9685–9692.
- [535] B. Remaki, G. Guillaud, D. Mayes, *Opt. Mater.* 9 (1998) 240–244.
- [536] R.Q. Png, P.J. Chia, S. Sivaramakrishnan, L.Y. Wong, M. Zhou, L.L. Chua, P.K.H. Ho, *Appl. Phys. Lett.* 91 (2007) 013511.
- [537] B.S. Ong, Y.L. Wu, P. Liu, *Proc. IEEE* 93 (2005) 1412–1419.
- [538] T. Miyadera, T. Minari, K. Tsukagoshi, H. Ito, Y. Aoyagi, *Appl. Phys. Lett.* 91 (2007) 013512.
- [539] A. Liu, S. Zhao, S.B. Rim, J. Wu, M. Konemann, P. Erk, P. Peumans, *Adv. Mater.* 20 (2008) 1065.
- [540] D.B. Janes, M. Batistuta, S. Datta, M.R. Melloch, R.P. Andres, J. Liu, N.P. Chen, T. Lee, R. Reifenberger, E.H. Chen, J.M. Woodall, *Superlattices Microstruct.* 27 (2000) 555–563.
- [541] K. Ikegami, H. Ohnuki, M. Izumi, *Curr. Appl. Phys.* 6 (2006) 808–812.
- [542] A.R. Hosseini, M.H. Wong, Y.L. Shen, G.G. Malliaras, *J. Appl. Phys.* 97 (2005).
- [543] F. Garnier, *Chem. Phys.* 227 (1998) 253–262.
- [544] F. Garnier, *Photonic Optoelectronic Polym.* 672 (1997) 420–436.
- [545] N.R. Dennington, A.C. Wright, J.O. Williams, *J. Mater. Chem.* 1 (1991) 663–666.
- [546] P. Cova, A. Singh, A. Medina, R.A. Masut, *Solid-State Electron.* 42 (1998) 477–485.
- [547] D.P. Bruno, B. De Jaeger, C. Eneman, J. Mitard, G. Hellings, A. Satta, V. Terzieva, L. Souriau, F.E. Leyls, G. Pourtois, M. Houssa, G. Winderickx, E. Vrancken, S. Sioncke, K. Opsomer, G. Nicholas, M. Caymax, A. Stemans, J. Van Steenberg, P.W. Mertens, M. Meuris, M.M. Heyns, *J. Electrochem. Soc.* 155 (2008) H552–H561.
- [548] J. Bisquert, G. Garcia-Belmonte, A. Munar, M. Sessolo, A. Soriano, H.J. Bolink, *Chem. Phys. Lett.* 465 (2008) 57–62.
- [549] P. Bauerle, G. Gotz, M. Hiller, S. Scheibl, T. Fischer, U. Segelbacher, M. Bennati, A. Grupp, M. Mehring, M. Stoldt, C. Seidel, F. Geiger, H. Schweizer, E. Umbach, M. Schmelzer, S. Roth, H.J. Egelhaaf, D. Oelkrug, P. Emele, H. Port, *Synth. Metals* 61 (1993) 71–79.
- [550] M. Ahles, R. Schmeichel, H. von Seggern, *Appl. Phys. Lett.* 87 (2005) 113505.
- [551] M. Ahles, R. Schmeichel, H. von Seggern, *Appl. Phys. Lett.* 85 (2004) 4499–4501.
- [552] J. Ackermann, C. Videlot, A. El Kassmi, R. Guglielmetti, F. Fages, *Adv. Funct. Mater.* 15 (2005) 810–817.
- [553] N.H. Ge, C.M. Wong, R.L. Lingle, J.D. McNeill, K.J. Gaffney, C.B. Harris, *Science* 279 (1998) 202–205.
- [554] N. Koch, A. Rajagopal, E. Zoyer, J. Ghijssen, X. Crispin, G. Pourtois, J.L. Bredas, R.L. Johnson, J.J. Pireaux, G. Leising, *Surf. Sci.* 454 (2000) 1000–1004.
- [555] H. Rauscher, T.A. Jung, J.L. Lin, A. Kirakosian, F.J. Himpsel, U. Rohr, K. Mullen, *Chem. Phys. Lett.* 303 (1999) 363–367.
- [556] L. Segev, A. Salomon, A. Natan, D. Cahen, L. Kronik, F. Amy, C.K. Chan, A. Kahn, *Phys. Rev. B* 74 (2006) 165323.
- [557] A. Rosa, E.J. Baerends, *Inorg. Chem.* 31 (1992) 4717.
- [558] M.S. Liao, S.J. Scheiner, *Chem. Phys.* 114 (2001) 9780.
- [559] H. Ding, K.W. Park, Y. Gao, *SPIE Proc* 7051 (2008) 705111.
- [560] T. Schwieger, H. Peisert, M.S. Golden, M. Knupfer, J. Fink, *Phys. Rev. B* 66 (2002) 155207.
- [561] X. Yang, Y. Mo, W. Yang, G. Yu, Y. Cao, *Appl. Phys. Lett.* 79 (2001) 563–565.
- [562] R. Schlaf, B.A. Parkinson, P.A. Lee, K.W. Nebesny, N.R. Armstrong, *Appl. Phys. Lett.* 73 (1998) 1026–1028.
- [563] K.L. Wang, B. Lai, M. Lu, X. Zhou, L.S. Liao, X.M. Cing, X.Y. Hou, S.T. Lee, *Thin Solid Films* 363 (2000) 25.
- [564] J.M. Zhao, S.T. Zhang, X.J. Wang, Y.Q. Zhan, X.Z. Wang, G.Y. Zhong, Z.J. Wang, X.M. Ding, W. Huang, X.Y. Hou, *Appl. Phys. Lett.* 84 (2004) 2913–2915.
- [565] A. Curioni, W. Andreoni, R. Treusch, F.J. Himpsel, E. Haskal, P. Seidler, C. Heske, S. Kakar, T.v. Buuren, L.J. Terminello, *Appl. Phys. Lett.* 72 (1998) 1575–1577.
- [566] C.I. Wu, C.R. Lee, T.W. Pi, *Appl. Phys. Lett.* 87 (2005) 212108.
- [567] E. Umbach, C. Seidel, J. Taborski, R. Li, A. Soukopp, *Physica Status Solidi B-Basic Res.* 192 (1995) 389–406.
- [568] E. Umbach, M. Sokolowski, R. Fink, *Appl. Phys. A-Mater. Sci. Process.* 63 (1996) 565–576.
- [569] E. Umbach, K. Glockler, M. Sokolowski, *Surf. Sci.* 402 (1998) 20–31.
- [570] C.I. Wu, A. Kahn, N. Taskar, D. Dorman, D. Gallagher, *J. Appl. Phys.* 83 (1998) 4249–4252.
- [571] C. Mariani, F. Allegretti, V. Corradini, G. Contini, V. Di Castro, C. Baldacchini, M.G. Betti, *Phys. Rev. B* 66 (2002) 115407.
- [572] G. Koller, R.I.R. Blyth, S.A. Sardar, F.P. Netzer, M.G. Ramsey, *Surf. Sci.* 536 (2003) 155–165.
- [573] H. Huang, H.Y. Mao, Q. Chen, X.Z. Yan, H.Q. Qian, J.H. Zhang, H.Y. Li, P.M. He, S.N. Bao, *Physica B-Condensed Matter* 352 (2004) 36–41.
- [574] H. Huang, X.C. Yan, H.Y. Mao, Q. Chen, H.Q. Qian, J.H. Hang, H.Y. Li, P.M. He, S.N. Bao, *Acta Physico-Chimica Sinica* 20 (2004) 892–896.
- [575] H. Huang, X.C. Yan, H.Y. Mao, Q. Chen, H.Q. Qian, J.H. Zhang, H.Y. Li, P.M. He, S.N. Bao, *Acta Physico-Chimica Sinica* 20 (2004) 882–886.
- [576] H.Y. Mao, H. Huang, Q. Chen, N.V. Richardson, Y. Wu, J.H. Zhang, H.Y. Li, P.M. He, S.N. Bao, *J. Chem. Phys.* 121 (2004) 6972–6977.
- [577] H.Y. Mao, H. Huang, X.C. Yan, Q. Chen, H.Q. Qian, J.H. Zhang, H.Y. Li, P.M. He, S.N. Bao, *Acta Phys. Sin.* 54 (2005) 460–466.
- [578] S. Blumstengel, N. Koch, S. Duhm, H. Glowatzky, R.L. Johnson, C. Xu, A. Yassar, J.P. Rabe, F. Henneberger, *Phys. Rev. B* 73 (2006) 165323.
- [579] O. McDonald, A.A. Cafolla, D. Carty, G. Sheerin, G. Hughes, *Surf. Sci.* 600 (2006) 3217–3225.
- [580] M.G. Betti, F. Bussolotti, L. Chiodo, P. Monachesi, C. Mariani, *Surf. Sci.* 601 (2007) 2580–2583.
- [581] M.G. Betti, A. Kanjilal, C. Mariani, *J. Phys. Chem. A* 111 (2007) 12454–12457.
- [582] P. Fenter, P.E. Burrows, P. Eisenberger, S.R. Forrest, *J. Cryst. Growth* 152 (1995) 65.
- [583] E. Umbach, M. Sokolowski, R. Fink, *Appl. Phys. A* 63 (1996) 565–576.
- [584] C. Kendrick, A. Kahn, *Appl. Surf. Sci.* 123/124 (1998) 405.
- [585] J. Taborski, P. Vaterlein, H. Dietz, U. Zimmermann, E. Umbach, *J. Elect. Spectrosc. Related Phen.* 75 (1995) 129–147.
- [586] A. Soukopp, K. Glockler, P. Bauerle, M. Sokolowski, E. Umbach, *Adv. Mater.* 8 (1996) 902.

- [587] C. Seidel, A. Soukopp, R. Li, P. Bauerle, E. Umbach, *Surf. Sci.* 374 (1997) 17–30.
- [588] M. Bohringer, W.D. Schneider, R. Berndt, K. Glockler, M. Sokolowski, E. Umbach, *Phys. Rev. B* 57 (1998) 4081–4087.
- [589] K. Glockler, C. Seidel, A. Soukopp, M. Sokolowski, E. Umbach, M. Bohringer, R. Berndt, W.D. Schneider, *Surf. Sci.* 405 (1998) 1–20.
- [590] R. Fink, D. Gador, U. Stahl, Y. Zou, E. Umbach, *Phys. Rev. B* 60 (1999) 2818–2826.
- [591] F.S. Tautz, S. Sloboshanin, V. Shklover, R. Scholz, M. Sokolowski, J.A. Schaefer, E. Umbach, *Appl. Surf. Sci.* 166 (2000) 363–369.
- [592] F.S. Tautz, M. Eremitchenko, J.A. Schaefer, M. Sokolowski, V. Shklover, K. Glockler, E. Umbach, *Surf. Sci.* 502 (2002) 176–184.
- [593] L. Chkoda, M. Schneider, V. Shklover, L. Kilian, M. Sokolowski, C. Heske, E. Umbach, *Chem. Phys. Lett.* 371 (2003) 548–552.
- [594] L. Kilian, U. Stahl, I. Kossev, M. Sokolowski, R. Fink, E. Umbach, *Surf. Sci.* 602 (2008) 2427–2434.
- [595] M. Jung, U. Baston, G. Schnitzler, M. Kaiser, J. Papst, T. Porwol, H.J. Freund, E. Umbach, *J. Mol. Struct.* 293 (1993) 239.
- [596] H. Kakuta, T. Hirahara, I. Matsuda, T. Nagao, S. Hasegawa, N. Ueno, K. Sakamoto, *Phys. Rev. Lett.* 98 (2007) 247601.
- [597] K. Hummer, C. Ambrosch-Daxl, *Phys. Rev. B* 72 (2005) 205205.
- [598] A.B. Chwang, C.D. Frisbie, *J. Phys. Chem. B* 104 (2000) 12202–12209.
- [599] S.E. Fritz, S.M. Martin, C.D. Frisbie, M.D. Ward, M.F. Toney, *J. Am. Chem. Soc.* 126 (2004) 4084–4085.
- [600] V. Kalihari, E.B. Tadmor, G. Haugstad, C.D. Frisbie, *Adv. Mater.* 20 (2008) 4033.
- [601] M.J. Loiacono, E.L. Granstrom, C.D. Frisbie, *J. Phys. Chem. B* 102 (1998) 1679–1688.
- [602] C.R. Newman, R.J. Chesterfield, M.J. Panzer, C.D. Frisbie, *J. Appl. Phys.* 98 (2005) 084506.
- [603] K. Seshadri, C.D. Frisbie, *Appl. Phys. Lett.* 78 (2001) 993–995.
- [604] S. Zorba, Y. Shapir, Y.L. Gao, *Phys. Rev. B* 74 (2006) 245410.
- [605] D.J. Gundlach, Y.Y. Lin, T.N. Jackson, S.F. Nelson, D.G. Schlom, *IEEE Electron Device Lett.* 18 (1997) 87.
- [606] T. Vicsek, *Phys. Rev. Lett.* 53 (1984) 2281–2284.
- [607] S.J. Wang, H.H. Park, *J. Electroceram.* 18 (2007) 161–165.
- [608] D.R.T. Zahn, S. Seifert, G. Gavrila, W. Braun, *J. Optoelectron. Adv. Mater.* 9 (2007) 522–526.
- [609] M. Chiodi, L. Gavioli, M. Beccari, V. Di Castro, A. Cossaro, L. Floreano, A. Morgante, A. Kanjilal, C. Mariani, M.G. Betti, *Phys. Rev. B* 77 (2008) 115321.
- [610] H.K. Lee, K.J. Kim, T.H. Kang, J. Chung, B. Kim, *Surf. Sci.* 602 (2008) 914–918.
- [611] H.K. Lee, K.J. Kim, T.H. Kang, S. Kim, J.W. Chung, B. Kim, *J. Elect. Spectrosc. Related Phen.* 164 (2008) 44–47.
- [612] R. Treusch, F.J. Himpsel, S. Kakar, L.J. Terminello, C. Heske, T. van Buuren, V.V. Dinh, H.W. Lee, K. Pakbaz, G. Fox, I. Jimenez, *J. Appl. Phys.* 86 (1999) 88–93.
- [613] R.I.R. Blyth, J. Thompson, V. Arima, Y. Zou, R. Fink, E. Umbach, G. Gigli, R. Cingolani, *Synth. Metals* 142 (2004) 293–298.